Dissertation

STRUCTURE AND FUNCTION ANALYSIS IN PROM1-RELATED RETINOPATHY

submitted by

Dr.med.univ.

Gernot SCHLIEßLEDER

for the Academic Degree of

Doctor of Medical Science

(Dr. scient. med.)

at the

Medical University of Graz

Department of Ophthalmology

under the Supervision of

Priv.-Doz. Dr. med. Rupert Wolfgang STRAUß

2024

2. Statutory Declaration

I formally declare that I have independently written the submitted thesis. I have not used any external support other than the cited literature and other sources mentioned in the document. I have clearly marked and separately listed all literature and all other sources used in the production of this scholarly work, verbatim or substantive. aware that the violation of these rules will lead to the failure of the thesis.

Graz, 23.1.2024 Gernot Schließleder

3. Disclosures

Sections of this thesis have been previously published in

Schließleder G[1], Kalitzeos A[2,3], Kasilian M[2,3], Singh N[2,3], Wang Z[4,5], Hu Z[4,5], Großpötzl M[1], Saada S[6], Wedrich A1, Michaelides M2,3, Strauss R1,2,3,7,8. Deep phenotyping of PROM1-associated retinal degeneration. British Journal of Ophthalmology (Internet). 2023 (cited 2023 Oct 26); Available from: https://bjo.bmj.com/content/early/2023/04/20/bjo-2022-322036.

1 Department of Ophthalmology, Medical University Graz, Graz, Styria, Austria

2 UCL Institute of Ophthalmology, University College London, London, UK

3 Moorfields Eye Hospital, NHS Foundation Trust, London, UK

4 School of Engineering, University of California, Los Angeles, California, USA

5 Doheny Image Analysis Laboratory, Doheny Eye Institute, Los Angeles, California, USA

6 Doheny Image Reading Center, David Geffen School of Medicine at University of California Los Angeles, Pasadena, California, USA

7 Department of Ophthalmology, Kepler University Hospital University Clinic for Ophthalmology and Optometry, Linz, Austria

8 Institute of Molecular and Clinical Ophthalmology Basel (IoB), Basel, Switzerland

Within the scope of this thesis, if text excerpts, tables, or figures from this publication are replicated or modified, they will be denoted as (1).

In accordance with the Author Permissions Policy (2) agreed upon with the copyright owners, BMJ Publishing Group Ltd, I am granted the permission to integrate the article into my dissertation. This permission is subject to the condition that the article is not employed for commercial purposes and that proper credit is given to its initial publication in the journal.

I hereby verify that all co-authors have explicitly consented to the inclusion of their published data in this dissertation.

The publication (1) received financial support from various sources, including the National Center for Advancing Translational Sciences at the National Institutes of Health, provided

through grant UL1TR000055. Additional funding was provided by grants from the National Institute for Health Research (NIHR) Biomedical Research Centre at Moorfields Eye Hospital NHS Foundation Trust and UCL Institute of Ophthalmology, as well as The Wellcome Trust (grant number 099173/Z/12/Z). RWS's research is further supported by the Foundation Fighting Blindness Clinical Research Institute.

Senior Scientist DI Dr. Regina Riedl from the Institute for Medical Informatics, Statistics, and Documentation at the Medical University of Graz provided guidance for the statistical analysis of the thesis.

All graphics included in my thesis were personally created by me. In order to enhance the understanding of certain complex subject matter in the introduction and discussion sections, I have redrawn, modified, and incorporated graphics from other publications that I deemed essential. These graphics were used either under a Creative Commons license (identified as Figure 1, 11, and 12 in my thesis) or with the corresponding permissions (referred to as Figures 2 and 3 in my thesis), which were obtained.

The authors and sources of graphics from other works, used as templates for modified graphics, are acknowledged within the section where the modified graphic is located in the thesis. This acknowledgment includes the phrase “adapted from,” followed by a citation in the Vancouver style, along with a note about the permission granted by the respective copyright owner.

I want to confirm that I have adhered to the Creative Commons license terms (3):

- Attribution: I have provided appropriate credit to the authors by citing their work and referencing the source, including the title, authors, and publication details, as mentioned above

- No additional restrictions: I have not imposed any legal terms or technological measures that would restrict others from using the graphics in the same manner the license permits.

- Notices: I understand that I do not have to comply with the license for elements of the material in the public domain or where my use is permitted by an applicable exception or limitation.

Additionally, I have followed the permission conditions set by the Association for Research in Vision and Ophthalmology (4), including the requirement to include a full article citation and acknowledge them as the copyright holder for my Figure 2.

I have obtained permission from Karger AG (5), in accordance with their sharing policies, to use a modified graphic in my thesis. The copyright of my Figure 3 remains with Karger AG, and I will duly attribute the source. This use is non-commercial.

4. Foreword

Imaging of the human retina is evolving at a still increasing pace, like telemedicine, something that nobody could have imagined a few years ago, and now, caused by lockdowns during the COVID-19 pandemic, is having an also evolving impact on different health systems. Likewise, other communication options like online meetings via zoom meetings instead of cumbersome office bookings associated with finding appointments and traveling, these options turned out be an alternative. Important work steps in the context of this dissertation, including the analysis, e.g. the segmentation of optical coherence tomography (OCT) scans, autofluorescence images, and especially adaptive-optics scanning laser ophthalmoscopy were carried out via remote online access to collaborating centers in Los Angeles (United States of America) and London (United Kingdom). Of note, the basic idea of this doctoral thesis was born before or at the beginning of COVID-19, and the successful completion underscores that the methods, especially those by collaborating with international experts, were already directing into the future, especially because they are necessary for research in rare diseases, also beyond the context of multi-center studies. Times have passed when science could only be carried out in large, influential research centers in metropolises of western world. Today, worldwide collaborations can be entered into online, outsourced work steps can be performed from anywhere in the world, which also saves costs and resources for larger-scale projects. Furthermore, this project therefore underscores and fills the policy of international “net-working” as proposed by the Medical University Graz with “lived life”. I remain in great gratitude being allowed to contribute for the benefit of mankind and ophthalmology science.

5. Acknowledgements

I thank Rupert W. Strauss for the supervision of the dissertation, his great commitment, his perseverance and competent support throughout the entire process, especially for allowing me to be part of a global research network between the absolute top institutions in the world in the field of retinal dystrophies. I also thank my colleague Manuel Großpötzl, for training me in the segmentation of spectral-domain optical coherence tomography images and being always a reliable contact person when assistance was needed. I also owe my deepest gratitude to my family, who made my long education possible and to whom I can always come back for strength and whose support I can always count on without hesitation. In particular, I would also like to thank my lovely girlfriend Lisa, who supports me in all my projects and always gave me time to carry out scientific activities in my leisure time. Thanks also to my friends, my employer, the Department of Ophthalmology of Medical University of Graz, and in particular my second supervisor, Prof. Wedrich, because consideration is always given when conducting the lectures related to the doctoral studies, even during working hours. I also thank Prof. SriniVas Sadda (leading the research group at Doheny Imaging Reading Center (DIRC) at University of California Los Angeles (UCLA)) and Prof. Michel Michaelides, leading the study group for inherited retinal dystrophies at Moorfields Eye Hospital and UCL Institute of Ophthalmology, University College London (United Kingdom) for the possibility to collaborate with them and their respective study team in order to perform this study.

6. Table of Contents

7. Abbreviations and Definitions

A-scan: A single line of data acquisition in OCT

A2E: N-retinylidene-N-retinylethanolamine

AAV: Adeno-Associated Virus

ABCA4: ATP-Binding Cassette Subfamily A Member 4

AD: Autosomal Dominant

ADAR: Adenosine Deaminase Acting on RNA

AMD: Age-Related Macular Degeneration

AOSLO: Adaptive Optics Scanning Light Ophthalmoscopy

AR: Autosomal Recessive

ARD: Autosomal Recessive Retinal Degeneration

ART: Automatic Real Time

ARVO: Association for Research in Vision and Ophthalmology

ASD: Autosomal Dominant

ASO: Antisense Oligonucleotide

B-scan: A two-dimensional cross-sectional image in OCT

BCVA: Best-Corrected Visual Acuity

BD: Best Disease

BEM: Bull's Eye Maculopathy

BRILLIANCE: Name of a clinical trial

CC BY: Creative Commons Attribution License

CCD: Charge-Coupled Device

CEP290: Gene associated with Leber's Congenital Amaurosis (LCA)

CMOS: Complementary Metal-Oxide-Semiconductor

CNN: Convolutional Neural Network

CRD: Cone-Rod Dystrophy

CRISPR/Cas9: Clustered Regularly Interspaced Short Palindromic Repeats/CRISPR-associated protein 9

CSCs: Cancer Stem Cells

CSLO: Confocal Scanning Laser Ophthalmoscopy

DAF: Decreased Autofluorescence

DCC: Data Coordinating Center

dB: Decibels

DDAF: Definitely Decreased Autofluorescence

DIRC: Doheny Imaging Reading Center

DNA: Deoxyribonucleic Acid

EMA: European Medicine Agency

ERG: Electroretinography

ETDRS: Early Treatment of Diabetic Retinopathy Study

FA: Fluorescein Angiography

FAF: Fundus Autofluorescence

FCN: Fully Convolutional Neural Network

FDA: Food and Drug Administration

FLIO: Fluorescence Lifetime Imaging Ophthalmoscopy

GA: Geographic Atrophies

GAF: Green-Absorbing Fundus Autofluorescence

GCL: Ganglion Cell Layer

GZ: Garbage Zone

HDR: Homology-Directed Repair

HMM: High Magnification Module

ICB: Inner Choroid Boundary

ILM: Inner Limiting Membrane

INL: Inner Nuclear Layer

IPL: Inner Plexiform Layer

IRD: Inherited Retinal Disease

IRL: Inner Retinal Layers

IS: Inner Segment

IS-OS: Inner Segment-Outer Segment

kb: Kilobase

L-cones: Long-Wavelength Cones

LCA: Leber Congenital Amaurosis

LD: Lumen Diameter

LF: Lipofuscin

LRAT: Lecithin Retinol Acyltransferase

M-cones: Medium-Wavelength Cones

MacTel: Macular Telangiectasia

MEH: Moorfields Eye Hospital

miRNA: MicroRNA

mm: Millimeters

MP: Microperimetry

mRNA: Messenger RNA

n/a = not applicable

NCBI: National Center for Biotechnology Information

NEI: National Eye Institute

NGS: Next Generation Sequencing

NIR-FAF: Near-Infrared Fundus Autofluorescence

nm: Nanometers

OCT: Optical Coherence Tomography

ONL: Outer Nuclear Layer

ONT: Oxford Nanopore Technologies

OPL: Outer Plexiform Layer

OS: Outer Segment

PacBio: Pacific Biosciences

PACS: Picture Archiving and Communication Systems

PCD: Peak Cone Density

PMO: Phosphorodiamidate Morpholino Oligonucleotide

PRC-AUC: Precision-Recall Area Under the Curve

PRL: Preferred Retinal Loci

PROM1: Prominin-1

qAF: Quantitative Autofluorescence

QDAF: Questionably Decreased Autofluorescence

RBP: Retinol Binding Protein

RD: Retinal Degeneration/ Dystrophy

RHO: Rhodopsin (a gene associated with Retinitis Pigmentosa)

RNA: Ribonucleic Acid

RNAi: RNA Interference

RNFL: Retinal Nerve Fiber Layer

ROS: Reactive Oxygen Species

RP: Retinitis Pigmentosa

RPE: Retinal Pigment Epithelium

RVO: Retinal Vein Occlusion

S-cones: Short-Wavelength Cones

SD-OCT: Spectral-Domain Optical Coherence Tomography

SD: Standard Deviation

SHWS: Shack-Hartmann Wavefront Sensor

SLO: Scanning Laser Ophthalmoscopy

SMART: Name of a study

SMRT: Single Molecule Real-Time

SS-OCT: Swept-Source Optical Coherence Tomography

STGD1: Stargardt Disease Type 1

STGD4: Stargardt Disease Type 4

SW-FAF: Short-Wavelength Fundus Autofluorescence

TD-OCT: Time-Domain Optical Coherence Tomography

TGA: Therapeutic Goods Administration

UCLA: University of California, Los Angeles

WT: Wall Thickness

8. List of Figures

9. List of Tables

10. Abstract German

Hintergrund: Es besteht ein begrenztes Verständnis darüber, wie Sequenzvarianten des PROM1-Gens spezifisch Zapfen-Photorezeptoren beeinflussen. Diese Arbeit hatte zum Ziel, die Struktur und Funktion der Netzhaut, insbesondere der Zapfenphotorezeptoren, bei PatientInnen mit PROM1-assoziierter Retinadegeneration (PROM1-RD) zu untersuchen.

Methoden: Zwölf PatientInnen aus vier Stammbäumen mit potenziell krankheitsverursachenden Varianten im PROM1-Gen wurden in der Datenbank des Moorfields Eye Hospital identifiziert. Daraus wurden sechs Studienaugen in diese institutionelle Längsschnittkohorte einbezogen, die zwei Untersuchungszeitpunkte umfasste: die initiale Baseline-Untersuchung und ein Follow-up nach 24 Monaten. Folgende Parameter wurden an den Untersuchungszeitpunkten bestimmt: Die Sehschärfe unter Verwendung des Early Treatment Diabetic Retinopathy Study (ETDRS)-Protokolls, Bereiche mit verminderter Autofluoreszenz durch Fundusautofluoreszenz (FAF) Aufnahmen, Gesamtdicke der Netzhaut und individuelle Schichtdicken gemessen durch Spektralbereichs-Optischer Kohärenztomographie (SD-OCT), sowie Zapfendichte (der primäre Endpunkt) unter Verwendung der adaptiven Optik-Scanning-Licht-Ophthalmoskopie (AOSLO). SD-OCT-Ergebnismessungen wurden mit Normdaten verglichen, die vom Moorfields Eye Hospital (MEH) bereitgestellt wurden.

Ergebnisse: AOSLO-Bildgebung von beurteilbarer Qualität war bei den rechten Augen von vier PatientInnen erfolgreich. Bei zwei Augen konnte nach zwei Jahren eine auswertbare Vergleichsuntersuchung durchgeführt werden. Herausfordernd dabei waren instabile Fixierung und ausgedehnte Atrophieherde. Zum Zeitpunkt der Baselineuntersuchung reichte die bestkorrigierte Sehschärfe (BCVA) von 35 bis 85 ETDRS-Buchstaben. Alle vier Augen zeigten veränderte Autofluoreszenzmuster. Die durchschnittliche Außensegmentschichtdicke war im Vergleich zu Werten aus der Normdatenbank signifikant reduziert. Die Zapfendichte wurde im zentralen Bereich und/oder in verschiedenen Abständen von der Fovea quantifiziert. Bei den beiden Augen, die nach zwei Jahren einer erneuten Untersuchung unterzogen wurden, wurde eine Reduktion der Dicke der äußeren Netzhautschichten sowie der Zapfendichte festgestellt, die über das Maß der Standardabweichung hinausgingen. Zusätzlich wurde eine Verringerung der bestmöglich korrigierten Sehschärfe beobachtet. In einem Auge vergrößerte sich der Bereich mit verminderter Autofluoreszenz, in der FAF-Aufnahme, während im anderen das Autofluoreszenzmuster unverändert blieb.

Schlussfolgerung: Diese Arbeit ist die erste, die Individuen mit PROM1-assoziierter Netzhautdegeneration auf zellulärer Ebene, einschließlich AOSLO-Bildgebung, untersucht hat. Sie umfasst Fälle sowohl mit autosomal-dominanter (AD) als auch mit autosomal-rezessiver (AR) Vererbung und enthält longitudinale Daten. Die AOSLO-Bildgebung ermöglichte die Messung der Zapfendichte trotz signifikanter Ausdünnung der Photorezeptoraußensegmente, wie sie in der SD-OCT-Analyse zu sehen war. Der Nachweis residualer Zapfen, selbst in fortgeschrittenen Stadien der PROM1-RD, könnte eine Chance für potenzielle auf Zapfen ausgerichtete therapeutische Interventionen darstellen.

11. Abstract

Background: There is a limited understanding of how PROM1 sequence variants specifically impact cone photoreceptors. This thesis aimed to investigate the structure and function of the retina, with a particular focus on cone photoreceptors, in patients with PROM1-associated retinal degeneration (PROM1-RD).

Methods: Twelve patients from four pedigrees with potentially disease-causing variants in the PROM1 gene from the Moorfields Eye Hospital database were identified. Six study eyes were included in this institutional longitudinal cohort, which featured two assessments: the initial baseline examination and a follow-up after a 24-month interval. Visual acuity using the Early Treatment Diabetic Retinopathy Study (ETDRS) protocol, areas of decreased autofluorescence via fundus autofluorescence (FAF), total retinal thickness, and individual layer thickness by spectral domain optical coherence tomography (SD-OCT), and cone density (the primary endpoint) using adaptive optics scanning light ophthalmoscopy (AOSLO), were measured. SD-OCT outcome measures were compared to normative data provided by the Moorfields Eye Hospital (MEH).

Results: AOSLO imaging of assessable quality was successful for the right eyes of four patients. Imaging of a comparable standard could be successfully repeated for two eyes after two years. Challenges encountered included unstable fixation and extensive atrophy. At baseline, the best-corrected visual acuity (BCVA) ranged from 35 to 85 ETDRS letters. All four eyes showed altered autofluorescence patterns. The outer segment layer thickness was significantly reduced in comparison to the normative data. Cone density was quantified in the central area and/or at varying distances from the fovea. In the two eyes with follow-up examinations after two years, reductions in the thickness of outer retinal layers and cell density exceeding the standard deviation, as well as a decrease in BCVA, were observed. In one eye, the area of decreased autofluorescence, as determined by FAF, expanded, while in the other, the autofluorescence pattern remained unchanged.

Conclusion: This study is the first to investigate PROM1-associated retinal degeneration at the cellular level, including AOSLO imaging. It encompasses cases of both autosomal dominant (AD) and autosomal recessive (AR) inheritance and provides longitudinal data. AOSLO imaging enabled the measurement of cone density despite significant thinning of the outer segments, as seen in SD-OCT analysis. The evidence of residual cones, even in

advanced stages of PROM1-RD, may represent a promising opportunity for potential cone-directed therapeutic interventions.

Adapted from Schließleder et al. (1) with authorization from the copyright holders BMJ Publishing Group Ltd (2).

12. Introduction

12.1. Cones and rods

Rods and cones, the two types of photoreceptor cells in the retina, exhibit distinct structural and functional differences:

- Cones have a conical shape and are primarily concentrated in the central region of the retina, particularly in the fovea. Cones are responsible for color vision and provide high visual acuity, especially in well-lit conditions. They possess different types of photopigments, known as cone opsins, which allow them to perceive different wavelengths of light and distinguish various colors. Based on the specific wavelength sensitivity of their photopigment, cones are classified into three categories: short-wavelength cones (S-cones), medium-wavelength cones (M-cones), and long-wavelength cones (L-cones). The outer segments of cones contain membranous discs that house these cone opsins (6, 7).

- Rods, the second type of photoreceptor cells, exhibit their own unique structure. They are elongated and cylindrical in shape and are more abundant in the peripheral regions of the retina. Rods are highly sensitive to dim light, making them crucial for night vision and peripheral vision. Unlike cones, rods do not contribute significantly to color vision as they contain a single type of photopigment called rhodopsin. The outer segments of rods consist of numerous membranous discs that contain the rhodopsin photopigment, enhancing their light-capturing capacity (8).

These structural differences between cones and rods enable them to fulfill different roles in visual perception. Cones provide detailed color vision and high visual acuity, making them more important in everyday life for tasks such as color perception, reading, object identification, and facial recognition, while rods excel in low-light conditions and peripheral vision (8).

Due to the small size of photoreceptors, typically ranging from 2 to 10 µm in diameter, direct visualization of these cells was not possible until the development of modern imaging techniques such as optical coherence tomography (OCT) (9) and adaptive optics (10). Prior to these advancements, researchers and clinicians relied heavily on functional tests to assess the activity of photoreceptors, including their sensitivity to light, response times, and overall functionality.

12.2. Inherited retinal diseases (IRDs)

Inherited retinal diseases (IRDs) are a genetically and clinically heterogeneous group of retinal disorders characterized by photoreceptor dysfunction or degeneration. These diseases are among the most common causes of blindness in central European countries (11). In Scotland and Wales, IRDs have overtaken diabetic retinopathy in working-age adults for the first time in almost five decades (12). IRDs are classically divided into two sub-types: stationary (13) and progressive (14). The stationary disorders (cone and rod dysfunction syndromes) are congenital or of early-infantile onset, and give rise to predominantly cone or rod dysfunction, whereas progressive cone dystrophy (COD), cone-rod dystrophy (CORD), and rod-cone dystrophy (RCD) are usually of later-onset, depending on the severity of mutation/disease-causing variant (15). Management of IRDs is so far rather mostly symptomatic and involves the correction of refractive errors, often in case of macular dystrophies with different magnifiers, the restauration of clear media (by performing e.g. cataract surgery), the optimisation of visual potential and the prevention of amblyopia. The management of IRDs is significantly influenced by age and onset of disease. In infants or patients in early developmental stage, the development of severe visual impairment can also have an adverse impact on other activities such as it may impair the speaking abilities, nonverbal communication, social skills, and other behaviours, highlighting and indicating the importance of multi-specialists in the therapeutic approaches. Access to low vision aids and assistive technologies, educational and work-related support and counselling, are all of paramount importance (16). Recent advances in molecular genetics, particularly next generation sequencing (NGS), have greatly improved molecular diagnosis, as the underlying causative genes and pathogenic variants can be identified in a large proportion of patients. Molecular genetic testing is crucial for accurate diagnosis, prognostication, and for the treatment prospects of targeted therapeutics (17).

12.2.1. Emerging therapies for IRDs

The approval of the first gene therapy for RPE65-associated retinopathy by the Food and Drug Administration (FDA), the European Medicines Agency (EMA), and the Therapeutic Goods Administration (TGA) marks a significant milestone in the treatment of inherited retinal diseases (IRDs) (18). To the present day, there are numerous ongoing therapeutic studies on various other IRDs. Common therapeutic approaches include gene replacement therapy, RNA-based therapies, stem cell therapy, optogenetic therapy, and pharmacological therapy.

- Gene replacement therapy involves providing functional genes to replace or compensate for defective or lost ones. Besides the approval of Luxturna for RPE65-associated retinopathy (18), promising results have been achieved using adeno-associated viruses (AAV) targeting the CHM gene in the case of Choroideremia (19).

- RNA-based therapies aim to correct abnormal gene expression using targeted RNA molecules. An example is the development of an investigational RNA therapy called QR-421a for Usher syndrome and retinitis pigmentosa caused by mutations in the USH2A gene (20).

- Stem cell therapy involves transplanting specialized cells into the retina to replace damaged or lost cells. Clinical studies are investigating the use of embryonic stem cells, induced pluripotent stem cells (iPSCs), and retinal precursor cells for treating IRDs such as Stargardt disease (21) and retinitis pigmentosa (22).

- Optogenetic therapies aim to restore light sensitivity in degenerated retinas by introducing light-sensitive proteins into non-light-sensitive cells. The development of optogenetic therapies for IRDs such as retinitis pigmentosa is in the research phase, with human clinical studies still in early stages (23).

- Pharmacological therapies are also being explored as potential treatment options for IRDs. The Fight RP study examined the effects of orally administered N-Acetylcysteine (NAC) in patients with retinitis pigmentosa (RP), showing promising results warranting further investigation in controlled studies (24).

12.3. PROMININ1

Prominin-1 (PROM1), also known as CD133, is a widely recognized marker for cancer stem cells (CSCs) (25-28). PROM1 is primarily expressed in microvilli or membrane protrusions of various stem cells and progenitor cells, indicating its association with lipid rafts (29-31). Since its initial discovery (32, 33), PROM1 has undergone extensive investigation. Its identification in CSCs has led to its exploration as a potential target for cancer therapies over the past few decades (25-28, 34, 35). Recently, PROM1 has been the subject of intensive research in normal organs, including the liver, intestine, central and peripheral nervous system, eyes, and teeth, using PROM1-deficient mouse models (36-43).

12.3.1. Discovery

Prominin-1 was first identified 1997 from neuroepithelial stem cells in mice, where it was named for its prominent location on cell membrane protrusions (29). In the same year, the surface antigen AC133 (CD133) was discovered by generating a monoclonal antibody targeting CD34+ hematopoietic stem cells from fetal liver, bone marrow, and cord blood (33). Subsequent cloning of the protein's cDNA revealed that AC133 is the human counterpart of mouse Prominin-1 (30). A unified nomenclature for the family has been proposed (44).

12.3.2. Structure

Human prominin-1 is encoded by the PROM1 gene, located on chromosome 4p15.32. It consists of 27 exons that undergo alternative splicing, giving rise to multiple isoforms. The full-length isoform of human prominin-1 is a transmembrane protein comprising 865 amino acids. It features five transmembrane domains, a short intracellular C-terminal tail, and a large extracellular N-terminal domain. Notably, the extracellular domain is heavily glycosylated and contains several N-glycosylation sites (27). In mice, prominin-1 shares high homology with its human counterpart and is also encoded by the PROM1 gene (45).

12.3.3. PROMININ-1's Role in the Context of Cancer Stem Cells

Cancer stem cells (CSCs) are a subpopulation of cancer cells that possess self-renewal, differentiation potential, and treatment resistance (46). CD133 (PROM1)-positive CSCs have been shown to initiate solid tumors in mice, while CD133-negative cells do not (34, 35). PROM1 regulates cancer cell differentiation by stabilizing β-Catenin through its interaction with HDAC6 (47), and it is upregulated in hepatocellular carcinoma and glioma stem cells under

hypoxia or IL-6 exposure (48, 49). Other studies have reported increased expression of Prominin 1 in other types of cancer, including brain tumors, colorectal cancer, breast cancer, and lung cancer (50). The expression of Prominin 1 in cancer cells has been associated with tumor aggressiveness, poor prognosis, and resistance to chemotherapy (51).

However controversies have arisen regarding the significance of CD133 as a selective marker for stem cells and its implications for cancer prognosis and progression. These controversies stem from issues such as the use of specific epitopes for immunodetection (e.g., AC133 epitope) and the oversight of general expression of CD133 beyond stem cells in the field (27, 29, 52-54).

12.3.4. Prominin-1 functions as a protein associated with lipid rafts

The association of CD133 with specific lipid rafts could play a role in stem cell biology by being involved in signal transduction and the maintenance of stem cell properties. Loss of this association could lead to cell differentiation, while various processes such as asymmetric cell division and the release of extracellular vesicles may be related to it (55). Furthermore research found that PROM1 might be involved in regulating axon regeneration, by influencing cholesterol metabolism pathways. Manipulating Prom1 expression levels affects genes associated with cholesterol metabolism, leading to changes in cellular cholesterol levels, which in turn impact the regeneration of axons (40).

12.3.5. The role of prominin-1 (CD133) in the eye

In addition to its presence in various organs and tissues, Prominin 1 is physiologically involved in the physiology of the eye. Its role in the formation and regulation of disks within the outer segment (OS) of photoreceptors (56), as well as its involvement in cytoplasmic functions such as the organization of autophagosome maturation and trafficking in the retinal pigment epithelium (RPE), has been elucidated (57, 58).

12.3.6. PROM1 associated retinopathy

Various types of mutations in the PROM1 gene have been identified and have been reported in association with retinal degenerations:

- Missense mutations: This type of mutation involves the substitution of one amino acid in the Prominin-1 protein. For example, a study conducted on a cohort of Chinese

patients identified the association of the PROM1 p.Arg373Cys variant with macular dystrophy plus peripheral bone-spicule degeneration (59).

- Truncating mutations: Truncating mutations result in a shortened or truncated version of the Prominin-1 protein. A premature truncation mutation in the PROM1 gene lead to retinitis pigmentosa with early macular involvement (60).

- Splice site mutations: Mutations at the splice sites of the PROM1 gene can lead to alterations in the splicing process, resulting in abnormal mRNA transcripts and disrupted protein production. A deep intronic variant in the PROM1 gene was found in a family with autosomal recessive cone-rod dystrophy (CRD), resulting in a pseudoexon integration and a putative null allele (61).

- Frameshift mutations: a frameshift mutation is a type of genetic mutation in which one or more nucleotide bases are inserted or deleted in a DNA sequence. This results in a shift in the reading frame during protein translation. Since the genetic code is read in triplets (codons), a frameshift mutation leads to an altered amino acid sequence and often an early stop codon. Frameshift mutations in the PROM1 gene have been identified in association with cone-rod dystrophy (62).

Heterogeneous retinal phenotypes have been reported, ranging from milder forms like bull's-eye maculopathy (BEM) and isolated macular dystrophy to more severe conditions such as panretinal cone, cone-rod, and rod-cone dystrophy (63). Phenotypes can manifest in both autosomal dominant (63) and autosomal recessive forms (64). Despite an increase in the number of reported patients and disease-causing variants in recent years (64-66), only a limited number of pedigrees have been described in the existing literature (63, 67). The onset and progression of these diseases can significantly vary among patients, even within the same family (56, 63, 68, 69), and the molecular mechanisms underlying this variation may be influenced by environmental factors or modifier genes (68).

12.4. Retinal imaging

12.4.1. History of retinal imaging

The first retinal images had been published in 1853 by van Trigt, a Dutch ophthalmologist (70) and even earlier Purkyně presented sketches of his own retinal vasculature (71). In 1891 images of sufficient quality were published in order to be able to identify retinal vessels, as it was done by Gerloff, an German ophthalmologist (72). Gullstrand pioneered the development of the first fundus camera, laying the foundation for the principles that underpin modern-day common fundus cameras (73). The next crucial advancement was the development of fluorescein angiographic (FA) imaging, which uses a fundus camera combined with narrow band filters to create images of fluorescent dye, that is administered into bloodstream at the beginning of the examination (74). Fluorescein angiography – as well as its successor, namely indocyaningreen-angiography – are even today state of the art investigations in clinical routine because they allow particularly an assessment of retinal blood flow; this is of paramount importance for age-related macular degeneration (AMD), Uveitis, especially the posteriorly located ones, and other retinal disease of various origins (75).

However issues with safety and high costs may contribute to it's slow replacement by tomographic imaging modalities that are efficient in their main application: the investigation and image-guided therapy of wet macular degeneration and other forms of macular edema of e.g. diabetic, inflammatory or vaso-occlusive origin.

Another limitation of conventional fundus photography and fluorescein angiography is that they capture the actual three-dimensional anatomy of the semi-transparent retinal tissue in two dimensions, resulting in a certain loss of diagnostic information. In contrast, emerging tomographic methods, provide the otherwise lost depth Information and even enable a pseudo-3D representation by extrapolating and interpolating the acquired data. Initially, the 3-D shape was simulated through stereo fundus photography, invented in 1964 by Allen (76), where multiple images, taken from different angles, were combined by the observer into three dimensional view. Later the development of confocal scanning laser ophthalmoscopy followed, a technique where using a confocal aperture enabled visualization of retinal tissue at different depths, giving impression of 3-D shape. The optics of the eye, however, only allow for about 100 µm of depth resolution for confocal imaging, which makes it inadequate to image retina in it's entirety, since the average retinal thickness measures between 300 to 500 µm (77). With of superluminescent diodes, tomographic imaging came into wide clinical use, particularly with the development of optical coherence tomography (OCT) machines (78).

12.4.2. Technical challenges in fundus imaging

Both light entering the eye and light reflected back from retina must be projected through the pupillary plane in parallel beams (75). Therefore the size of pupil opening has always been a major challenge in retinal imaging (73). Another complicating factor is that the photo and illumination beam paths cannot overlap, as this causes corneal and lens related reflections, resulting in a loss of contrast. Therefore, separate lightpaths are employed in the small pupil plane, which necessitates optical openings just of a few millimeters. As setup in fundus imaging is technically challenging, it required highly expertized photographers and costly equipment in the past. However, in the last 10 years, great efforts have been made to increase the accessibility and user-friendliness of fundus photography, to become less dependent on expensive photographic professionals and recording relevant experience. The following advances are being particularly conducive to this (79):

- The shift from analogue to digital photography, whereby picture archiving and communication systems (PACS) have gained increasing importance in clinical ophthalmology, enabling integration with electronic medical histories

- Increasing awareness of retinal diseases, demanding population-based early detection of funduscopic diseases

- Certain application-related factors as non-mydriatic imaging, digital imaging with near-infrared focusing and standardized imaging methods simplified the use of fundus cameras for non-ophthalmic photographers and increased repeatability.

12.5. Optical coherence tomography (OCT)

Nowadays optical coherence tomography (OCT) is an established imaging technique in ophthalmology that allows for depth determination by measuring the time of light backscatter. Backscatter is induced by variations in refractive indices at tissue interfaces. By analyzing the time it takes for backscattered light to reach the sensor, OCT can distinguish between backscatter from superficial tissues and backscatter from deeper tissues. In OCT, a beam splitter is used to divide the incident light into two beams: the sample arm, representing the retinal tissue, and the reference arm, which reflects light off a reference mirror within the device. The interferogram energy differences between the sample and reference arms are detected by photo sensors, such as charge coupled device (CCD) and complementary metal oxide semiconductor (CMOS), and are subsequently converted into image intensities (80). To obtain a tomographic image, the illuminating beam is scanned across the retina using galvanic mirrors that control its position along the x and y axes. Each x and y location corresponds to an A-scan, which represents a single line of data acquisition. Combining multiple A-scans generates a two-dimensional cross-sectional image known as a B-scan. B-scans provide insights into the spatial arrangement of different tissue layers or structures within the imaged area (81).

12.5.1. Scanning concepts

Improving the efficiency of A-scan acquisition is crucial for reducing motion artifacts, enhancing patient comfort, and achieving higher image resolution. Therefore three key concepts have been developed and enhanced in chronological order:

- Time-domain OCT (TD-OCT): Also referred to as time-of-flight OCT, TD-OCT involves mechanically displacing the reference mirror to different positions, causing variable flight time delays for the reference light arm. However, due to mechanical constraints, TD-OCT is limited to acquiring tens of thousands of A-scans per second. The intensity of each depth is determined based on the interferogram's envelope (80).

- Spectral-domain OCT (SD-OCT): SD-OCT represents a significant advancement in OCT technology. It employs a broadband light source, broader in spectrum than what is typically used in Time-Domain Optical Coherence Tomography (TD-OCT). To spectrally decompose the interferogram, it utilizes a diffraction grating and relies on a linear sensor, which is typically either a Complementary Metal-Oxide-Semiconductor

(CMOS) or a Charge-Coupled Device (CCD). These CMOS and CCD sensors are accountable for capturing and converting the spectral information into electronic signals for subsequent analysis. The Fourier method is then applied to transform the intensity values from the spectral correlograms, enabling quantification of the range of each scatter signal. SD-OCT offers improved imaging speed and a broader depth range compared to TD-OCT (82).

- Swept-source OCT (SS-OCT): SS-OCT stands as the most recent and innovative OCT technique. It utilizes a rapidly modulated light source that sweeps through its central wavelength range, rather than moving the reference arm. This modulation introduces a second label, the wavelength, to the light. The resulting correlograms for specific center wavelengths are time-recorded by a photosensor. To calculate the thickness of tissue scatters within the imaged region, a Fourier transform of the multi-wavelength or spectral interferogram is performed. SS-OCT offers enhanced imaging speed and an expanded depth range (82).

12.5.2. Macular scan techniques

Macular imaging in optical coherence tomography (OCT) involves various scan techniques (80). Macular scans provide valuable insights into the structure and health of the macula, aiding in the diagnosis and monitoring of macular diseases:

- Cross-sectional scans: Cross-sectional scans, the B-scans mentioned earlier, provide a two-dimensional view of the macula, capturing vertical slices of tissue. These scans allow for the visualization of individual retinal layers and the identification of abnormalities, such as fluid accumulation or macular thickening.

- Volume scans: Volume scans, also referred to as 3D scans or cube scans, offer a comprehensive assessment of the macula. By acquiring a series of B-scans in a grid pattern, these scans generate a three-dimensional representation of the macular structure. Volume scans enable detailed analysis of the macula's thickness, volume, and topography, facilitating precise measurements and comparisons over time.

- Radial scans: Radial scans consist of multiple B-scans acquired from a central point and extending outward in a radial pattern. These scans provide a radial view of the macula, capturing its entire circumference. Radial scans are particularly useful for assessing lesions or abnormalities located near the fovea, as they pass through its

central region. Six to twelve line scans at identical angles around a common axis make up the radial scan.

- Raster scans: Raster scans are high-density scans that capture a series of parallel B-scans, covering a specific area of the macula. These scans allow for detailed examination of a particular region of interest, providing a cross-sectional view along multiple axes. Raster scans offer flexibility in scan orientation and can be performed at various angles to capture specific macular features.

- En face scans: En face scans provide a flat, surface-level view of the macula, akin to a photograph. These scans are generated by digitally extracting specific retinal layers or structures from the volumetric data acquired during OCT imaging. En face scans enable detailed visualization of features such as the retinal pigment epithelium, drusen, or macular holes, aiding in the assessment of various macular pathologies.

12.5.3. ETDRS ring

The ETDRS ring, originating from the Early Treatment Diabetic Retinopathy Study (ETDRS) (83) conducted in the 1980s, is a standardized scan grid that was initially developed for assessing and treating diabetic retinopathy. It comprises several concentric circles and rings:

- Central subfield: the area within a 0.5 mm radius from the foveal center
- Inner ring: extending the area from a 0.5 to 1.5 mm radius from the foveal center
- Outer ring: encompassing the region within a 1.5 to 3 mm radius from the foveal center

Since its inception, it has also demonstrated particular effectiveness in quantifying the disease progression of several other retinal pathologies, including Mb Stargardt (84).

12.5.4. Technical challenges in macular OCT-Imaging

There are technical challenges associated with interpreting macular diseases using optical coherence tomography (85):

- Variations in scan duration, density, and resolution among different OCT machines can impact image quality. To mitigate this, it is essential to use standardized scanning protocols and compare results within the same machine or software.

- Insufficient pupil dilation can result in suboptimal OCT images. To address this, it is recommended to ensure a pupil diameter of at least 3 mm to achieve adequate image

quality. Dilating eye drops or alternative techniques can be used to achieve the desired pupil size.

- Aligning the focus of the fundus image and the OCT scan is crucial for accurate interpretation. Refractive errors should be taken into account and corrected to achieve proper alignment. Adjusting the OCT image vertically and positioning the focal point of the reference scan pattern directly above the fovea are essential steps.

- Optimal signal intensity is crucial for obtaining high-quality OCT images. Care should be taken to position the light source in such a way that it enters the eye directly across the pupil. This helps maximize signal strength and minimize artifacts.

- In some cases, multiple scan procedures may be required to capture the necessary information. It is important to repeat the scanning process consistently and ensure proper alignment and focus for each scan.

- After acquiring OCT scans, quantitative and qualitative analyses are performed. However, it is important to consider that analysis reports and measurements may vary between different OCT systems. Familiarity with the specific system and software used is essential for accurate interpretation.

12.5.5. Segmentation of retinal layers

These are the retinal layers, including adjacent structures, that are commonly segmented for diagnostic or scientific purposes in macula-OCT scans. The layers are listed from innermost to outermost (86):

1. Inner limiting membrane (ILM): The ILM is a thin, transparent layer that forms the boundary between the retina and the vitreous humour. It consists of Müller cell end feet and the basement membrane of the retina.

2. Retinal nerve fiber layer (RNFL): The RNFL consists of axons from ganglion cells that form the optic nerve. It carries visual information from the retina to the brain.

3. Ganglion cell layer (GCL): The GCL contains the cell bodies of retinal ganglion cells, which receive visual signals from photoreceptors and transmit them to the brain.

4. Inner plexiform layer (IPL): The IPL contains synapses between bipolar cells, amacrine cells, and ganglion cells. It plays a critical role in the processing and integration of visual signals.

5. Inner nuclear layer (INL): The INL contains the cell bodies of bipolar cells, horizontal cells, and amacrine cells. It serves as an intermediary layer in the visual signal processing pathway.

6. Outer plexiform layer (OPL): The OPL contains synapses between photoreceptor cells (rods and cones) and bipolar cells. It is involved in the transmission of visual signals from photoreceptors to bipolar cells.

7. Outer nuclear layer (ONL): The ONL contains the cell bodies and nuclei of the photoreceptor cells (rods and cones). It is responsible for the production and maintenance of photoreceptor cells.

8. External limiting membrane (ELM): The ELM is a boundary layer between the inner segment (IS) of photoreceptor cells and the outer nuclear layer (ONL). It plays a role in maintaining the structural integrity of the photoreceptor layer.

9. Photoreceptor layer: The photoreceptor layer comprises the outer segments and inner segments. These cells capture and process light, initiating the visual signal.

10. Retinal pigment epithelium (RPE): The RPE is a monolayer of pigmented cells located between the photoreceptor layer and the choroid. It plays a crucial role in supporting and nourishing the photoreceptor cells.

11. Inner choroidal layers (choriocapillaris, Sattler's layer, Haller's layer): The inner choroidal layers consist of the choriocapillaris, Sattler's layer, and Haller's layer, which are part of the choroid. They provide blood supply to the outer retina and play a role in nutrient exchange (86).

Accurate segmentation of macular layers in optical coherence tomography (OCT) scans is essential for quantitative analysis of retinal structures and the detection of abnormalities. Automated and semi-automated segmentation techniques have been developed to enhance accuracy and efficiency in this process. OCT devices often come equipped with software that offers automated pre-segmentation of macular layers, providing an initial segmentation. The software often allows for manual adjustment by clinicians to refine the results.

The Spectralis SD-OCT layer segmentation module, developed by Heidelberg Engineering in Germany, is a commonly used segmentation software that combines intensity-based and edge-based techniques:

- Intensity-based segmentation methods analyze the pixel intensity values in OCT images to differentiate various tissue layers and boundaries. These methods employ thresholding techniques or region-growing approaches based on intensity gradients or statistical properties of the image.

- On the other hand, edge-based segmentation methods focus on identifying layer boundaries by detecting sharp intensity transitions or edges in OCT images. These methods employ edge detection techniques, such as gradient-based methods or edge filters, to accurately locate areas where significant intensity changes occur (87).

Both intensity-based and edge-based segmentation techniques are effective for segmenting well-defined layers with distinct intensity profiles.

Another widely used software is the Topcon 3D OCT-2000 software (Topcon Corporation, Tokyo, Japan), which utilizes a graph-based algorithm for segmenting retinal layers: Graph-based segmentation methods leverage the concept of a graph, representing the OCT image as a network of interconnected nodes. These algorithms approach the segmentation problem as an optimization task, seeking to achieve the most optimal segmentation based on specific criteria. They frequently employ graph-cut algorithms or graph-based clustering techniques to divide the image into distinct regions or layers (88).

12.5.6. Applications

OCT has several indications across various ocular conditions, for example:

- Age-related macular degeneration (AMD) and inherited retinal disease (IRD): OCT aids in the diagnosis and management of AMD and IRD by assessing the presence of drusen, geographic atrophy, loss of photoreceptors and retinal pigment epithelium, and the presence of choroidal neovascularization (89).

- Diabetic retinopathy: OCT is useful for evaluating the presence and severity of diabetic macular edema, detecting macular thickening, and monitoring response to treatment (90).

- Macular holes: OCT is crucial for diagnosing and characterizing macular holes, assessing their size, and evaluating the vitreomacular interface (91).

- Retinal vein occlusion (RVO): OCT helps in identifying macular edema, assessing the extent of retinal ischemia, and monitoring the response to anti-vascular endothelial growth factor (anti-VEGF) therapy (92).

- Glaucoma: OCT provides valuable information for evaluating the retinal nerve fiber layer thickness, optic nerve head, and assessing disease progression in glaucoma (93).

12.6. Fundus autofluorescence (FAF)

The early emergence of autofluorescence imaging can be attributed to the research conducted by Delori et al. in 1995, who is acknowledged as the first to comprehensively investigate the autofluorescent characteristics of lipofuscin (94).

Fundus autofluorescence (FAF) is a non-invasive imaging technique used to visualize fluorophores, naturally occurring molecules that absorb and emit specific wavelengths of light (94).

The excitation of fluorophores in FAF occurs when an electron within the molecule absorbs a photon at the excitation wavelength, causing it to be excited to a higher energy state. As the electron returns to its ground state, it emits light at a longer wavelength. FAF imaging traditionally employs blue-light excitation to capture emissions and create a brightness map reflecting the distribution of fluorophores, particularly lipofuscin, within the retinal pigment epithelium (RPE) and retinal layers (95).

Lipofuscin is composed of bisretinoid molecules, by-products of vitamin A metabolism and the visual cycle, which are deposited in RPE lysosomes over time. Lipofuscin autofluorescence has a peak emission wavelength of 600-610 nm and absorbs blue light with a peak excitation wavelength of 470 nm. Increased levels of lipofuscin have been observed in degenerative conditions such as age-related macular degeneration (AMD) and macular dystrophies. The distribution of lipofuscin is highest in the posterior pole of the retina, lowest in the fovea, and gradually decreases towards the periphery (96).

One well-studied component of lipofuscin is N-retinyl-N-retinylidene ethanolamine (A2E) (97). A2E accumulation in RPE lysosomes has been associated with various degenerative retinal disorders. It has been shown to generate reactive oxygen species (ROS) upon photo-oxidation under blue light and has been linked to detrimental effects on RPE cells (98-102).

However, A2E may also have a protective role in the retina, as it produces singlet oxygen species less efficiently than its precursor all-trans-retinal, potentially shielding the retina from its harmful effects (103, 104).

Furthermore, while A2E is primarily located in the peripheral retina, macular FAF signals are known to predominantly originate from central retinal areas (105, 106).

It has been suggested that the macular pigment acts as a protective filter against blue light and oxidative damage, potentially reducing the formation of lipofuscin and A2E. Higher

macular pigment density has been associated with a lower risk of developing age-related macular degeneration (AMD) (107, 108).

The precise role of A2E and its contribution to retinal pathology are still under ongoing investigation.

12.6.1. Wavelength-specific FAF imaging methods

FAF imaging is commonly performed using the principle of confocal scanning laser ophthalmoscopy (cSLO), which employs laser beams to scan ocular structures (77). Various acquisition techniques have been developed to investigate different fluorophores. These techniques employ specific excitation wavelengths to selectively visualize and analyze distinct fluorophores. Here are several commonly employed wavelength-specific FAF imaging methods:

- Short-wavelength FAF (SW-FAF): SW-FAF utilizes short-wavelength blue light, typically around 488 nm, for excitation. This technique is specifically designed to assess fluorophores such as lipofuscin, which exhibit optimal excitation and emission characteristics in the shorter wavelength range. SW-FAF enables the examination of lipofuscin distribution and accumulation in the retinal pigment epithelium (RPE) and outer retina (94).

- Near-infrared FAF (NIR-FAF): NIR-FAF employs near-infrared light, usually around 787 nm, for excitation. This technique allows for the visualization of other retinal fluorophores, including melanin and choroidal fluorophores. NIR-FAF provides complementary information to conventional FAF, aiding in the evaluation of pathologies involving these specific fluorophores (109).

- Green-absorbing FAF (GAF): GAF utilizes green-absorbing filters to capture autofluorescence emitted by the retina. By selectively blocking shorter wavelength excitation light, GAF imaging enables the detection of longer wavelength emission signals. This technique is particularly valuable for studying the contribution of lipofuscin-related autofluorescence and other fluorophores in various retinal pathologies, for example geographic atrophies (GA) (110).

12.6.2. Advantages and limitations of FAF imaging

Compared to fluorescein angiography, FAF provides additional diagnostic information without the need for intravenous dye injection, hence avoiding risks such as discomfort, redness, nausea, vomiting and pruritus. However, it is important to note certain limitations of FAF imaging. The signal intensity of FAF is significantly lower than that of fluorescein angiography (94). Additionally, artifacts from anterior segment or vitreous opacities, such as cataracts or vitreous opacities, can complicate image interpretation. Standardization across different imaging devices and settings can also pose challenges for result comparison (111).

12.6.3. Quantitative autofluorescence (qAF)

While FAF is mainly used for qualitative analysis and visual interpretation of autofluorescence patterns, one of its main limitations has been the lack of quantitative measurements. In 2011, Delori et al. (112) introduced a clinical imaging tool that allows for the quantification of FAF signal intensities. This imaging device, known as quantitative fundus autofluorescence (qAF), is an adapted scanning laser ophthalmoscope that incorporates an internal standard reference. During the acquisition of each FAF image, the standard reference is simultaneously excited, enabling subsequent normalization of the FAF images to the standard reference signal. This normalization process is independent of camera and image acquisition settings (113). Since its introduction, QAF has been utilized in various studies involving both healthy (114, 115) and diseased eyes, including conditions such as age-related macular degeneration (AMD), hereditary retino-/maculopathies (116, 117), and inflammatory diseases (118).

12.7. Adaptive optics scanning light ophthalmoscopy (AOSLO)

The concept of adaptive optics (AO) is an approach that was initially in astronomy to sharpen photographs by adjusting for blur-causing optical aberrations induced by turbulence in the earth's atmosphere. AO is used in the area of vision research to correct for optical aberration in the eye's optics and may be implemented with any kind of ophthalmoscope modality, from full-field fundus cameras to scanning laser ophthalmoscopies (SLOs) and optical coherence tomography (OCT) devices. Adaptive optics (AO) transforms an ophthalmoscope into a microscope, providing optical access to individual single photoreceptors in real human eyes (119). An AO system requires two crucial steps: to assess the optical flaws of the eye and to correct them. The most popular method for measuring aberrations in the human eye is the Shack-Hartmann Wavefront Sensor (SHWS) (Figure 1). As part of his PhD study at the University of Heidelberg in Germany with Josef Bille (120), Junzhong Liang was the first to build a SHWS for the human eye; it was improved at the University of Rochester (121). Liang, Donald Miller, and David Williams constructed the first AO retinal camera using SHWS technology for ophthalmic purposes (119). At its core was an adjustable mirror that could be reshaped to have aberration equal to and opposite that of the human eye, as recorded by the Shack-Hartmann wavefront sensor (SHWS). As a result, the mirror's imperfections would virtually cancel out the eye's as the light travelled through it (122-124).

Among the ophthalmic imaging techniques, a very suitable technology to apply AO in humans is the scanning laser or light ophthalmoscope (SLO). While scanning over the retina in a raster pattern, the SLO, which was invented in 1980 by Robert Webb (125), continuously records and logs the light dispersed from a single specific area on the retina.

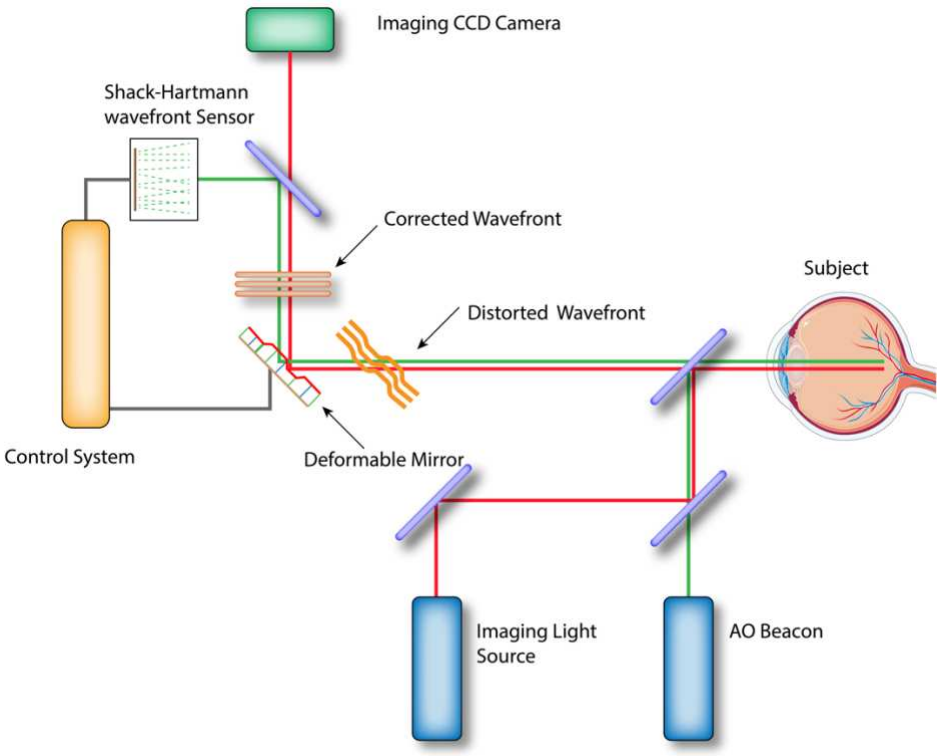

Figure 1 Adaptive optics scheme

A retinal imaging system with adaptive optics is shown in a schematic picture. Using a wavefront sensor, an AO system detects the aberrated wavefront, which is then adjusted by a wavefront corrector. These typically consist of a Shack-Hartmann Wavefront Sensor (SHWS) and a deformable mirror. A central control system links these two components together. The AO-corrected retinal picture is captured using a high-resolution camera.

Adapted from Gill et al. (126). This Figure is authorized under a Creative Commons Attribution 4.0 International License (3).

The most prevalent scanning mode for AOSLO is confocal imaging, in which a tiny aperture (confocal pinhole) is positioned near to the detector and is optically conjugate to the point of focus on the retina. The confocal pinhole prevents dispersed light from reaching the detector, with the exception of light that originates close to the plane of focus. The use of this confocal pinhole permits optical sectioning, which is the major benefit of confocal microscopes over traditional light-field microscopes (albeit not as precise as OCT's ability for axial scanning), and it also offers high contrast pictures of the target structure. Cones may be seen using a confocal detector due to their waveguiding capacity, which is believed to be dependent on undamaged photoreceptor outer segments (OS) (127-129). Yet another advancement was the split detection approach, which utilizes non-confocal backscattered beams to reveal photoreceptor inner segments. It achieves that by using two detectors to capture the light to the left and right

of the confocal aperture, then calculating the subtraction of pictures divided by their total (Figure 2) (130, 131).

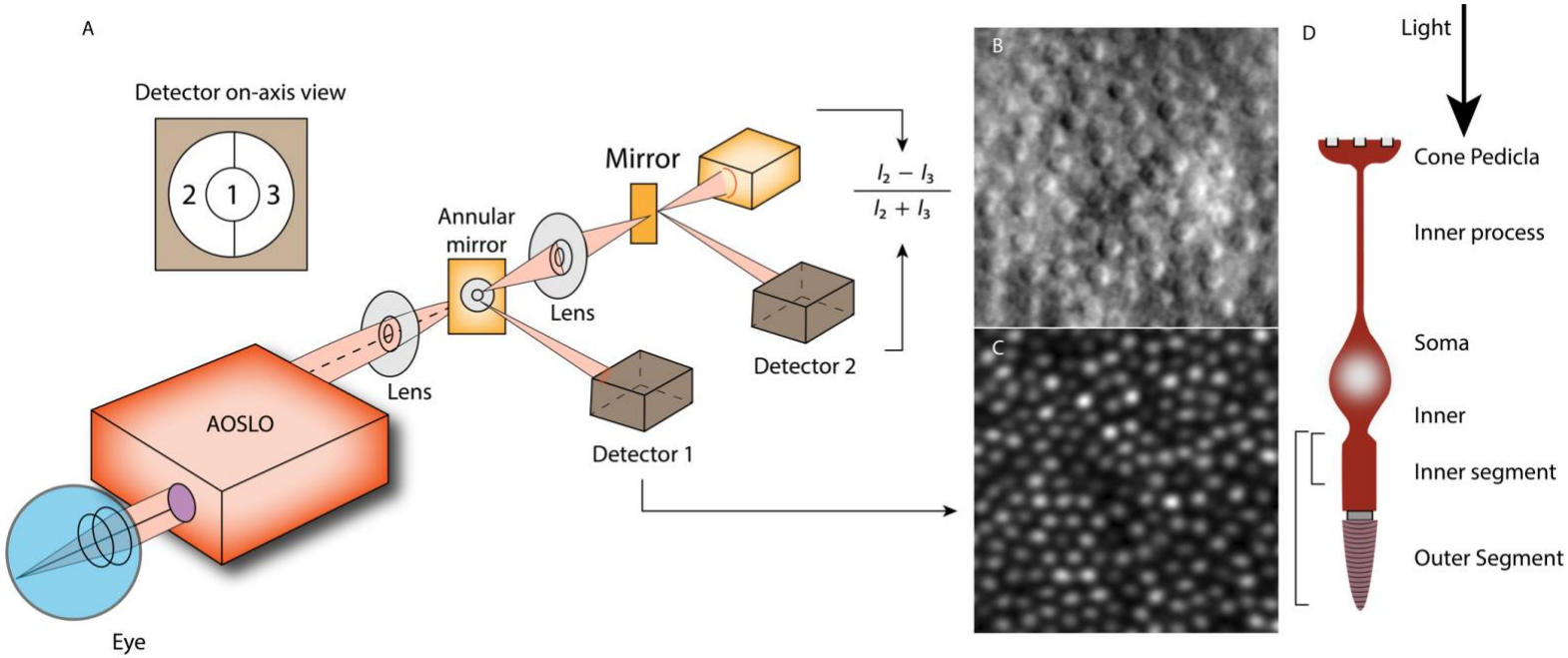

Figure 2 AOSLO split-detector implementation

Images and implementations of the split detector shown in schematic form. (A) AOSLO drawing with an annular reflecting mirror (inset) to split the confocal light from the multiple-scattered beams, which are subsequently distributed evenly between two further detectors. The confocal signal is recorded directly in Detector 1, while split-detector input is the result of subtracting the intensities recorded in Detector 2 from those recorded in Detector 3 and dividing the result by the total of signal intensity at each pixel. (B) Split-detector picture of the photoreceptor inner segment mosaic taken at 10° of visual angle from fixation in a healthy subject, displaying cones and an inability to discern individual rods. (C) Cones with wide - ranging reflectivity are encircled by rods in this simultaneously captured confocal picture. Scale bar: 25 µm. (D) The potential source of light back reflections is shown on a photoreceptor illustration The images labeled B and C were obtained from patient P1 presented in this thesis. AOSLO stands for Adaptive Optics Scanning Light Ophthalmoscopy. Adapted from Scoles et al. (131) with authorization from the copyright owner the Association for Research in Vision and Ophthalmology (ARVO) (4).

12.8. Outcome measures for IRDs

Clinical trials for IRDs require special considerations regarding outcome measurements. In general, the measurements should show a high degree of reliability and repeatability, ideally in comparison with normative data. In earlier retinal studies, visual acuity was often used as the primary endpoint parameter, which does not appear to be ideal in the case of IRD, since in the case of centripetal atrophies, for example, the macula is only affected in later stages of the disease. A change of ≥15 letter values (corresponds to ≥3 lines with a standardized visual acuity) is considered significant, values that subjects with central atrophies hardly reach (132).

The NEI/FDA Endpoints Workshop on Age-Related Macular Degeneration and Inherited Retinal Diseases (133), commissioned by the National Eye Institute (NEI) and the U.S. Food and Drug Administration (FDA), aimed to address challenges in assessing disease progression and treatment responses through discussions on various endpoints. These included:

- Disease progression measures: Participants discussed the importance of utilizing advanced imaging techniques, such as optical coherence tomography (OCT), to evaluate structural changes in the retina. These measures could include the assessment of drusen volume, retinal thickness, and geographic atrophy progression.

- Visual function assessments: Experts emphasized the need for functional endpoints to evaluate visual acuity, contrast sensitivity, and visual field defects. These assessments help determine the impact of the disease on patients' visual capabilities.

- Quality of life and patient-reported outcomes: The workshop highlighted the value of including patient-reported outcomes to capture the impact of the disease on daily activities, emotional well-being, and overall quality of life. Questionnaires and surveys were considered as potential tools to gather this information.

- Biomarkers: Discussions also revolved around identifying reliable biomarkers, such as genetic markers, biochemical indicators, or specific protein levels, that could serve as objective measures of disease progression and treatment response.

12.9. ProgStar- 4 study

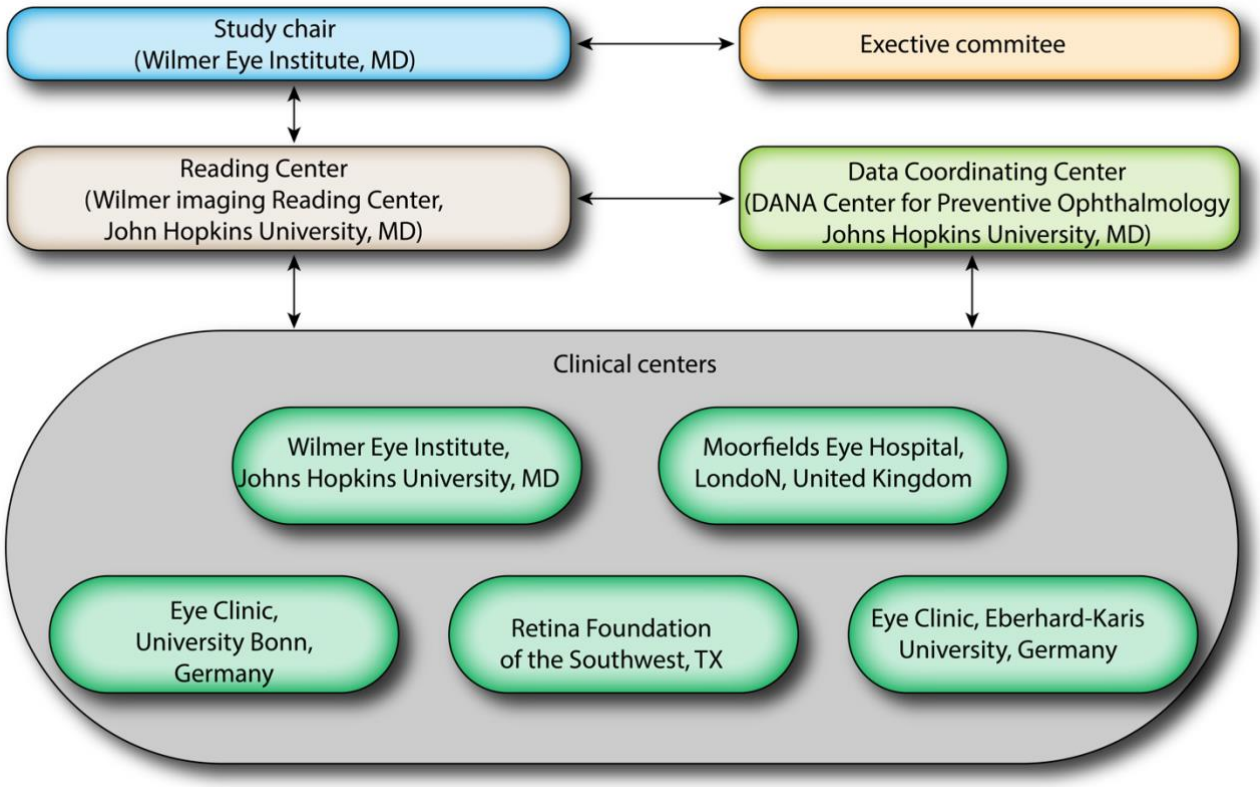

Figure 3 Organizational structure of the ProgStar-4 study group

Adapted from Strauss et al. (57) with authorization from the copyright owners Karger AG (5).

To assess the natural course of PROM1-related retinopathy, the Natural History of the Progression of Atrophy Secondary to Stargardt Disease Type 4 study (ProgStar-4), a prospective longitudinal observational cohort, has been initiated (57). The ProgStar-4 study investigated 15 individuals for two years. There were a total of 5 study visits (1 initial and 4 subsequent visits every 6 months for 24 months), with a five-week timeframe for each visit. A clinical assessment, including refraction and best-corrected visual acuity (BCVA) testing, central visual field testing with mesopic and scotopic microperimetry (MP), and retinal imaging with fundus autofluorescence (FAF) and spectral-domain optical coherence tomography (SD-OCT), was conducted.

The primary objective was to determine annual rate of progression of STGD4 utilizing FAF imaging to measure growth of atrophic lesions. These were the secondary goals:

- to determine the rates of retinal thinning and photoreceptor loss employing SD-OCT

- to evaluate the annual rate of decrease of retinal sensitivity as indicated by mesopic and scotopic MP
- to investigate the rate of BCVA changes per year
- to assess correlation between FAF and SD-OCT with visual function represented by MP and visual acuity
- exploratory investigation of variables related with progression, such as the patient's smoking history

The baseline characteristics of the ProgStar-4 study have been published previously (57). Nevertheless, it remained uncertain whether the selected modalities could effectively monitor progression in all patients and whether potential endpoints could be established. There is also a limited understanding of how PROM1 sequence variants specifically impact cone photoreceptors. Therefore, the Moorfields Study Group has launched a program employing a custom-built adaptive optics system to investigate patients affected by Inherited Retinal Disorders (IRDs). This system allows for the visualization of not only cones but also rods (134).

13. Materials and methods

13.1. Purpose

The purpose of this study was to investigate retinal structure and function in individuals with autosomal-dominant (AD) and autosomal-recessive (AR) PROM1-associated retinal degeneration (PROM1-RD), specifically with regard to cone photoreceptors. The following multimodal imaging techniques were employed to assess retinal structure down to the cellular scale:

- Fundus autofluorescence (FAF)
- Spectral-domain optical coherence tomography (SD-OCT)
- Adaptive optics Scanning light ophthalmoscopy (AOSLO)

13.2. Research question

What is the impact of PROM1 sequence variants on retinal structure and function, specifically with regard to cone photoreceptors in individuals with autosomal dominant and autosomal recessive PROM1-associated retinal degeneration?

13.3. Outcome measures

- Ocular examination including best-corrected visual acuity (BCVA) according to ETDRS protocol and biomicroscopy of the anterior segments.
- Size of present areas of definitely decreased autofluorescence (DDAF) and questionably decreased autofluorescence (QDAF) in mm² as determined by fundus autofluorescence (FAF).
- Mean total retinal thickness and mean thicknesses of individual layers, including outer segment (OS), inner segment(IS), retinal pigment epithelium (RPE), inner retina (IR) and outer nuclear layer (ONL), were assessed using spectral-domain optical coherence tomography (SD-OCT) in the central subfield (area within a 0.5 mm radius from the foveal center), inner ring (area within a 0.5 to 1.5 mm radius from the foveal center), and outer ring (area within a 1.5 to 3 mm radius from the foveal center).

- Primary endpoint: mean peak cone density (PCD) and mean (± SD) cone densities in cones/mm² for distinct regions of interest (ROIs) away from the foveal center (1°, 2°, and 5°) as determined by adaptive optics scanning light ophthalmoscopy (AOSLO).

13.4. Study design

Institutional longitudinal cohort encompassing two distinct assessments: the baseline examination and a subsequent follow-up after a 24-month interval. Due to limited follow-up data, the publication that evolved from this thesis has been published as a cross-sectional study (1), with the addition of longitudinal assessments for two patients. Furthermore, the study has a comparative aspect, as outcome measures determined by one imaging modality (SD-OCT) are compared to normative data. The comparative aspect is further elaborated in the thesis.

13.5. Selection of trial participants

The procedures employed for selecting trial participants were the same as those for the ProgStar-4 study (57):

13.5.1. Inclusion criteria

- There needed to be disease-causing variant(s) in the PROM1 gene
- The primary study eye had to have clear ocular media and adequate pupillary dilation to permit good-quality imaging, as determined by the investigator.
- The patient should have been able to cooperate in performing the examinations.
- There needed to have been a willingness to undergo ocular examinations once every 6 months for up to 24 months.
- The minimum age at the baseline visit had to have been 6 years.
- Both eyes could have been included if the inclusion criteria were fulfilled for both eyes.

13.5.2. Exclusion criteria

- Any ocular diseases, such as choroidal neovascularization, glaucoma, and diabetic retinopathy, in either eye that could potentially affect the assessment of retinal morphology and function.

- Recent intraocular surgery in the primary study eye within 90 days prior to the baseline visit.

- Current or previous participation in an interventional study involving treatments for STGD4, such as gene therapy or stem cell therapy. Current participation in a drug trial or previous participation in a drug trial within 6 months prior to enrolment. The use of oral supplements of vitamins and minerals was allowed.

- The site principal investigator had the authority to deem any patient at their site ineligible for participation in the study based on valid medical reasons before the patient's enrolment.

- Any systemic disease with a limited prognosis for survival, such as cancer or severe/unstable cardiovascular disease.

- Any condition that would make it difficult or unlikely for the patient to adhere to the examination schedule of attending regular follow-up visits once every 6 months for up to 24 months, such as personality disorder, use of major tranquilizers like Haldol or phenothiazine, chronic alcoholism, Alzheimer's disease, or drug abuse.

- Evidence of significant uncontrolled concomitant diseases in cardiovascular, neurological, pulmonary, renal, hepatic, endocrine, or gastrointestinal systems. However, there were no specific restrictions on visual acuity for eligibility in the ProgStar-4 study.

13.5.3. Recruitment

The potential study participants were selected from the Moorfields Eye Hospital (MEH) patient pool (17) who were referred there by eye specialists or self-referred. A detailed clinical history was obtained from the patient. This included information about the presence of symptoms, the age at onset of symptoms, and the order in which symptoms appeared, including issues related to night vision problems, central vision disturbances, photophobia or hemeralopia. A full medical history and family history were also recorded, including the construction of a pedigree. Patients underwent ophthalmic examinations, including assessments of visual acuity and

intraocular pressure, slit-lamp biomicroscopy, and retinal imaging techniques such as spectral-domain OCT. Short-wavelength fundus autofluorescence was used when applicable. In some cases, electroretinography was also performed. If the IRD specialist suspected the presence of an inherited retinal disease (IRD), genetic testing was discussed as a potential diagnostic option. Genetic testing, utilizing either Sanger sequencing or next-generation sequencing, was conducted by the retinal genetics service at MEH (17).

13.5.4. Drop-out

A single participant would be considered a drop-out in the event of any of the following situations:

- The participant's withdrawal of their informed consent.
- Meeting one of the exclusion criteria.
- If the participant's health would be negatively impacted by continuing in the study.

Additionally, patients had the option to discontinue their participation in the trial at any time without the need to provide reasons, and this decision would not have any adverse effects on their subsequent medical care.

13.6. Approval

The study was approved by the Ethics Committee of MEH. All patients signed informed consent prior to enrollment. The research followed the tenets of the Declaration of Helsinki (135).

13.7. Examinations

All examinations were carried out at the MEH. The evaluation of the collected data was carried out within the context of this thesis. To access the necessary software for grading of data of the respective structural imaging modalities TeamViewer remote access was used.

13.7.1. Ocular examination

The ocular examination consisted of measuring best-corrected visual acuity (BCVA) following the Early Treatment of Diabetic Retinopathy Study (ETDRS) protocol, as well as anterior segment biomicroscopy. Dilation of the eyes was achieved using Tropicamide 1% and

phenylephrine 2.5% eye drops prior to funduscopy and all imaging procedures. AOSLO imaging was performed on the right eye of each patient.

13.7.2. Characterization of PROM1 associated retinal degeneration by fundus autofluorescence

FAF images were captured using a customized software designed exclusively for this purpose (136). This software incorporated the technique of short-wavelength reduced-illuminance autofluorescence imaging, as outlined by Cideciyan et al. (136-138). Two independent graders, Gernot Schließleder and Rupert Wolfgang Strauß, evaluated atrophic lesion areas in µm² using established grading protocols and the Heidelberg Eye Explorer version 6.3.4.0 (137). The optic nerve head and retinal vessels were utilized as reference points for the "100% level of darkness," while the peripheral retinal background autofluorescence served as the benchmark for normal autofluorescence. Regions with a darkness level equal to or exceeding 90% in comparison to the optic nerve head or blood vessels were classified as "definitely decreased autofluorescence" (DDAF), whereas areas with darkness levels ranging from 50% to 89% were categorized as "questionably decreased autofluorescence" (QDAF) (57, 137, 138).

13.7.3. Characterization of PROM1 associated retinal degeneration by spectral-domain optical coherence tomography (SD-OCT)

A Heidelberg Spectralis OCT device was utilized to capture an infrared reflectance image and a 20° x 20° volume scan consisting of 49 B-scans, centered onto the anatomical fovea (Automatic Real Time; ART mean of ≥9 frames) (84). Two independent graders (Gernot Schließleder, Manuel Großpötzl), with the involvement of a senior investigator (Rupert Wolfgang Strauß) in cases of disagreement, independently assessed the images. Ungradable images with insufficient quality were excluded from the analysis. For viewing, annotating, and quantifying the OCT scans, an OCT grading application called OCTOR 3.0, developed by Doheny Image Analysis Laboratory (DIAL) and validated at Doheny Imaging Reading Center, was employed (84). Automated segmentations generated by a DIAL algorithm served as the initial reference for manual adjustments and quantitative assessment using OCTOR 3.0, as previously described (84). The thickness measurements of individual layers were derived from grading for the inner subfield, inner ring, and outer ring of the ETDRS subfield grid (84). Adopting the grading method, at least 25 out of 49 B-scans per volume scan were evaluated

per eye/visit (139). In each selected B-scan, the following boundaries, ordered from innermost (anterior) to outermost (posterior), were segmented:

- Inner Limiting Membrane (ILM)
- Inner Boundary of Outer Plexiform Layer (OPL)
- External Limiting Membrane (ELM)
- Inner Segment-Outer Segment (IS-OS) Junction or Ellipsoid Zone (EZ)
- Photoreceptor Outer Segment Layer (OS)
- Retinal Pigment Epithelium (RPE) Inner Boundary
- Inner Choroid Boundary (ICB)

By applying these boundaries, the following layers were outlined and segmented:

- Mean Inner Retinal Thickness (IR): generated from the two boundaries: Inner Limiting Membrane (ILM) and Inner Boundary of Outer Plexiform Layer (OPL)
- Mean Outer Nuclear Layer Thickness (ONL): Inner Boundary of OPL and External Limiting Membrane (ELM)
- Mean Inner Segment Thickness (IS): ELM and Inner Segment-Outer Segment (IS-OS) Junction or Ellipsoid Zone (EZ)
- Mean Outer Segment Thickness (OS): IS-OS Junction or EZ and Inner Boundary of Retinal Pigment Epithelium (RPE) Cell Layer
- Garbage Zone (GZ): Photoreceptor Outer Segment Layer (OS) and RPE Inner Boundary
- Mean RPE Thickness and Intact Area: RPE Cell Layer Inner Boundary and Inner Choroid Boundary (ICB)
- Mean Total Retinal Thickness (TR): ILM and Inner Choroid Boundary (ICB)

In B-scans where a given layer had been completely absent, the immediately adjacent posterior boundaries were snapped together resulting in a thickness value of 0. In case of

tissue accumulations between OS and RPE, such as lipofuscin, OS limited the inside of the debris, the so called “garbage zone” (GZ). The thickness of this layer was subtracted when calculating total retinal thickness (TR). If thickness of garbage zone was 0, OS line corresponded to RPE inner layer.

Adapted from Schließleder et al. (1) with authorization from the copyright holders BMJ Publishing Group Ltd (2).

13.7.3.1. Statistical analysis

Mean retinal thicknesses (µm) of individual layers were calculated separately for each eye in the outer ring, inner ring, and central subfield of the ETDRS-ring. Subsequently, the overall mean thicknesses of retinal sublayers in the study eyes (n=4) were calculated and compared with normative data from 20 healthy, age-matched individuals either within or greater than the SD from the normal mean. The Welch’s unpaired t-test was chosen due to unequal variances and differing sample sizes. We considered the differences to be highly significant ($P < 0.01$), significant ($P < 0.05$), or not significant. The statistical calculations were conducted using GraphPad (140). The comparison further assessed whether the means for each eye individually fell within or exceeded the standard deviations (SD) from the mean values observed in the normative data.

13.7.4. Characterization of PROM1 associated retinal degeneration by AOSLO imaging of the photoreceptor mosaic

A custom-built AOSLO system at Moorfields Eye Hospital (MEH)/UCL Institute of Ophthalmology, London, UK, was utilized to perform AOSLO imaging on all six participating subjects. This imaging approach involved the simultaneous application of confocal and split detection (non-confocal) techniques. Image sequences comprising a minimum of 150 frames each were acquired, covering the central retina or the preferred retinal locus, as well as strips extending from the fovea to 5 degrees in the temporal, superior, nasal, and inferior directions. Prior to subsequent analysis, each image sequence underwent processing through a desinusoiding algorithm, followed by the selection, registration, and averaging of individual frames to improve the signal-to-noise ratio (141).

Subsequently, the resulting images were consolidated into a single montage using Adobe Photoshop and custom-built automated software, with different detection schemes represented in separate layers (142). The scaling procedure was performed as previously described (143), involving the determination of degrees per pixel in an image featuring a

Ronchi ruling with a known spacing. The obtained value was then linearly scaled using the subject's axial length. For quantitative evaluation of AOSLO imaging, peak cone density was utilized, involving the extraction of cone coordinates from foveal images through manual annotation by Gernot Schließleder and validation by a single experienced grader (Melissa Kasilian). Whenever feasible, peak foveal cone density (PCD) in cones/mm² was assessed using coordinate arrays. Mean cone density was determined at various locations by calculating the average of two 55µm square sampling windows, with corresponding regions of interest (ROIs) identified within the cone mosaic (143, 144). In the case of non-foveal measurements, the distances from the center of the ROIs to the PCD in the inferior, nasal, superior, and temporal directions were recorded. The ROIs were then cropped and imported into custom software called MOSAIC (Translational Imaging Innovations, Rayleigh, NC), where cone counting was conducted by Gernot Schließleder and validated by two experienced graders (Melissa Kasilian and Navjit Singh) using split-detection imaging (141). Bound cone density was calculated by dividing the total number of bound Voronoi cells within an ROI by the total bound Voronoi area within the ROI, as previously outlined (129, 145). A qualitative assessment of the mosaics was performed (141). Rigorous eligibility criteria were applied for AOSLO analysis, resulting in the exclusion of low-quality images due to involuntary eye motion or low signal-to-noise ratio, as well as non-contiguous montages, from further analysis.

Adapted from Schließleder et al. (1) with authorization from the copyright holders BMJ Publishing Group Ltd (2).

14. Results

Twelve patients belonging to four pedigrees were identified as having potential disease-causing variants in the PROM1 gene at Moorfields Eye Hospital (MEH), London, UK. Among them, six patients were enrolled in the ProgStar-4 study (57). Additionally, these six patients were invited to participate in the Deep phenotyping of PROM1-associated RD (retinal degeneration) study (1) at MEH, which corresponds to the publication of this thesis. AOSLO Montages suitable for analysis, meeting the criteria of adequate image quality, were successfully obtained in the right eyes of four patients on at least one occasion, with two patients also providing longitudinal data. In the context of PROM1-RD, several factors posed challenges and limitations to the acquisition of high-quality images. These included unstable fixation and extensive areas of atrophy where no discernible structures could be identified.

Adapted from Schließleder et al. (1) with authorization from the copyright holders BMJ Publishing Group Ltd (2).

14.1. Demographic characteristics and ocular examination

The demographic characteristics and the visual acuity of all 4 study subjects are provided in Table 1. In terms of genetic nomenclature, we used the notation provided by the Human Genome Variation Society (146). Three patients carried autosomal dominant (AD) mutations, and one had an autosomal recessive (AR) mutation in the PROM1 gene. P2, harbouring a documented recessive mutation, also exhibited a novel insertion/deletion, namely PROM1(N-M_006017.3):c.630_c.630+8delGGTAAAAACinsAACTT- GAATGAAA, which was classified as pathogenic according to the American College of Medical Genetics guidelines (147). Patient P3 is the mother of patient P4. All our patients identified as White/Middle Easterns.

All patients exhibited normal anterior segments. At the initial visit, the Best Corrected Visual Acuity (BCVA) spanned from 35 to 88 ETDRS letters. In eyes for which we had a follow-up examination (P3, P4), visual acuity had decreased.

Adapted from Schließleder et al. (1) with authorization from the copyright holders BMJ Publishing Group Ltd (2).

Table 1: Demographic characteristics and visual acuity

Provided are patient age at the first visit, mutations in the prom1 gene, inheritance patterns, and best-corrected visual acuity (BCVA) measurements in the right eye. ETDRS score stands for Early Treatment Diabetic Retinopathy Study visual acuity.

Patient	Age	Mutation	Inheritance	BCVA (Right Eye)
P1	45	PROM1 c.1117C>T p.(Arg373Cys)	AD	ETDRS score of 88 letters
P2	31	PROM1(NM_006017.3):c.1354dup (p.Tyr452LeufsTer13)	AR	ETDRS score of 55 letters
		PROM1(N-M_006017.3):c.630_c.630+8delGGTAAAAACinsAACTT- GAATGAAA		
P3	54	PROM1 c.1117C>T p.(Arg373Cys)	AD	ETDRS score of 35 letters (first visit) ETDRS score of 5 letters (after 24 months)
P4	31	PROM1 c.1117C>T p.(Arg373Cys)	AD	ETDRS score of 80 letters (first visit) ETDRS score of 70 letters (after 24 months)

14.2. Findings in FAF imaging

14.2.1. Individual characterizations, including longitudinal assessment of P3 and P4

P1 Fundus autofluorescence (FAF) imaging revealed regular appearance of the foveal center, surrounded by numerous small spots exhibiting both decreased and increased autofluorescence intensity (Figure 4 Panel A), his region of heterogeneity measured approximately 20.83 ± 0.16 mm².

P2 FAF imaging demonstrated a central region of definitely decreased autofluorescence (DDAF) measuring 0.49 ± 0.01 mm², accompanied by surrounding areas of questionably decreased autofluorescence (QDAF) and additional QDAF spots with a combined area of 0.21 ± 0.02 mm² (Figure 4 Panel B). The posterior pole exhibited predominantly preserved and homogeneous autofluorescence patterns.

P3 FAF revealed a central DDAF lesion measuring 1.45 ± 0.02 mm², with a total lesion size of DDAF and QDAF of 8.82 ± 0.22 mm² (Figure 4 Panel C). After 24 months, the lesion size of DDAF increased to 1.79 ± 0.91 mm², and the total lesion size (DDAF + QDAF) was 9.42 ± 0.27 mm² (Figure 4 Panel D).

P4 FAF imaging did not reveal any areas of DAF, but faint dot-like discrete hyperautofluorescence was observed, resembling that seen in P1 (Figure 4 Panel E). However, these were too faint for reliable delineation. After 24 months, FAF imaging remained unchanged (Figure 4 Panel F).

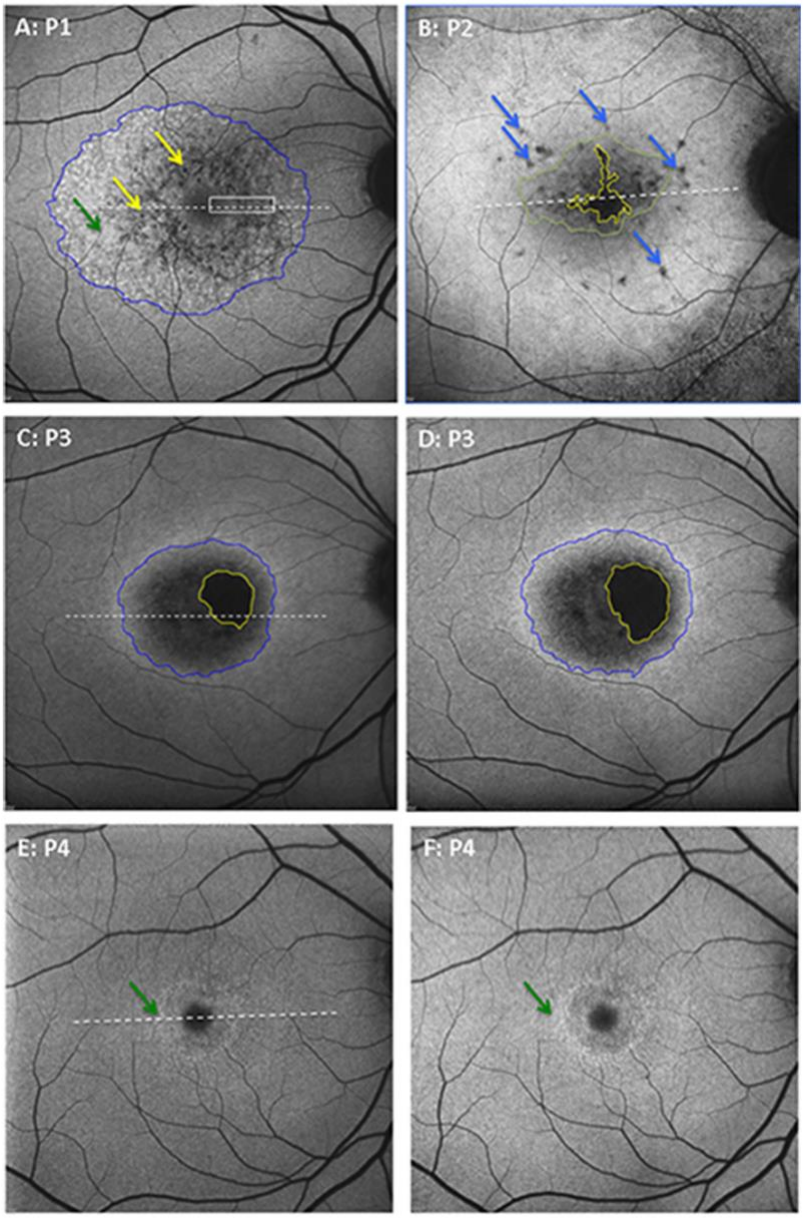

Figure 4 FAF Imaging and grading of the four study eyes

A: In P1, the fovea displayed the expected reduction in fundus autofluorecence (FAF) due to photopigments in the photoreceptor outer segments and macular pigment. Definitely decreased autofluorescence areas (DDAF) are denoted by yellow arrows, while there is surrounding hyperautofluorescence indicated by a green arrow. A complete lesion showing AF heterogeneity is enclosed by a blue line measuring 20.83 mm². The white dashed line marks the location of the spectral-domain optical coherence tomography (SD-OCT) B-scan in figure 7, P1. The white rectangle delineates the area analyzed for cone densities in figure 9. B: P2 exhibits a central DDAF lesion (yellow line), surrounded by an area of questionable decreased AF (QDAF; green line) along with additional small areas of QDAF (blue arrows). The white dashed line designates the location of the SD-OCT B-scan in figure 7, P2. C, D: In P3, DDAF (yellow line) and QDAF (blue line) lesions were observed at the initial visit (C) and after 24 months (D). The white dashed line in C indicates the location of the SD-OCT B-scan in figure 7, P3. E, F: FAF images of P4 at the initial visit and after 24 months.

No areas with reduced AF were observed; instead, there were tiny and faint hyperautofluorescent spots (green arrows). The white dashed line in panel E signifies the location of the SD-OCT B-scan in figure 7, P4.
Adapted from Schließleder et al. (1) with authorization from the copyright holders BMJ Publishing Group Ltd (2).

14.3. Findings in SD-OCT imaging

14.3.1. Cross-sectional comparison to normative database

Mean retinal thicknesses (µm) of individual layers were calculated separately for each eye in the outer ring, inner ring, and central subfield of the ETDRS-ring after manual correction and centration onto the anatomical fovea at the time of the first visit (Figure 5 illustrates the annotation process, while Figure 6 demonstrates the division of zones within the ETDRS grids to preserve the values). Then the overall mean thicknesses of retinal sublayers (n=4) were calculated and compared to normative data (n=20). The results are displayed in Table 2. Notably, significant differences in retinal thickness were observed in several regions. In the following, we consider the differences to be highly significant ($P < 0.01$), significant ($P < 0.05$), or not significant:

- Mean outer segment thickness displayed highly significant reductions in the outer ring, inner ring, and central subfield.
- The mean outer nuclear layer exhibited a highly significant reduction in the inner ring and a significant decrease in the outer ring and central subfield.
- Mean total retinal thickness showed a highly significant decrease in the inner ring and a significant reduction in the outer ring and central subfield.
- The mean retinal pigment epithelium displayed significant reductions in the inner and outer rings, with no significant thinning in the central subfield.
- The mean inner segments thickness demonstrated significant reductions in the inner ring, with no significant thinning in the outer ring and central subfield.
- The mean inner retina exhibited no significant differences at all examined locations.

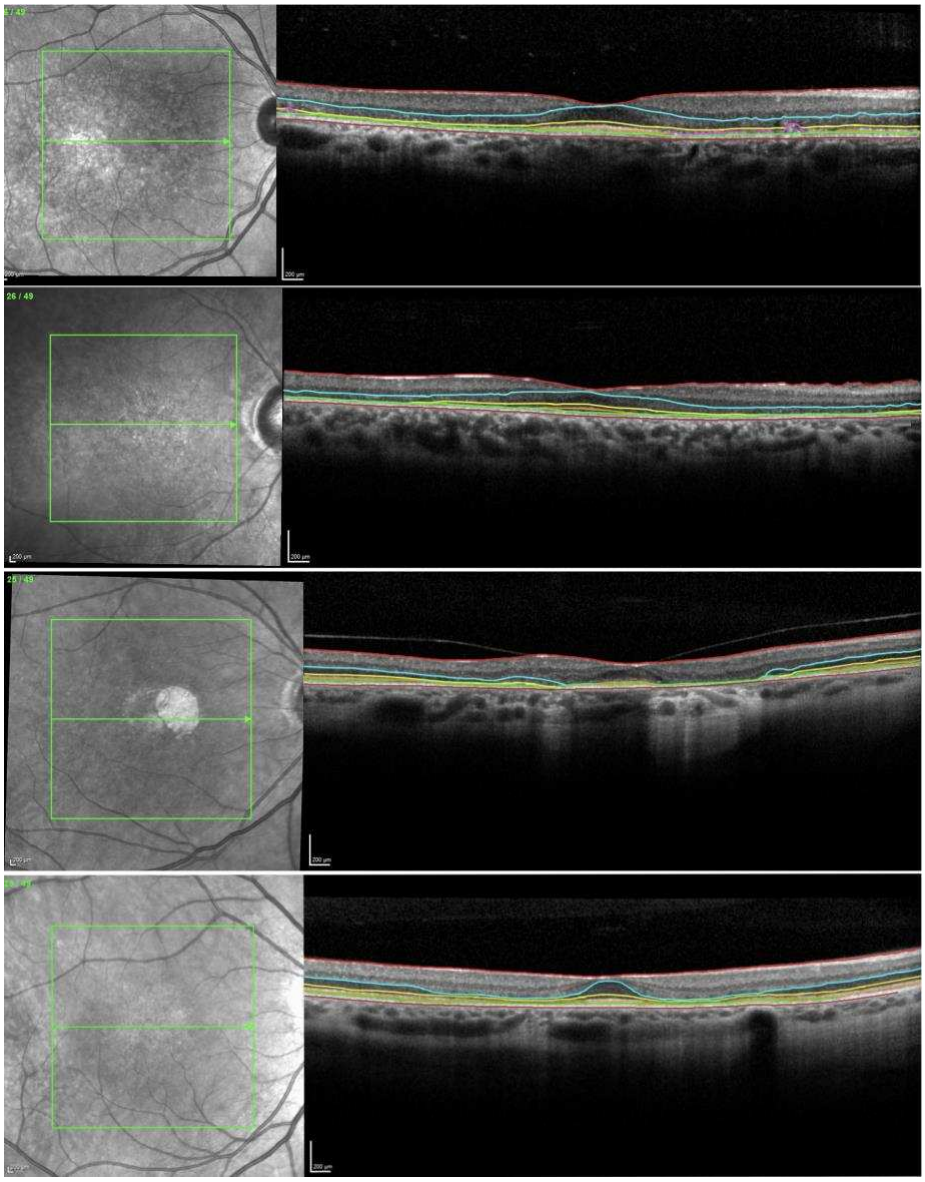

Figure 5 OCT segmentation at the time of first visit

On the left side, en face (infrared) images of the mid-retinas are displayed, arranged in numerical order from P1 to P4 from top to bottom. On the right side, the segmentation of anatomical layers in the most central OCT section of the four patients is presented, color-coded according to the legend: inner limiting membrane (red); inner boundary of outer plexiform layer (blue); external limiting membrane (yellow); inner segment-outer segment junction or ellipsoid zone (orange); photoreceptor outer segment layer or garbage zone inner boundary (purple); inner retinal pigment epithelium boundary (green); inner choroid boundary (brown). In the top-right image (P1), a small bump-like elevation beneath the purple line was identified as the "garbage zone" and subsequently excluded from thickness calculations. In the third image from the top on the right side (P3), certain lines folded downward and overlapped, indicating significant atrophy in the corresponding layers.

Adapted from Schließleder et al. (1) with authorization from the copyright holders BMJ Publishing Group Ltd (2).

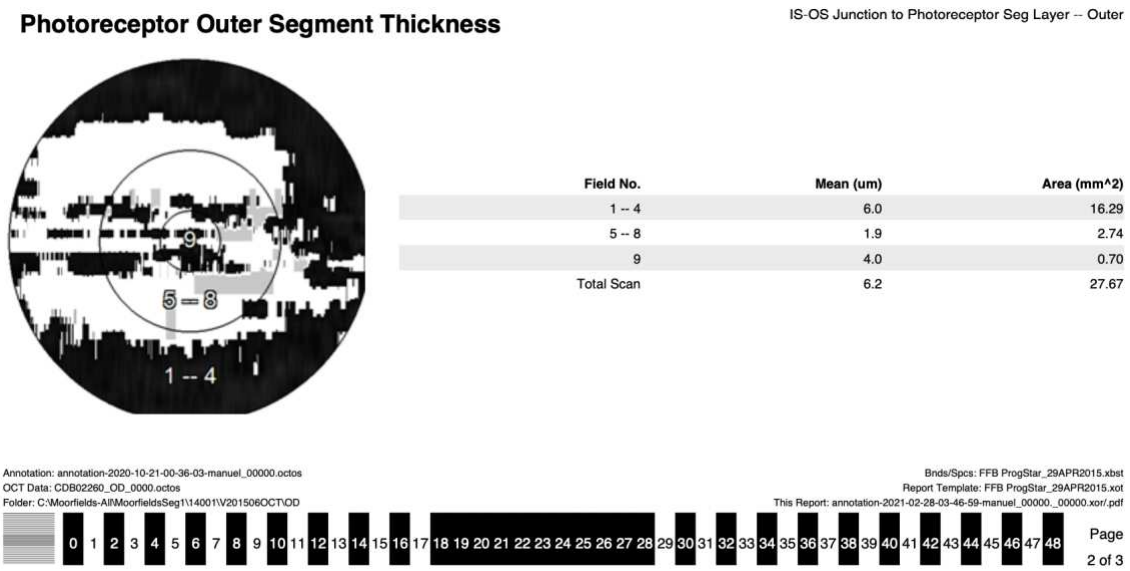

Figure 6 Octor report of photoreceptor outer segment thickness

An exemplary report from our annotation software after grading the photoreceptor outer layer of P3 is displayed. On the right, Fields 1-4 represent the outer ring (3 mm radius from the anatomical fovea), Fields 5-8 correspond to the inner ring (1.5 mm radius), and Field 9 to the central subfield (0.5 mm radius). The outlined ETDRS grid on the left is depicted in white for measurements approaching zero, black for high values, and gray in between. A whitish area that fills the inner ring considerably and also extends beyond is visible, indicating a substantial outer segment/bulls-eye atrophy with a correspondingly lower mean thickness in Fields 5-8 on the right. At the bottom, black indicates segmented slices included in the means calculation, while white represents omitted slices. A minimum of 25 of the 49 slices were evaluated per eye/visit to calculate mean retinal thicknesses.

Table 2 Mean retinal thickness at the time of first visit and comparison to norm database

The mean retinal thickness (in µm) for individual layers in the study eyes is presented for the outer ring, inner ring, and central subfield of the ETDRS ring. These individual eye means were then used to calculate the overall mean thickness, which was compared to the mean data of healthy subjects (n=20) using Welch's unpaired t-test. We observed significant reductions in retinal thickness across various layers.

Adapted from Schließleder et al. (1) with authorization from the copyright holders BMJ Publishing Group Ltd (2).

	Retinal Pigment Epithelium			**Outer Segments**			**Inner Segments**		
	Outer Ring	Inner Ring	Central Subfield	Outer Ring	Inner Ring	Central Subfield	Outer Ring	Inner Ring	Central Subfield
P1	20	16.1	23.4	6	1.9	4	32.7	23.1	39.4
P2	19.5	19.8	21.1	0.3	0.5	5.4	30.6	5	23.6
P3	17.1	16.8	18.9	7.6	0	0	31.6	6.6	0
P4	29.5	28.1	32.8	7.8	4.2	3.2	36.2	24.6	28.9
Mean ± Standard Deviation Study Eyes (N=4)	21.5±5.5	20.2±5.5	24.1±6.1	5.4±3.5	1.7±1.9	3.2±2.3	32.8±2.4	14.8±10.5	23.0±16.7
Mean ± Standard Deviation Normative Data (N=20)	31.4±3.3	30.4±3.1	32.8±4.8	20.0±4.3	18.5±4.7	24.5±4.4	29.0±1.9	32.9±2.1	34.4±2.3
Welch's Unpaired T Test									
P-value	0.0401	0.0369	0.0744	0.0007	<0.0001	<0.0001	0.0584	0.0414	0.2663
Mean Difference	-9.9	-10.2	-8.7	-14.6	-16.8	-21.3	3.8	-18.1	-11.4
95% Confidence Interval	(-19.0 to -0.8)	(-19.2 to -1.2)	(-19.0 to 1.6)	(-19.7 to -9.5)	(-19.9 to -13.7)	(-24.8 to -17.8)	(-0.3 to 7.9)	(-34.9 to -1.3)	(-38.0 to 15.2)

	Outer Nuclear Layer			Inner Retina			Total Retina		
	Outer Ring	Inner Ring	Central Subfield	Outer Ring	Inner Ring	Central Subfield	Outer Ring	Inner Ring	Central Subfield
P1	68.3	64	96.8	140.9	162.6	81.8	268.5	275.1	248.7
P2	36.2	54.7	75.7	132.5	128.9	62.8	195.3	215.3	192.9
P3	58.4	28.8	48.2	106.8	140.6	86.2	220.3	213.4	182
P4	69.1	54.8	83.8	122.9	133.9	69.2	264.4	242.1	217.9
Mean ± Standard Deviation Study Eyes (N=4)	58.0±15.3	50.6±15.2	76.1±20.5	125.8±14.6	141.5±14.9	75.0±10.9	237.1±35.4	236.5±28.9	210.4±29.6
Mean ± Standard Deviation Normative Data (N=20)	88.7±5.4	103.2±6.3	111.4 ±11.5	141.9±10.4	159.6±8.6	67.0±12.1	310.9±12.8	344.6±13.5	270.0±19.3
Welch's Unpaired T Test									
P-value	0.0287	0.0065	0.0444	0.1264	0.1001	0.2589	0.026	0.0053	0.0306
Mean Difference	-30.7	-52.6	-35.3	-16.1	-18.1	8	-73.8	-108.1	-59.6
95% Confidence Interval	(-55.3 to -6.1)	(-77.2 to -28.0)	(-68.9 to -1.7)	(-40.5 to 8.3)	(-42.6 to 6.4)	(-8.9 to 24.9)	(-130.9 to -16.7)	(-155.1 to -61.1)	(-108.7 to -10.5)

14.3.2. Individual characterizations in relation to normative data and longitudinal assessment of P3 and P4

The comparison further assessed whether the means for each eye individually fell within or exceeded the standard deviations (SD) from the mean values observed in the normative data.

P1 The spectral-domain optical coherence tomography (SD-OCT) analysis indicated preserved foveal center with thinning observed in the retinal pigment epithelium (RPE), outer segment (OS), outer nuclear layer (ONL), and total retina within the inner and outer ETDRS rings (Table 2, Figure 7 P1) compared to our reference database.

P2 SD-OCT analysis revealed preserved yet thinned foveal architecture, accompanied by outer segment atrophy in the peripheral macula, corresponding to the inner and outer rings (Table 2, Figure 7 P2).

P3 SD-OCT imaging revealed atrophy with a reduced mean thickness especially of outer retinal sublayers (Table 2, Figure 7 P3). A re-evaluation after 24 months showed further changes in mean thicknesses of retinal sublayers (Table 3).

P4 SD-OCT showed preserved RPE but thinning of the outer segments and ONL (Table 2, Figure 7 P4). A re-evaluation after 24 months showed a decrease in certain sublayers (Table 3).

Adapted from Schließleder et al. (1) with authorization from the copyright holders BMJ Publishing Group Ltd (2).

Table 3: Longitudinal data of retinal sublayers in P3 and P4

The mean retinal thickness (in µm) for individual layers is presented for the outer ring, inner ring, and central subfield of the ETDRS grid at the time of the first visit and after 24 months. Patient P3 exhibited a decrease, as well as thickening in certain regions, indicating measurement fluctuations. In P4, after 2 years, there were notable reductions in total retinal thickness, retinal pigment epithelium, and the outer nuclear layer.

Adapted from Schließleder et al. (1) with authorization from the copyright holders BMJ Publishing Group Ltd (2).

	Retinal Pigment Epithelium			**Outer Segments**			**Inner Segments**		
	Outer Ring	Inner Ring	Central Subfield	Outer Ring	Inner Ring	Central Subfield	Outer Ring	Inner Ring	Central Subfield
P3: First Visit	17.1	16.8	18.9	7.6	0.0	0.0	31.6	6.6	0.0
P3: 24 Months Later	17.8	13.4	11.5	8.5	0.2	0.5	24.9	0.7	0.0
Difference	0.7	-3.4	-7.4	0.9	0.2	0.5	-6.7	-5.9	0.0
P4: First Visit	29.5	28.1	32.8	7.8	4.2	3.2	36.2	24.6	28.9
P4: 24 Months Later	17.2	17.8	19.9	7.8	4.0	3.0	36.7	22.3	29.6
Difference	-12.3	-10.3	-12.9	0.0	-0.2	-0.2	0.5	-2.3	0.7

	Outer Nuclear Layer			Inner Retina			Total Retina		
	Outer Ring	Inner Ring	Central Subfield	Outer Ring	Inner Ring	Central Subfield	Outer Ring	Inner Ring	Central Subfield
P3: First Visit	58.4	28.8	48.2	106.8	140.6	86.2	220.3	213.4	182.0
P3: 24 Months Later	56.2	35.7	38.5	110.3	149.1	100.6	222.0	214.2	183.1
Difference	-2.2	6.9	-9.7	3.5	8.5	14.4	1.7	0.8	1.1
P4: First Visit	69.1	54.8	83.8	122.9	133.9	69.2	264.4	242.1	217.9
P4: 24 Months Later	63.5	48.5	62.8	121.0	132.2	68.5	250.0	228.1	198.8
Difference	-5.6	-6.3	-21.0	-1.9	-1.7	-0.7	-14.4	-14.0	-19.1

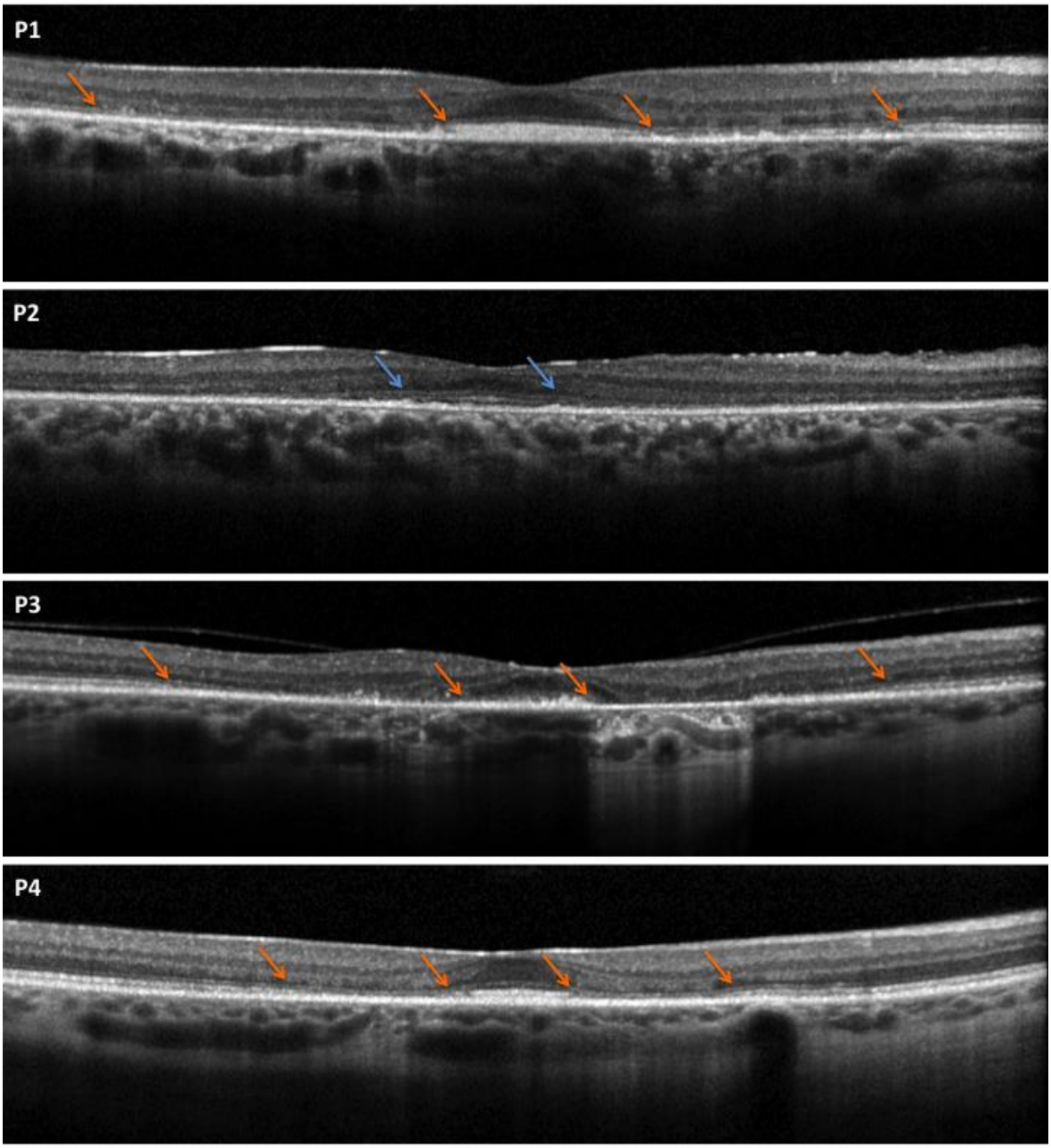

Figure 7 Exemplary unannotated SD-OCT B-scans through the fovea of all four patients (P1 to P4) from the first visit are displayed.

Patients with the autosomal dominant PROM1(NM_006017.3):c.1117C>T (p.Arg373Cys) mutation (P1, P3, P4) all showed reduced thicknesses of the outer retinal layers in the parafoveal region (orange arrows). In P2 with autosomal recessive disease PROM1(NM_006017.3):c.1354dup (p.Tyr452LeufsTer13); PROM1(NM_006017.3):c.630_c.630+8delGGTAAAAACinsAACTT- GAATGAAA, the retinal layers at the foveal center were thinned, but present (between blue arrows), and there was atrophy of the outer retinal layers at the peripheral macula (outside blue arrows).

Adapted from Schließleder et al. (1) with authorization from the copyright holders BMJ Publishing Group Ltd (2).

14.4. Findings in AOSLO imaging of the photoreceptor mosaic

14.4.1. Individual characterizations, including longitudinal assessment of P3 and P4

P1 Although full resolution and reliable quantification of cones within the foveal center were not achievable in adaptive optics scanning light ophthalmoscopy (AOSLO) imaging, cone counts were successfully performed at one degree, two degrees, and five degrees away from the foveal center (Table 4 and Figure 8). Split-detection imaging allowed for identification and counting of remaining photoreceptors. In confocal AOSLO images, a distinctive bull's eye maculopathy (BEM) pattern was observed, characterized by the absence of wave-guiding cones (Figure 9).

P2 Peak cone density was determined as 32505 ± 517 cells/mm², with feasible cone counts in the temporal, inferior, and nasal meridians (Table 4).

P3 AOSLO imaging at the foveal center revealed a peak cone density of 34135 ± 755 cells/mm². Subsequent AOSLO imaging indicated a decline in peak cone density to 32408 ± 275 cells/mm² after two years, which exceeded the standard deviation.

P4 PCD determination was not possible, but peripheral cone counts were conducted (Table 4). AOSLO imaging after 24 months showed a decrease in the number of cones at all analyzed areas, surpassing the standard deviation (Table 4).

Adapted from Schließleder et al. (1) with authorization from the copyright holders BMJ Publishing Group Ltd (2).

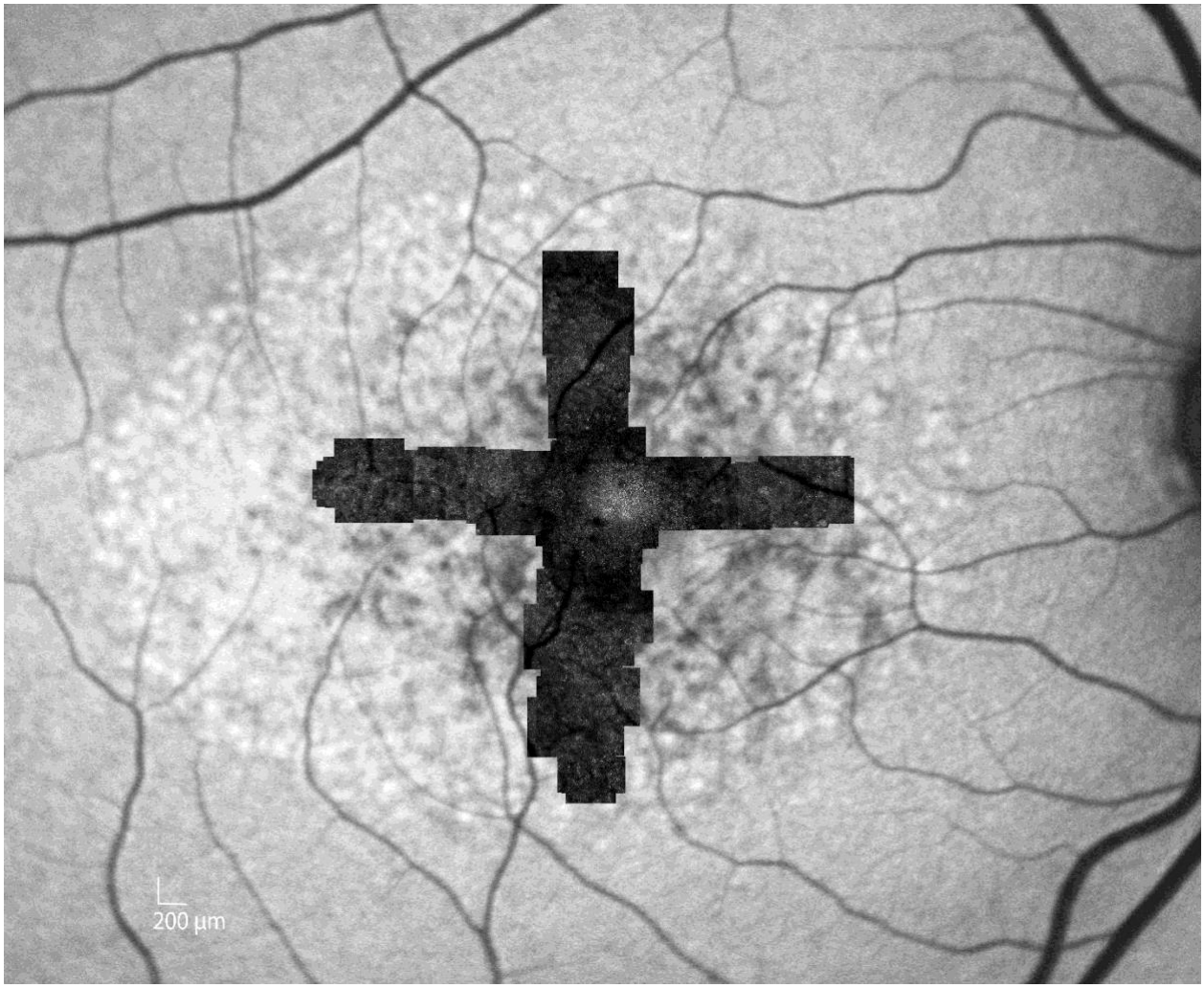

Figure 8 AOSLO mosaic

AOSLO confocal images overlayed on the FAF image of the right eye of P1 indicating the extent of photoreceptor imaging performed across the four directions away from the fovea.

Adapted from Schließleder et al. (1) with authorization from the copyright holders BMJ Publishing Group Ltd (2).

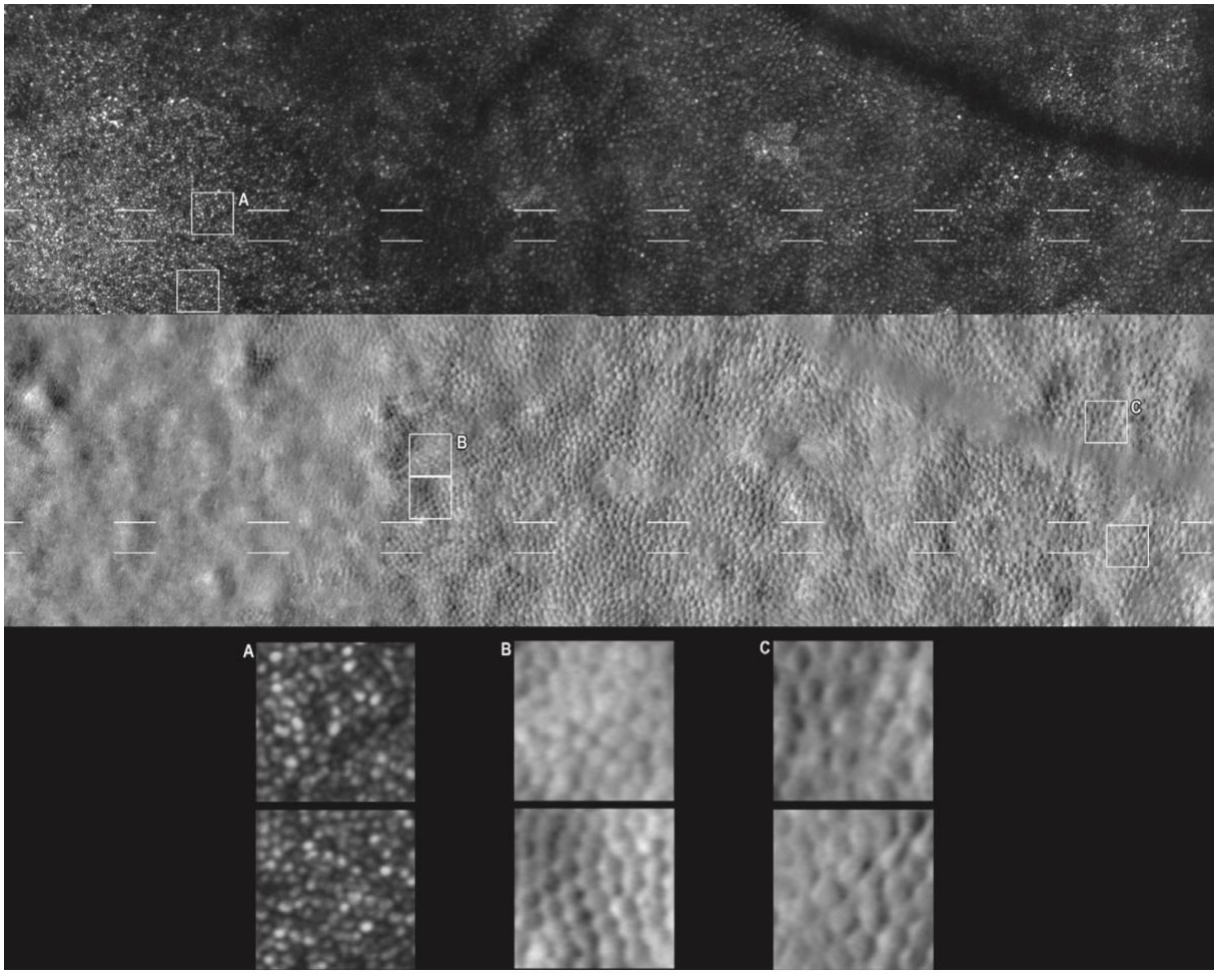

Figure 9 AOSLO cone counts in P1

Increased magnification of the nasal strip of P1's cone mosaic. (Top row) and non-confocal split-detection AOSLO (middle row) were used to generate photoreceptor mosaics of the right eye of patient P1, displaying outer and inner segments. The bottom row features magnified sections (55 µm2) marked as A in the confocal image and B, C in the split-detection image, representing locations 1°, 2°, and 5° away from the foveal center, respectively. These areas were utilized for cell annotations. Dashed white lines mark the position of the transfoveal SD-OCT B-scan depicted in figure 7 P1.

Adapted from Schließleder et al. (1) with authorization from the copyright holders BMJ Publishing Group Ltd (2).

Table 4 Mean cone densities

Mean (± Standard deviation, SD) peak cone density and mean (± SD) cone densities (cones/mm²) for distinct regions of interest (ROIs) 1°, 2°, and 5° away from the foveal center are provided, derived from adaptive optics scanning light ophthalmoscope imaging for P1, P2, P3, and P4. n/a = not applicable. Adapted from Schließleder et al. (1) with authorization from the copyright holders BMJ Publishing Group Ltd (2).

Patient ID		PCD	Inferior			Temporal		
			1°	2°	5°	1°	2°	5°
P1	Cone density	n/a	14656 (±2189)	10413 (±1081)	5674 (±1651)	14105 (±973)	9972 (±921)	n/a
	ROI	0	287.5	575	1437.5	287.5	575	n/a
P2	Cone density	32505 (±517)	14270 (±1095)	9862 (±325)	n/a	14050 (±953)	9862 (±737)	n/a
	ROI	0	314.9	629.8	n/a	314.9	629.8	n/a
P3 First Visit	Cone Density	34135 (±755)	n/a	n/a	n/a	n/a	n/a	n/a
	ROI	0	n/a	n/a	n/a	n/a	n/a	n/a
P3 Two Years Later	Cone Density	32408 (±275)	n/a	n/a	n/a	n/a	n/a	n/a
	ROI	0	n/a	n/a	n/a	n/a	n/a	n/a
P4 First visit	Cone density	n/a	23030 (±1877)	n/a	4683 (±249)	n/a	n/a	4628 (±467)
	ROI	0	281.8	n/a	1409	n/a	n/a	n/a
P4 Two years later	Cone Density	n/a	19091 (±1249)	n/a	4353 (±487)	n/a	n/a	n/a
	ROI	0	281.8	n/a	1409	n/a	n/a	n/a

Patient ID		Superior			Nasal		
		1°	2°	5°	1°	2°	5°
P1	Cone density	11515 (±2157)	8705 (±995)	7879 (±1393)	14711 (±856)	10853 (±793)	9696 (±615)
	ROI	287.5	575	1437.5	287.5	575	1437.5
P2	Cone density	10849 (±487)	n/a	n/a	13775 (±1283)	10413 (±1696)	n/a
	ROI	314.9	n/a	n/a	314.9	629.8	n/a
P3 First Visit	Cone Density	n/a	n/a	n/a	n/a	n/a	n/a
	ROI	n/a	n/a	n/a	n/a	n/a	n/a
P3 Two Years Later	Cone Density	n/a	n/a	n/a	n/a	n/a	n/a
	ROI	n/a	n/a	n/a	n/a	n/a	n/a
P4 First visit	Cone density	21872 (±1032)	n/a	5950 (±467)	18457 (±1816)	13939 (±569)	5839 (±827)
	ROI	281.8	n/a	1409	281.8	563.6	1409
P4 Two years later	Cone Density	16088 (±1177)	n/a	5509 (±271)	17356 (±1383)	12287 (±569)	5344 (±605)
	ROI	281.8	n/a	1409	281.8	563.6	1409

14.5. Summary of findings

Demographic Characteristics and Visual Acuity					FAF	OCT		AOSLO				
	Age	Mutation	Inheritance	BCVA (Right Eye)		OS Central Subfield	IS Central Subfield	PCD	1° INF	1° TEM	1° SUP	1° NAS
P1	45	PROM1 c.1117C>T p.(Arg373Cys)	AD	ETDRS score of 88 letters	Heterogeneous region: 20.83 ± 0.16	4	39.4	n/a	14656 (±2189)	14105 (±973	11515 (±2157)	14711 (±856)
P2	31	PROM1(NM_006017.3):c.1354dup (p.Tyr452LeufsTer13) PROM1(NM_006017.3):c.630_c.630+8delGGTAAAAACinsAACTT-GAATGAAA	AR	ETDRS score of 55 letters	DDAF measuring 0.49 ± 0.01 mm2, QDAF and additional QDAF spots with a combined area of 0.21 ± 0.02 mm2	5.4	23.6	32505 (±517)	14270 (±1095)	14050 (±953)	10849 (±487)	13775 (±1283)
P3	54	PROM1 c.1117C>T p.(Arg373Cys)	AD	ETDRS score of 35 letters	DDAF lesion measuring 1.45 ± 0.02 mm2, DDAF and QDAF of 8.82 ± 0.22 mm2	0	0	34135 (±755)	n/a	n/a	n/a	n/a
P4	31	PROM1 c.1117C>T p.(Arg373Cys)	AD	ETDRS score of 80 letters	No DDAF or QDAF lesions, faint dot-like discrete hyperautofluorescence	3.2	28.9	n/a	23030 (±1877)	n/a	21872 (±1032)	18457 (±1816)
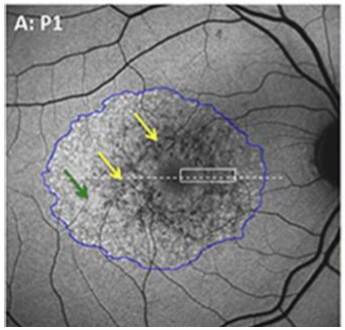					**Mean ± SD Study Eyes (N=4)**	**3.2±2.3**	**23.0±16.7**	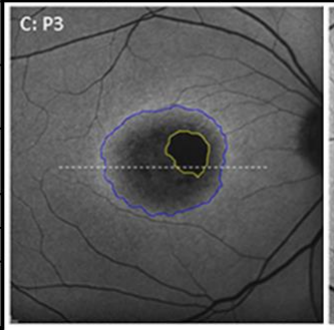				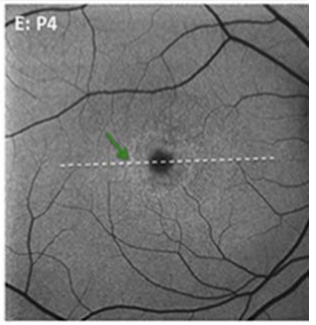
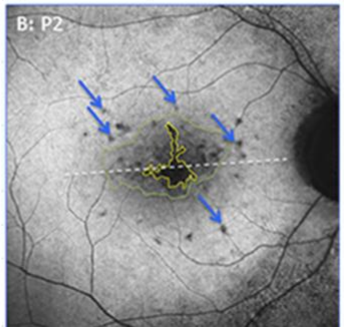					**Mean ± SD Normative Data (N=20)**	24.5±4.4	34.4±2.3					
					Welch's Unpaired T Test							
					P-value	<0.0001	0.2663					
					Mean Difference	-21.3	-11.4					
					95% Confidence Interval	(-24.8 to -17.8)	(-38.0 to 15.2)					

Figure 10 Summary of findings

A comprehensive overview of the study subjects characteristics and ocular measurements in the right eye at the baseline visit is provided, including age, genetic mutations, inheritance patterns, best corrected visual acuity (BCVA) in Early Treatment Diabetic Retinopathy Study (ETDRS) letters, fundus autofluorescence (FAF) measurements of atrophies in mm², spectral-domain optical coherence tomography (SD-OCT) measurements of the outer (OS) and inner segment (IS) in the area of central subfield in µm, along with a comparison to a normative database, peak cone densities (PCD) in mm², as well as cone densities from respective measurement angles at 1° inferior (INF), 1° temporal (TEM), 1° superior (SUP) and 1° nasal (NAS) as determined by adaptive optics scanning light ophthalmoscopy (AOSLO). FAF: All study eyes displayed patterns of altered autofluorescence in the macular region. Eyes with definite decreased autofluorescence (DDAF) and questionably decreased autofluorescence (QDAF) lesions (P3 and P4) exhibited corresponding reductions in visual acuity. P2, with the autosomal recessive (AR) form, developed a DDAF lesion at the age of 31, in contrast to P4, who carried an AD variant and was the same age but still maintained decent visual acuity, albeit with early hyperreflective dots. SD-OCT: The mean outer segment thickness in central subfield was significantly thinner compared to normative data, while mean inner segment thinning was not statistically significant. AOSLO: Cone counting was largely feasible, even with significant outer segment thinning as observed in the SD-OCT analysis. In areas of extensive atrophy, as indicated by the size of DDAF on FAF in P3, cone counts were not feasible. Marking of imaging according to the description of Figure 4. n/a = not applicable

Adapted from Schließleder et al. (1) with authorization from the copyright holders BMJ Publishing Group Ltd (2).

15. Discussion

High-resolution retinal imaging offers potential surrogate outcome measures for degenerative retinal diseases and may be accepted by regulatory authorities for therapeutic trials (148). However, the optimal modalities for consecutive imaging and tracking of disease progression are still being investigated. In the ProgStar-4 study, fundus autofluorescence (FAF) was selected as the primary endpoint, consistent with other studies on retinal degenerations (137, 138, 149). In our patients, particularly those with the autosomal-dominant *PROM1*(NM_006017.3):c.1117C>T (p.Ar- g373Cys) variant, the earliest signs observed were hyperautofluorescent patterns at the macula, followed by subsequent atrophy development. A previous report speculated that this hyperautofluorescence might be caused by a window defect representing autofluorescence from the retinal pigment epithelium (RPE) through an atrophic outer retina (67). However, previous studies on *PROM1*-transgenic mice revealed abnormal lipofuscin-like deposits in the RPE, indicating compromised function of this cell type (56). The role of PROM1 in regulating photoreceptor autophagy in RPE cells was also describe d (58). Quantitative autofluorescence (qAF) measurements recently demonstrated normal levels in a patient with dominant PROM1-related retinal dystrophy (PROM1-RD), whereas a patient with more severe autosomal recessive PROM1-RD (of similar age) exhibited significantly increased qAF levels (150). In an even more recent case series (151), qAF analysis incorporating short-wavelength autofluorescence (SW-AF) and near-infrared autofluorescence (NIR-AF) was performed on 36 eyes of 18 patients with genetically confirmed autosomal dominant PROM1-RD variants. The findings indicated that PROM1 maculopathy did not display elevated levels of SW-AF signal as measured by qAF, unlike in ABCA4-associated disease, which is known to show increased qAF levels (152). However, the aforementioned case series (151) on patients affected by PROM1-associated RD identified similarities in clinical findings between the two diseases, particularly in terms of macular atrophy. Studies in knockout-mice have shown that PROM1 is necessary for maintaining the expression levels of ABCA4 and RDH12, suggesting its involvement in the regulation of the visual cycle, particularly in the step of reducing all-trans-retinal to all-trans-retinol (68). There is also a possibility that PROM1 has an indirect effect on lipofuscin accumulation through ABCA4 dysfunction resulting from a disrupted outer segment structure (150). In advanced stages, such as in P3, FAF imaging can serve as a potential outcome measure for assessing atrophy development (148). However, the lack of any atrophic lesions, even when considering questionably decreased autofluorescence (QDAF) as depicted in Figure 4E and 4F, such as in the case of P4, may restrict the utility of this imaging modality (including qAF), particularly in

the initial stages of diseases where there is a potential for rescue of photoreceptors (and RPE) through pharmacological, gene augmentation, or gene editing therapies (134). Nonetheless, early intervention is crucial since significant photoreceptor loss occurs before the onset of visual symptoms (67). Patients in such early stages appear to be excellent candidates for adaptive optics scanning light ophthalmoscopy (AOSLO) imaging, as demonstrated in this study, which is, to the best of our knowledge, the first published series of AOSLO imaging in patients with PROM1-RD, encompassing both autosomal dominant and autosomal recessive traits. Three of these patients carried the previously reported AD PROM1(NM_006017.3):c.1117C>T (p.Ar- g373Cys) variant (63, 64), while one (P2) had a PROM1(NM_006017.3):c.1354dup (p.Tyr452LeufsTer13) variant inherited in an autosomal recessive fashion and a novel PROM1(N-M_006017.3):c.630_c.630+8delGGTAAAAACinsAACTT- GAATGAAA variant. The phenotypes of these patients, with P2 being one of the two youngest but exhibiting the largest area of outer segment layer thinning, as observed in the SD-OCT-based examination (Table 2, Figure 7 P2), confirm previous reports associating recessive diseases with early-onset severe panretinal degeneration (56, 69). This is further supported by our findings in P2, where AOSLO imaging of cones at multiple locations was feasible, despite significant thinning of the outer segment observed on SD-OCT. In contrast, the dominant PROM1(NM_006017.3):c.1117C>T (p.Ar- g373Cys) variant primarily causes macular degeneration, mainly affecting cone photoreceptors and exhibiting later-onset dystrophy primarily involving the macula (56, 64). Longitudinal follow-up imaging and analysis were possible in two of the autosomal dominant patients, revealing mild but significant progressive cone loss, exceeding the standard deviation. Even with significant outer segment thinning observed in our SD-OCT analysis, AOSLO imaging utilizing the split-detector technique (131) provided a reliable method to visualize the inner segment structure of cones in all cases except for P3, who displayed a pronounced central DDAF area. Therefore, individuals affected by PROM1-RD are suitable candidates for AOSLO imaging, as is the case with other retinal degenerations where the loss of outer segments precedes the degeneration of the remaining photoreceptor cell (130, 131). Our quantitative analysis of SD-OCT supports the concept of outer segment degeneration, although thinning of the outer nuclear layer (ONL) throughout the macula was also observed in all cases, consistent with a previously reported case (67). However, while Pajewala et al. did not report any changes in OCT imaging over a three-year period, we were able to demonstrate a decrease in the mean retinal thickness of affected layers in SD-OCT images over two years in P4 through semi-automated segmentation.

15.1. Limitations

Since the number of analyzable AO-montages was small, only limited statistical evaluations were possible. The small number of study patients resulted from the extreme rarity of the disease itself. In orphan diseases small sample sizes are inevitable, especially when the primary end point is also uncommon (153).

The patients recruited for our study were selected from an IRD (inherited retinal disease) database at Moorfields Eye Hospital. The database contained information from 4,236 individuals belonging to 3,195 families as of December 2021. It involved pathogenic variants in 135 different genes, with the PROM1 gene being present in 1.2% of families (8); however, this percentage was even smaller when the study was initiated and enrollment began (17).

In the past, Sanger sequencing of single genes or small gene panels was commonly utilized as a cost-effective screening method for IRD, as for our patients P1,P3 and P4, carrying the AD PROM1(NM_006017.3):c.1117C>T (p.Ar-g373Cys) variant (17). This approach is especially suitable for patients whose genetic makeup closely correlated with the observed symptoms, known as genotype-to-phenotype correlation (154). However, various factors, including the patient's interest in testing, the likelihood of positive results, and potential eligibility for treatment trials, are taken into account when determining whether to proceed with genetic testing (17). In contrast, for cases involving patients displaying the typical characteristics of rod-cone dystrophy (retinitis pigmentosa), the disease-causing variants could be present in any of the 100+ different genes associated with this condition. Consequently, adopting a less targeted approach might be more advantageous in such scenarios (154).

Recent advancements in next-generation sequencing have significantly improved the accessibility of large gene panels for testing, leading to the identification of more patients and the discovery of new causative mutations. The retinal genetics service at Moorfields Hospital is dedicated to provide molecular diagnostic investigations to all patients suspected of having an inherited retinal disease (IRD). Thus the costs of genetic testing are typically covered by healthcare organizations such as the National Health Service (NHS) or the National Institute of Health Research (17). Genetic testing is performed for various types of retinal dystrophies, including retinitis pigmentosa, chorioretinal degenerations, macular dystrophies, cone and cone-rod dystrophies, stationary conditions, and suspected syndromic retinal dystrophies. While some patients may choose to decline genetic testing, the majority opt to undergo it. The testing strategy involves gene panel tests that encompass a wide range of genes known to be associated with retinal dystrophies. Depending on the inheritance pattern, specific gene panel

tests or single-gene testing can be requested. In cases where gene panels yield negative results but a monogenic disorder is still suspected, further sequencing is pursued, including whole-exome sequencing or whole-genome sequencing. Although whole-genome sequencing provides a comprehensive alternative for patients with undiagnosed conditions, its current implementation is limited due to cost and efficiency concerns. As a result, targeted genome re-sequencing is often preferred. Even whole-exome sequencing is insufficient to detect all variants, particularly complex structural changes such as large deletions, inversions, translocations, and trinucleotide repeat expansions. Moreover, variants in deep intronic or regulatory regions cannot be captured using this sequencing approach. There is a confident expectation that in the near future, a precise molecular diagnosis will be available for the majority of patients (16). Whole-genome sequencing is increasingly funded through national research projects such as the National Institute of Health Research Bioresource project and the 100,000 Genomes project. Remarkably, approximately 600 individuals in the Moorfields IRD database (17) have already received a molecular diagnosis through whole-genome sequencing.

Also recording-related difficulties had led to the fact that from the already small number of six study subjects, only two montages could be repeated in analyzable quality and comparison was possible at few of the intended measuring points. Hereby the major common limitation was poor fixation, in alignment with one of the largest AO ophthalmoscopy studies to date (n=51) (155). In another study, out of 51 subjects with grades I to IV retinas of CNGB3-Associated Achromatopsia, only 26 had images of sufficient quality to be processed, montaged, and quantified. Nystagmus and/or unstable fixation were the primary reasons the inability to process the remaining subjects (155). Eye-tracking systems integrated with AO systems (156-158) may allow more subjects to be imaged and improve data collection in the future. In addition, image processing and analysis are important bottlenecks that developments in machine learning, for example, will hopefully solve in the near future, thereby enabling wider application of AO technology (159).

The utilization of adaptive optics is currently confined to research purposes. To establish standard reference databases, it is essential to analyze significant numbers of healthy eyes. This approach enables the identification of any abnormalities or early-stage diseases by comparing deviations from the norm. The cone mosaic, particularly the outer photoreceptor segment, can be observed during these investigations. Nevertheless, there have been limited studies conducted on the density of cone packing and the spacing between cones in the cone

mosaic at the center of the retina Prior to clinical implementation, it is crucial to establish standardized norms for these measurements (160, 161).

Adaptive optics facilitates the imaging of cones, primarily due to their ability to guide waves. They appear as an imperfect hexagonal pattern when observed. Various studies have utilized cone density and spacing as significant indicators (162).

Additionally, adaptive optics has made it possible to identify different subtypes of cones based on their sensitivity to different wavelengths, such as short, medium, and long wavelengths (163). Dysflective cones, which exhibit altered functionality, can be detected through adaptive optics by observing changes in the reflectance of their outer segment tips (COST) (164). Conversely, rods, which are smaller in size and have limited wave-guiding properties, have been the subject of fewer imaging studies. Nevertheless, visualizing rods could provide valuable guidance for devising treatment approaches for inherited retinal dystrophies (165).

Besides cones and rods, the exploration of other retinal layers using AO has been documented in the literature:

- Retinal pigment epithelium

The imaging of the retinal pigment epithelium (RPE) using adaptive optics has posed difficulties due to the integration of photoreceptor outer segments within the RPE layer. However, these challenges have been surmounted by imaging the RPE in regions where there is either loss of photoreceptors or the presence of subretinal fluid (166). Morgan et al. achieved successful imaging of the RPE mosaic in a healthy retina using a dual-channel fluorescence adaptive optics scanning light ophthalmoscope (AO SLO) (167). Visualizing the RPE and determining the ratio between RPE and photoreceptor can facilitate the monitoring of various retinochoroidal pathologies and evaluate the effectiveness of treatments (167).

- Ganglion cells

Imaging ganglion cells has posed challenges due to their transparent characteristics and densely packed three-dimensional structures. Rossi et al. successfully generated two-dimensional images of retinal ganglion cells using a multi-offset adaptive optics scanning light ophthalmoscope (AO-SLO). Through the application of adaptive optics, it is also possible to distinguish between various subtypes of ganglion cells, including parasol and midget cells, based on distinctive imaging features (168, 169).

- Lamina cribrosa

Through the utilization of adaptive optics, the lamina cribrosa can now be visualized and measured, including parameters like pore size, shape, and density. These measurements have exhibited reliable repeatability. By precisely quantifying and standardizing these parameters and establishing correlations with predisposing genes, it may be feasible to screen and identify individuals who are susceptible to specific conditions at an exceptionally early stage (170).

- Retinal vasculature

Adaptive optics enables precise visualization and measurement of the retinal microvasculature by employing various parameters, including wall thickness (WT), lumen diameter (LD), wall-to-lumen ratio, and cross-sectional area of the vessel wall (171). Furthermore, it is feasible to observe the movement and velocity of leukocytes in the perifoveal capillaries. These parameters hold particular importance for patients with retinal vascular diseases like diabetic retinopathy and hypertensive retinopathy (172).

In addition to mentioned above, other applications of AO include conditions such as albinism (173), age-related macular degeneration (174, 175), autoimmune retinopathy (176), as well as basic and applied research to provide insights into the neurophysiology of the visual system (177).

Evolving AO-guided retinal sensitivity tests ('nanoperimerty') may improve the ability to correlate cellular imaging and functional testing with fine retinotopic accuracy (178-180).

As AOSLO units remains costly and scarce, commercially accessible alternatives like the Heidelberg Engineering SPECTRALIS High Magnification Module (HMM) have evolved in recent years (181). These findings might add to our comprehension of the photoreceptor mosaic in bigger populations. The Heidelberg SPECTRALIS confocal scanning laser ophthalmoscopy equipment is used to obtain near-infrared reflectance retinal pictures with HMM (including Heidelberg HRA SPECTRALIS hardware and Heidelberg Eye Explorer 1.10.4.0 software). Participants may be scanned with their pupils undilated, which, according to authors, might increase the recording quality in some individuals (181).

Despite supposed advantages of HHM over AOSLO, such as ease of recording, integrability into existing OCT systems which increases clinical accessibility, claimed success rates for HMM imaging vary widely. Success rates range reportedly from 45% to 80% (181-183).

In one work, 30 participants' cone mosaic metrics produced from adaptive optics scanning light ophthalmoscopy (AOSLO) photographs were compared to those gained using Heidelberg

Engineering SPECTRALIS High Magnification Module (HMM) (181). The intergrader intraclass correlation coefficients for cone measures were high in both groups (0.688–0.757 for HMM; 0.805–0.836 for AOSLO). Estimates of cone density produced from HMM pictures were on average 2,661 cones/mm² (24.1%) lower than estimates derived from AOSLO. Hence, HMM estimates of cone spacing were greater than AOSLO estimations on average (181).

Regarding our autofluorescence imaging, we tried to build on grading methods established in previous studies, which made it possible to size existing atrophies, a necessary information to be able to describe the phenotype (136-138).

Nonetheless, our autofluorescence configuration was custom-designed to target short-wavelength autofluorescence (SW-AF) following the methodology of previously conducted research (136-138). The rationale behind this choice – and not to use qAF which requires bleaching of the photopigments prior to image acquisition - lies in the potential hazard of light toxicity, especially in ABCA4-related diseases that origine from the accumulation of A2-dihydropyridine-ethanolamine, a significant constituent of lipofuscin. This buildup has the potential to expedite the progression of the disease (184).

Furthermore, it is important to acknowledge that even the analysis of qAF fundus images is not the definitive measure, as it solely focuses on a small area of the posterior pole. The internal software of the device uses a specific pattern of 25 segments, composed of three concentric rings centered on the fovea, with the outermost ring extending to the optic disc's edge (115). The placement of this pattern relies solely on the examiner's visual judgment of where the fovea and optic disc are presumed to be located. Previous studies (114-118) also presented the average QAF8 signal, which represents the average pixel intensities of the middle ring located at the perifovea, comprising eight equally spaced segments (115). These average QAF8 values have been employed to construct normative databases for healthy individuals (115) and to categorize QAF intensities in diseased eyes, especially in cases of AMD (116, 185). However, in the context of AMD or IRD eyes, analyzing the mean QAF8 value becomes challenging because autofluorescence signals from small pathological areas (e.g., drusen or tiny atrophic regions) disappear if these affected areas cover only a few pixels. These limited pixels may not significantly influence the overall mean QAF8 signal within a segment or the entire original QAF grid. Additionally, to effectively describe both physiological and pathological observations, there is a need for tools that facilitate direct comparisons of QAF images with other retinal imaging methods. Different imaging modalities highlight various retinal structures and could complement and enhance the advantages of multimodal imaging. Kleefeldt et al. (186) are dedicated to address these issues by employing multimodal retinal

imaging, coregistration based on SD-OCT, and image alignment to generate image stacks. This study also establishes standard normative QAF retinas for healthy adults in various age groups and introduces advanced tools for analyzing QAF images, laying the groundwork for the assessment of diseased macula and retina (186).

A case series (151) demonstrated NIR-AF signals similar to those observed in healthy eyes in individuals with autosomal dominant PROM1-related macular degenerations.

Beyond that, approaches finding fundus autofluorescence classifications for Inherited Retinal Diseases using deep learning algorithms have been published recently (187). In the study by Miere et al. (187), FAF images from individuals with conditions such as retinitis pigmentosa (RP), Best disease (BD), Stargardt disease type 1 (STGD1), and a comparable healthy group were utilized to train a multilayer deep convolutional neural network (CNN). This network was trained to differentiate FAF images specific to each type of IRD from those of normal FAF. The CNN was trained and validated using a dataset comprising 389 FAF images. The global accuracy of these IRD classifiers reached 0.95. Furthermore, the precision-recall area under the curve (PRC-AUC) averaged 0.988 for BD, 0.999 for RP, 0.996 for STGD, and 0.989 for healthy controls. Despite these promising outcomes, it's worth noting that the limited dataset prevented further classification based on the disease stage. Considering that IRDs are rare diseases, the availability of extensive datasets would only be feasible through collaborative efforts across multiple institutions (187).

Another FAF-related determinable parameter would have been FLIO (Fluorescence Lifetime Imaging Ophthalmoscopy), a measure for time delay from excitation to emission and the decay curve of emission intensity. It is not necessarily related to fluorescent intensity (188). Every fluorophore has a distinct excitation and emission spectrum, as well as a fluorescence lifetime (189). The period between excitation and emission may be determined either directly or indirectly by adjusting flickering light while monitoring the phase delay of emission. In healthy eyes, AF lifetimes increase with age (190) and distance from the fovea (191) presumably due to macular pigment distributions. In general, diseased retina and RPE exhibit a large increase in lifespan, which is often attributable to the accumulation of LF with its relatively long lifetime (189). Disease-specific alterations have been seen in AMD (192), macular telangectasia type 2 (MacTel) (193), Stargardt disease type 1 (STGD1) (194), hydroxychloroquine retinopathy (195) and choroideremia (196). Although clinical value is limited at now, the outcomes of these research are promising for monitoring disease progression in observational and therapeutic trials (197).

Concerning the semi-automated OCT segmentation, our experience was, that it is an extremely laborious process. The automatic pre-segmentation of our custom software has only worked reasonably well in the healthy layers. Due to the disorganization of the outer retina, it is very challenging to accurately segment the relevant boundaries and categorize tissues into the appropriate layers. This can lead to large variability in the difference between gradings depending on the layer (84, 198). Deep-learning algorithms may provide a more robust automated segmentation in the future although the underlying pathophysiology may limit the applicability of SD-OCT in certain cases (198). However the advancement of deep learning-based OCT models has encountered a few hurdles throughout its development. Fang et al. (199) introduced a CNN and graph search-based method, but it has a high computational burden and is sensitive to boundary positions. Other discussed approaches include ReLayNet (200), a fully convolutional neural network (201), FCNs with Gaussian process regression (202), a cascaded FCN framework (203), a Bayesian deep learning approach (204), a CNN-based framework (205), specific retinal layer segmentation (206), a convolutional neural network approach (207), and a method based on an encoder-decoder model (208). DeepRetina currently appears to be the most promising approach for retinal layer segmentation, with improvements in segmentation precision and sensitivity (209).

With regard to the statistical comparison of the mean retinal sublayers with the normative group, it should be noted that the OCT reports did not provide us with the standard deviation or the exact number of slices that contributed to the calculation of the outer ring, inner ring, and central subfield areas. Due to these circumstances, we included the mean thicknesses of the retinal sublayers of the four eyes as individual values in the calculation, as similar information was also absent from the normative group. We refrained from conducting a normal distribution test on the study group due to the limited sample size and the unavailability of comparable data for the normative group. Additionally, Moorfield Eye Hospital did not provide more detailed data about the normative group, such as average age, gender distribution, or other demographic information needed for assessing comparability. Only the information that the normative collective consisted of age- and gender-matched individuals without retinal pathologies, as described in the methods section, was accessible to me. Nevertheless, attempts were made with the available resources to represent significant differences.

Due to time constraints, we were unable to include the measurement of macular sensitivity using microperimetry in the dissertation, as originally planned, along with its correlations to AOSLO. Instead, visual acuity served as the sole functional parameter. Throughout the disease progression of macular degeneration, visual acuity has traditionally been the primary assessment method for macular function. However, it is important to acknowledge that visual

acuity only represents the physiological function of the central fovea and may not adequately evaluate the surrounding macular area at different stages of the disease process(132). To address these limitations, the technique of MP allows for repeated testing of the same sites within the macular area. Within the ProgStar studies (210-212), MP examinations have demonstrated their value in diagnosing Stargardt disease, as they can detect visual impairments before any abnormalities become visible in retinal images. Mesopic MP testing using the MP-1 device was conducted on 359 eyes of 200 Stargardt disease patients, with a follow-up period of one year. Disease progression was assessed by measuring the decline in retinal sensitivity (in dB), the increase in the number of deep scotoma points, and the decrease in the number of points with a minimum retinal sensitivity threshold. The tracking of points adjacent to scotomas over time revealed a faster rate of progression, indicating their potential as a clinical endpoint (211).

Fixation metrics were also investigated in a ProgStar study (213), where changes in the location of preferred retinal loci (PRL) and fixation areas were measured over a one-year period. However, heterogeneity in these changes was observed, potentially due to neuronal adaptations, the presence of multiple PRLs, and the need for longer follow-up. Therefore, fixation metrics may be more suitable as secondary endpoints, with a focus on specific subsets of patients (213).

The SMART study (214), an ancillary study conducted alongside ProgStar in ABCA4-associated diesease, specifically examines scotopic function using the MP-1S device. Data from 118 participants indicated that scotopic function deteriorated at a faster rate compared to mesopic function, suggesting that it may be a more sensitive endpoint for future trials. Furthermore, a previous study demonstrated a correlation between the loss of scotopic sensitivity and structural changes observed through OCT imaging (215).

The ProgStar-4 study investigates the natural history of PROM1-associated disease by incorporating both mesopic and scotopic microperimetry assessments (57).

15.2. Potential Therapies

15.2.1. Gene therapy

Following the pioneering approval of voretigene neparvovec by the Food and Drug Administration (FDA) for the treatment of RPE65-associated Leber's congenital amaurosis (LCA), there has been a vast amount of excitement about the potential of retinal gene therapy for various other monogenic IRDs (216). Despite the existence of numerous ongoing therapeutic studies for various other monogenic inherited retinal diseases (IRDs), there are currently no approved treatments available for PROM1-associated retinopathy, and to the best of our knowledge, there are no ongoing therapeutic studies specifically addressing this condition either. The development of potential treatments requires a sufficient understanding of the underlying mechanisms of PROM1-associated RD.

The pentaspan transmembrane domain glycoprotein encoded by PROM1 is specifically localized to membrane protrusions at the base of rod and cone outer segments, where its key roles include disc morphogenesis and subsequent photopigment sorting (56), with wild-type PROM1 preferentially localizing to basal disc membranes in rod OS and throughout outer rims of disc lamellae of cone OS (Figure 11) (64).

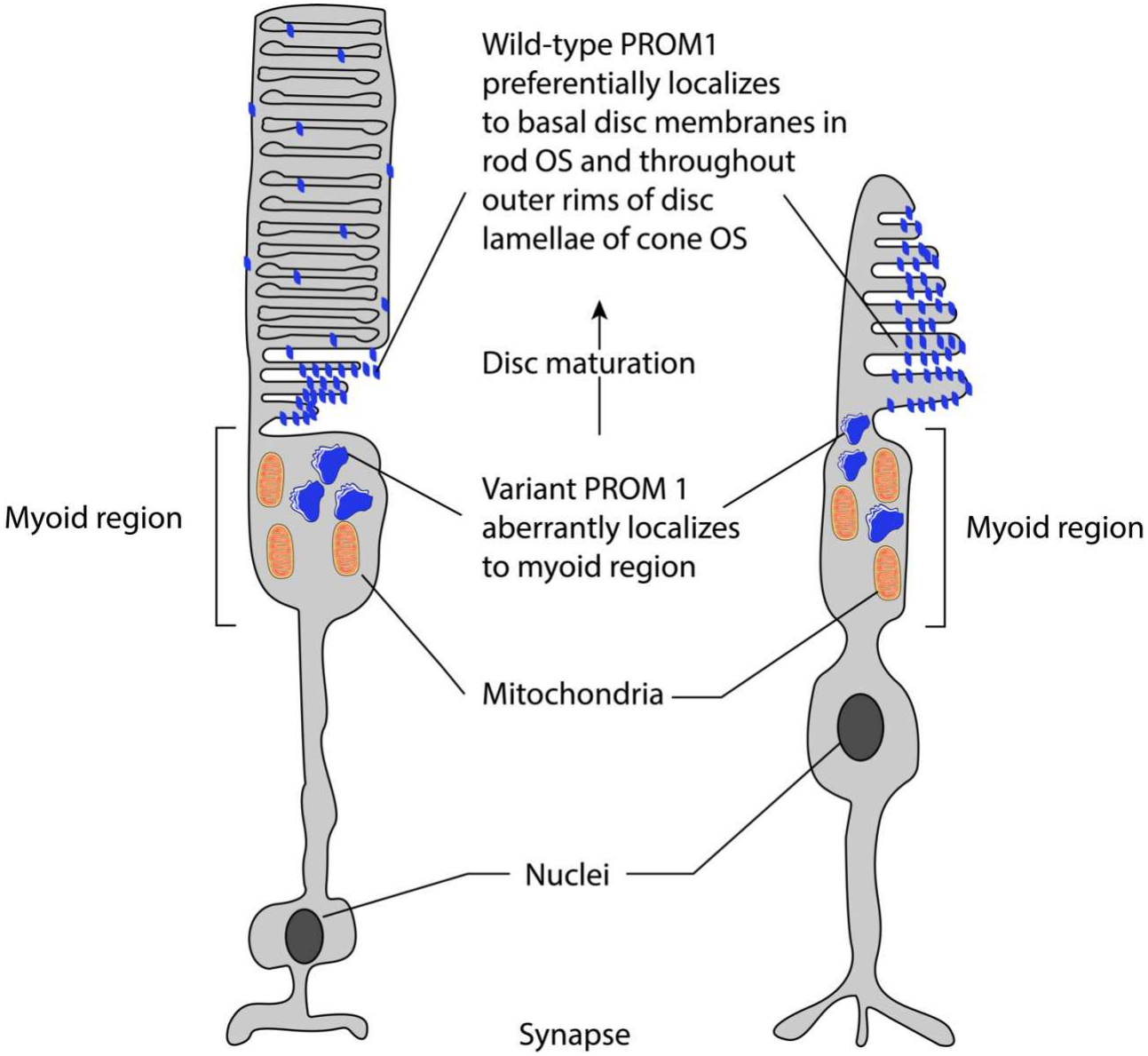

Figure 11 Rod and cone photoreceptors

Illustration of rod and cone photoreceptors, depicting localization of wild-type and variant PROM1; OS indicates outer segment.

Adapted from Cehajic-Kapetanovic et al. (64). This Figure is authorized under a Creative Commons Attribution 4.0 International License (3).

By 2019, 41 different mutations had been identified in the PROM1 gene, with 34 of them having a known mode of inheritance, as depicted in Figure 12. Among the 34 the majority was reported as autosomal recessive (11 nonsense variants, 9 frameshift variants, 8 splice site variants, and

3 missense variants), while just three were found to be autosomal dominant (all missense variants)(64).

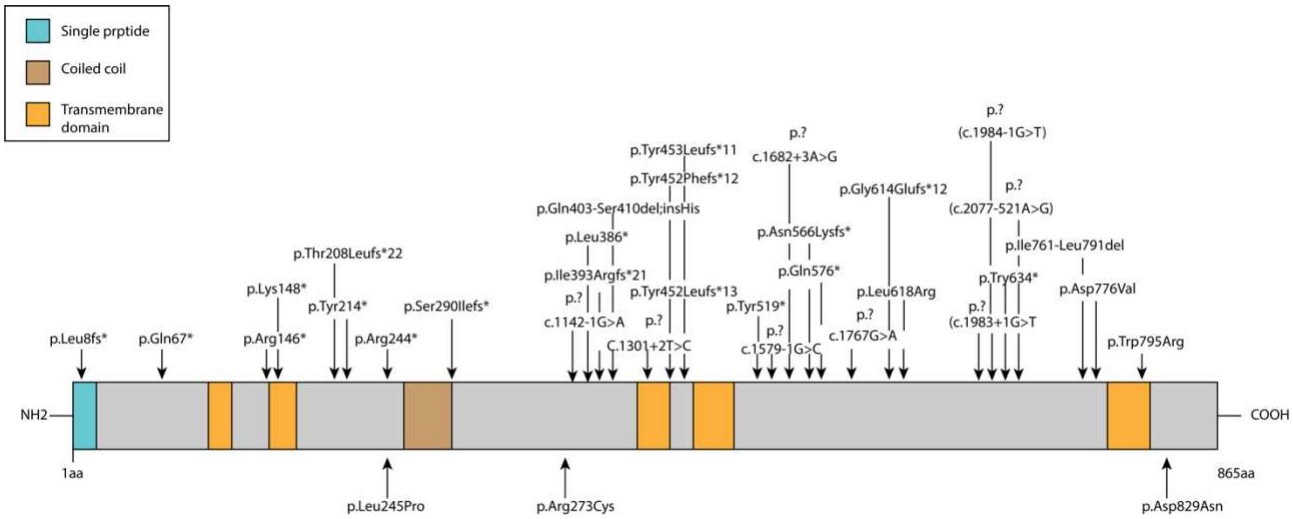

Figure 12 Schematic representation of PROM1 and associated variants

The PROM1 protein is represented as a grey bar, with the corresponding protein domains displayed in various colors. Recessive mutations are depicted above, while dominant mutations are shown below. The arrow marks the position of the first impacted amino acid in splice site and frameshift variants. Variants lacking a valid prediction on the protein (e.g., splice site) are indicated as p.? with their corresponding c. designations listed below.

Adapted from Cehajic-Kapetanovic et al. (64). This Figure is authorized under a Creative Commons Attribution 4.0 International License (3).

The severe homozygous recessive phenotype has been linked to null variants that eliminate the function of alleles, resulting in a lack of PROM1. The vast number of frameshift and nonsense variations led to a premature stop codon, resulting in a shortened modified RNA that is rapidly eliminated by nonsense-mediated decay prior to translation (52).

Furthermore, the missense and splice site variants associated with the recessive condition were likely associated with a null (or loss of function close to null) effect, as evidenced by the similar phenotypes of subjects with homozygous missense and splice site variants compared to equally aged patients with truncating mutations (64). These loss-of-function mutations were related with disrupted membranes of the optic disc and photoreceptor atrophy, as seen in mice lacking PROM1 (41).

Contrarily, the milder, dominant phenotype was linked with a dominantly negative missense variant impact. This seemed to lead in a stable variant protein linked with the variant protein's mislocalization (64).

To restore the missing protein and maybe rescue the phenotype, a genetic treatment strategy might be the subretinal introduction of an adeno-associated viral vector expressing the PROM1 (2.5 kilobase pairs) gene to photoreceptors at a preliminary phase of recessive dystrophy (64).

Nevertheless, as Cehajic et al. (64) emphasize, the dominant variation must be silenced first, for example, by RNA silencing through a mirtron (217), and then a gene replacement treatment of the wild-type protein, i.e. block-and-replace therapy, should follow. In severe cases of disorder in which permanent photoreceptor loss has occurred, optogenetic treatment (218) might be used to restore vision (64).

15.2.2. Visual cycle modulators

A previously mentioned study (68) conducted on PROM1 knockout mice provided evidence that the expression of genes related to the visual cycle was altered, potentially affecting the preservation of chromophore levels in photoreceptor outer segments. The knockout of PROM1 led to a significant decrease in the expression of ABCA4 and RDH5/12/14 genes. Interestingly, the expression of other genes such as rhodopsin, IRBP, LRAT, S-opsin, Rdh11, and Rdh13 remained largely unaffected or may have even been upregulated. This suggests that PROM1 plays a critical role in maintaining the expression levels of specific genes involved in the visual cycle, particularly during the reduction step from all-trans-retinal to all-trans-retinol.

Additionally, the study demonstrated that PROM1-knockout mice reared under normal light conditions exhibited severe degeneration of photoreceptor cells, whereas those reared in darkness retained a significant proportion of photoreceptor cells. This observation was consistent across both strains of mice. The researchers further investigated the ultrastructure of photoreceptor cells using transmission electron microscopy and found that the dark-reared PROM1-knockout mice preserved the cellular structure compared to those reared under light conditions. Immunohistochemistry analysis also indicated reduced mislocalization of rhodopsin and M-opsin in the dark-reared PROM1-knockout mice. To evaluate the functionality of photoreceptor cells, the researchers conducted electroretinography (ERG) on the PROM1-knockout mice. They discovered that the scotopic ERG responses, which reflected the physiological health of rod and cone photoreceptors, were impaired in the Prom1-knockout mice reared under normal light conditions. However, when the mice were raised in complete darkness, the scotopic ERG responses significantly improved, with the b-wave reaching almost the same level as that of the wild-type mice. Similar observations were made in photopic ERGs (68).

15.2.2.1. Fenretinide

The synthetic retinoid derivative Fenretinide reduces the availability of retinoids to the eye by its interaction with retinol binding proteins (RBP; RBP1-4; NCBI gene IDs 5947-5950) and thereby reduces accumulation of A2E in the RPE (219-221). The first discoveries were from adverse effects described in clinical studies using large dosages of fenretinide (600–800 mg/day) in individuals with basal cell carcinoma exhibiting considerable electroretinogram changes and decreased dark adaption (222). Subsequently, Decensi et al. observed that the daily dosage of 200 mg, which is now utilized in cancer chemoprevention studies, had relatively

little effects (223). Again, clinical findings indicated that fenretinide exhibited dose-dependent impairment of retinal function. In geographic atrophy, which is characterized by an excessive buildup of retinol-based toxins, fenretinide has been recommended as a therapy due to its ability to lower retinol levels in circulation (224). In contrast to other organs, the absorption of retinol by the eye is mostly reliant on delivery via the RBP complex, which may be regulated by fenretinide through the quick clearance of the complex in the urine. Two-hundred forty-six individuals with geographic atrophy were given 100 and 300 mg of fenretinide orally, daily, in a placebo-controlled, double-masked, two-year experiment. As hypothesized, fenretinide treatment generated a dose-dependent reversible decrease in serum RBP-retinol, with visual dysfunction and night blindness being the most prevalent side effects in individuals treated with larger doses. Importantly, restricting retinol uptake from the bloodstream into retinal pigment epithelium has been linked to a decline in lesion growth rates, continuing to support the potential of fenretinide in the management of retinopathy, according to the study in geographic atrophy patients (225). The prospective human use of Fenretinide hinges on the balance between the advantage (desired effect) of inhibiting the buildup of harmful lipofuscin (226) and the ocular adverse effects, such as rod malfunction (227, 228).

Dellet et al. (68) demonstrated that fenretinide delayed PROM1-mediated retinal degeneration and partially preserved retinal function in PROM1-knockout mice, as shown by the structural and functional improvements observed in the treated mice. They conducted experiments in which PROM1-knockout mice were intraperitoneally injected with fenretinide. The results showed that the mice treated with fenretinide had thicker photoreceptor segments, a thicker outer nuclear layer (ONL), and an increased number of photoreceptor nuclei compared to the control group. This indicated that fenretinide partially protected the photoreceptor cells from degeneration caused by PROM1 deficiency. Furthermore, the researchers assessed the effect of fenretinide on retinal function by analyzing scotopic electroretinography (ERG) responses. They found that fenretinide treatment decreased the a-wave amplitude in wild-type retinas. However, in the PROM1-knockout retinas, which were initially insensitive to the stimulus, the rod responses improved after fenretinide treatment. Similar improvements were observed in the b-wave responses. These findings suggested that fenretinide, despite its inhibitory effect on normal rod cell function, improved rod function in PROM1-knockout mice, potentially by reducing cell death (68).

15.3. Conclusion

This is the first study to investigate both autosomal recessive and autosomal dominant cases of PROM1-associated RD down to cellular level with adaptive optics scanning light ophthalmoscopy. Individuals with PROM1-RD are eligible for AOSLO imaging, along with other retinal dystrophies in which the outer segments of the photoreceptor cell are lost ahead of the rest of the cell (130, 131).

The evidence of residual cones in both autosomal dominant and recessive disease presents an opportunity for potential therapeutic intervention, for which the proof of principle has been shown in the knockout mouse model (68).

Furthermore, this work may pave the way for future treatments trials, regardless whether these are gene-dependant or not. While the numbers of patients with molecular-genetic diagnosis is increasing every day due to the aforementioned higher numbers of genetic testing in retina practice, the amount of patients with confirmed disease-causing variants in the PROM1 gene is also world-wide increasing. The results presented in this work may provide potential outcome measures, depending on the stage of disease, i.e. the amount of already present atrophy: AOSLO in early diseases, OCT in the midstage and FAF in advanced stages.

16. Appendix

ReferencesUncategorized References

1. Schließleder G, Kalitzeos A, Kasilian M, Singh N, Wang Z, Hu Z, et al. Deep phenotyping of PROM1-associated retinal degeneration. British Journal of Ophthalmology. 2023:bjo-2022-322036.
2. Copyright and authors' rights: BMJ Publishing Group Ltd; 2023 [Available from: https://authors.bmj.com/policies/copyright-and-authors-rights/.
3. CC BY 4.0 DEED: Creative Commons; 2019 [Available from: https://creativecommons.org/licenses/by/4.0/.
4. RIGHTS & PERMISSIONS: Association for Research in Vision and Ophthalmology; 2023 [Available from: https://arvojournals.org/ss/terms.aspx.
5. Rights and Permissions: Karger AG; 2023 [Available from: https://karger.com/pages/rights-and-permissions.
6. Nathans J, Thomas D, Hogness DS. Molecular genetics of human color vision: the genes encoding blue, green, and red pigments. Science. 1986;232(4747):193-202.
7. Haegerstrom-Portnoy G, Schneck ME, Brabyn JA. Seeing into old age: vision function beyond acuity. Optom Vis Sci. 1999;76(3):141-58.
8. Lamb TD. Why rods and cones? Eye (Lond). 2016;30(2):179-85.
9. Witkin AJ, Ko TH, Fujimoto JG, Chan A, Drexler W, Schuman JS, et al. Ultra-high resolution optical coherence tomography assessment of photoreceptors in retinitis pigmentosa and related diseases. Am J Ophthalmol. 2006;142(6):945-52.
10. Wynne N, Carroll J, Duncan JL. Promises and pitfalls of evaluating photoreceptor-based retinal disease with adaptive optics scanning light ophthalmoscopy (AOSLO). Prog Retin Eye Res. 2021;83:100920.
11. Glatz M, Riedl R, Glatz W, Schneider M, Wedrich A, Bolz M, et al. Blindness and visual impairment in Central Europe. PLoS One. 2022;17(1):e0261897.
12. Liew G, Michaelides M, Bunce C. A comparison of the causes of blindness certifications in England and Wales in working age adults (16-64 years), 1999-2000 with 2009-2010. BMJ Open. 2014;4(2):e004015.
13. Aboshiha J, Dubis AM, Carroll J, Hardcastle AJ, Michaelides M. The cone dysfunction syndromes. Br J Ophthalmol. 2016;100(1):115-21.
14. Michaelides M, Hardcastle AJ, Hunt DM, Moore AT. Progressive cone and cone-rod dystrophies: phenotypes and underlying molecular genetic basis. Surv Ophthalmol. 2006;51(3):232-58.
15. Fujinami K, Zernant J, Chana RK, Wright GA, Tsunoda K, Ozawa Y, et al. Clinical and molecular characteristics of childhood-onset Stargardt disease. Ophthalmology. 2015;122(2):326-34.
16. Georgiou M, Fujinami K, Michaelides M. Inherited retinal diseases: Therapeutics, clinical trials and end points-A review. Clin Exp Ophthalmol. 2021;49(3):270-88.
17. Pontikos N, Arno G, Jurkute N, Schiff E, Ba-Abbad R, Malka S, et al. Genetic Basis of Inherited Retinal Disease in a Molecularly Characterized Cohort of More Than 3000 Families from the United Kingdom. Ophthalmology. 2020;127(10):1384-94.
18. Gao J, Hussain RM, Weng CY. Voretigene Neparvovec in Retinal Diseases: A Review of the Current Clinical Evidence. Clin Ophthalmol. 2020;14:3855-69.
19. MacLaren RE, Groppe M, Barnard AR, Cottriall CL, Tolmachova T, Seymour L, et al. Retinal gene therapy in patients with choroideremia: initial findings from a phase 1/2 clinical trial. Lancet. 2014;383(9923):1129-37.
20. Girach A, Audo I, Birch DG, Huckfeldt RM, Lam BL, Leroy BP, et al. RNA-based therapies in inherited retinal diseases. Ther Adv Ophthalmol. 2022;14:25158414221134602.
21. Weiss JN, Levy S. Stem Cell Ophthalmology Treatment Study (SCOTS): Bone Marrow-Derived Stem Cells in the Treatment of Stargardt Disease. Medicines (Basel). 2021;8(2).

22. Weiss JN, Levy S. Stem Cell Ophthalmology Treatment Study: bone marrow derived stem cells in the treatment of Retinitis Pigmentosa. Stem Cell Investig. 2018;5:18.
23. Busskamp V, Picaud S, Sahel JA, Roska B. Optogenetic therapy for retinitis pigmentosa. Gene Ther. 2012;19(2):169-75.
24. Campochiaro PA, Iftikhar M, Hafiz G, Akhlaq A, Tsai G, Wehling D, et al. Oral N-acetylcysteine improves cone function in retinitis pigmentosa patients in phase I trial. J Clin Invest. 2020;130(3):1527-41.
25. Liu G, Yuan X, Zeng Z, Tunici P, Ng H, Abdulkadir IR, et al. Analysis of gene expression and chemoresistance of CD133+ cancer stem cells in glioblastoma. Mol Cancer. 2006;5:67.
26. Bao S, Wu Q, McLendon RE, Hao Y, Shi Q, Hjelmeland AB, et al. Glioma stem cells promote radioresistance by preferential activation of the DNA damage response. Nature. 2006;444(7120):756-60.
27. Florek M, Haase M, Marzesco AM, Freund D, Ehninger G, Huttner WB, et al. Prominin-1/CD133, a neural and hematopoietic stem cell marker, is expressed in adult human differentiated cells and certain types of kidney cancer. Cell Tissue Res. 2005;319(1):15-26.
28. Yin S, Li J, Hu C, Chen X, Yao M, Yan M, et al. CD133 positive hepatocellular carcinoma cells possess high capacity for tumorigenicity. Int J Cancer. 2007;120(7):1444-50.
29. Weigmann A, Corbeil D, Hellwig A, Huttner WB. Prominin, a novel microvilli-specific polytopic membrane protein of the apical surface of epithelial cells, is targeted to plasmalemmal protrusions of non-epithelial cells. Proc Natl Acad Sci U S A. 1997;94(23):12425-30.
30. Miraglia S, Godfrey W, Yin AH, Atkins K, Warnke R, Holden JT, et al. A novel five-transmembrane hematopoietic stem cell antigen: isolation, characterization, and molecular cloning. Blood. 1997;90(12):5013-21.
31. Röper K, Corbeil D, Huttner WB. Retention of prominin in microvilli reveals distinct cholesterol-based lipid micro-domains in the apical plasma membrane. Nat Cell Biol. 2000;2(9):582-92.
32. Wu R, Kaiser AD. Structure and base sequence in the cohesive ends of bacteriophage lambda DNA. J Mol Biol. 1968;35(3):523-37.
33. Yin AH, Miraglia S, Zanjani ED, Almeida-Porada G, Ogawa M, Leary AG, et al. AC133, a novel marker for human hematopoietic stem and progenitor cells. Blood. 1997;90(12):5002-12.
34. Singh SK, Hawkins C, Clarke ID, Squire JA, Bayani J, Hide T, et al. Identification of human brain tumour initiating cells. Nature. 2004;432(7015):396-401.
35. Ricci-Vitiani L, Lombardi DG, Pilozzi E, Biffoni M, Todaro M, Peschle C, et al. Identification and expansion of human colon-cancer-initiating cells. Nature. 2007;445(7123):111-5.
36. Lee H, Yu DM, Park JS, Lee H, Kim JS, Kim HL, et al. Prominin-1-Radixin axis controls hepatic gluconeogenesis by regulating PKA activity. EMBO Rep. 2020;21(11):e49416.
37. Lee H, Yu DM, Bahn MS, Kwon YJ, Um MJ, Yoon SY, et al. Hepatocyte-specific Prominin-1 protects against liver injury-induced fibrosis by stabilizing SMAD7. Exp Mol Med. 2022;54(8):1277-89.
38. Bahn MS, Yu DM, Lee M, Jo SJ, Lee JW, Kim HC, et al. Central role of Prominin-1 in lipid rafts during liver regeneration. Nat Commun. 2022;13(1):6219.
39. Zhu L, Gibson P, Currle DS, Tong Y, Richardson RJ, Bayazitov IT, et al. Prominin 1 marks intestinal stem cells that are susceptible to neoplastic transformation. Nature. 2009;457(7229):603-7.
40. Lee J, Shin JE, Lee B, Kim H, Jeon Y, Ahn SH, et al. The stem cell marker Prom1 promotes axon regeneration by down-regulating cholesterol synthesis via Smad signaling. Proc Natl Acad Sci U S A. 2020;117(27):15955-66.

41. Zacchigna S, Oh H, Wilsch-Bräuninger M, Missol-Kolka E, Jászai J, Jansen S, et al. Loss of the cholesterol-binding protein prominin-1/CD133 causes disk dysmorphogenesis and photoreceptor degeneration. J Neurosci. 2009;29(7):2297-308.
42. Choi MH, Na JE, Yoon YR, Rhyu IJ, Ko YG, Baik JH. Hypomyelination and cognitive impairment in mice lacking CD133 (Prominin-1). Biochem Biophys Res Commun. 2018;502(3):291-8.
43. Singer D, Thamm K, Zhuang H, Karbanová J, Gao Y, Walker JV, et al. Prominin-1 controls stem cell activation by orchestrating ciliary dynamics. Embo j. 2019;38(2).
44. Fargeas CA, Corbeil D, Huttner WB. AC133 antigen, CD133, prominin-1, prominin-2, etc.: prominin family gene products in need of a rational nomenclature. Stem Cells. 2003;21(4):506-8.
45. Jászai J, Fargeas CA, Graupner S, Tanaka EM, Brand M, Huttner WB, et al. Distinct and conserved prominin-1/CD133-positive retinal cell populations identified across species. PLoS One. 2011;6(3):e17590.
46. Yang L, Shi P, Zhao G, Xu J, Peng W, Zhang J, et al. Targeting cancer stem cell pathways for cancer therapy. Signal Transduct Target Ther. 2020;5(1):8.
47. Mak AB, Nixon AM, Kittanakom S, Stewart JM, Chen GI, Curak J, et al. Regulation of CD133 by HDAC6 promotes β-catenin signaling to suppress cancer cell differentiation. Cell Rep. 2012;2(4):951-63.
48. Soeda A, Park M, Lee D, Mintz A, Androutsellis-Theotokis A, McKay RD, et al. Hypoxia promotes expansion of the CD133-positive glioma stem cells through activation of HIF-1alpha. Oncogene. 2009;28(45):3949-59.
49. Won C, Kim BH, Yi EH, Choi KJ, Kim EK, Jeong JM, et al. Signal transducer and activator of transcription 3-mediated CD133 up-regulation contributes to promotion of hepatocellular carcinoma. Hepatology. 2015;62(4):1160-73.
50. Shmelkov SV, Butler JM, Hooper AT, Hormigo A, Kushner J, Milde T, et al. CD133 expression is not restricted to stem cells, and both CD133+ and CD133- metastatic colon cancer cells initiate tumors. J Clin Invest. 2008;118(6):2111-20.
51. Sureban SM, May R, Ramalingam S, Subramaniam D, Natarajan G, Anant S, et al. Selective blockade of DCAMKL-1 results in tumor growth arrest by a Let-7a MicroRNA-dependent mechanism. Gastroenterology. 2009;137(2):649-59, 59.e1-2.
52. Maw MA, Corbeil D, Koch J, Hellwig A, Wilson-Wheeler JC, Bridges RJ, et al. A frameshift mutation in prominin (mouse)-like 1 causes human retinal degeneration. Hum Mol Genet. 2000;9(1):27-34.
53. Corbeil D, Röper K, Hellwig A, Tavian M, Miraglia S, Watt SM, et al. The human AC133 hematopoietic stem cell antigen is also expressed in epithelial cells and targeted to plasma membrane protrusions. J Biol Chem. 2000;275(8):5512-20.
54. Karbanová J, Missol-Kolka E, Fonseca AV, Lorra C, Janich P, Hollerová H, et al. The stem cell marker CD133 (Prominin-1) is expressed in various human glandular epithelia. J Histochem Cytochem. 2008;56(11):977-93.
55. Karbanová J, Lorico A, Bornhäuser M, Corbeil D, Fargeas CA. Prominin-1/CD133: Lipid Raft Association, Detergent Resistance, and Immunodetection. Stem Cells Transl Med. 2018;7(2):155-60.
56. Yang Z, Chen Y, Lillo C, Chien J, Yu Z, Michaelides M, et al. Mutant prominin 1 found in patients with macular degeneration disrupts photoreceptor disk morphogenesis in mice. J Clin Invest. 2008;118(8):2908-16.
57. Strauss RW, Munoz B, Ahmed MI, Bittencourt M, Schonbach EM, Michaelides M, et al. The Progression of the Stargardt Disease Type 4 (ProgStar-4) Study: Design and Baseline Characteristics (ProgStar-4 Report No. 1). Ophthalmic Res. 2018;60(3):185-94.
58. Bhattacharya S, Yin J, Winborn CS, Zhang Q, Yue J, Chaum E. Prominin-1 Is a Novel Regulator of Autophagy in the Human Retinal Pigment Epithelium. Invest Ophthalmol Vis Sci. 2017;58(4):2366-87.

59. Wang Y, Wang P, Li S, Ouyang J, Jia X, Xiao X, et al. Characterization of PROM1 p.Arg373Cys Variant in a Cohort of Chinese Patients: Macular Dystrophy Plus Peripheral Bone-Spicule Degeneration. Invest Ophthalmol Vis Sci. 2021;62(6):19.
60. Permanyer J, Navarro R, Friedman J, Pomares E, Castro-Navarro J, Marfany G, et al. Autosomal recessive retinitis pigmentosa with early macular affectation caused by premature truncation in PROM1. Invest Ophthalmol Vis Sci. 2010;51(5):2656-63.
61. Mayer AK, Rohrschneider K, Strom TM, Glöckle N, Kohl S, Wissinger B, et al. Homozygosity mapping and whole-genome sequencing reveals a deep intronic PROM1 mutation causing cone-rod dystrophy by pseudoexon activation. Eur J Hum Genet. 2016;24(3):459-62.
62. Pras E, Abu A, Rotenstreich Y, Avni I, Reish O, Morad Y, et al. Cone-rod dystrophy and a frameshift mutation in the PROM1 gene. Mol Vis. 2009;15:1709-16.
63. Michaelides M, Gaillard MC, Escher P, Tiab L, Bedell M, Borruat FX, et al. The PROM1 mutation p.R373C causes an autosomal dominant bull's eye maculopathy associated with rod, rod-cone, and macular dystrophy. Invest Ophthalmol Vis Sci. 2010;51(9):4771-80.
64. Cehajic-Kapetanovic J, Birtel J, McClements ME, Shanks ME, Clouston P, Downes SM, et al. Clinical and Molecular Characterization of PROM1-Related Retinal Degeneration. JAMA Netw Open. 2019;2(6):e195752.
65. Carss KJ, Arno G, Erwood M, Stephens J, Sanchis-Juan A, Hull S, et al. Comprehensive Rare Variant Analysis via Whole-Genome Sequencing to Determine the Molecular Pathology of Inherited Retinal Disease. Am J Hum Genet. 2017;100(1):75-90.
66. Wawrocka A, Skorczyk-Werner A, Wicher K, Niedziela Z, Ploski R, Rydzanicz M, et al. Novel variants identified with next-generation sequencing in Polish patients with cone-rod dystrophy. Mol Vis. 2018;24:326-39.
67. Palejwala NV, Gale MJ, Clark RF, Schlechter C, Weleber RG, Pennesi ME. INSIGHTS INTO AUTOSOMAL DOMINANT STARGARDT-LIKE MACULAR DYSTROPHY THROUGH MULTIMODALITY DIAGNOSTIC IMAGING. Retina. 2016;36(1):119-30.
68. Dellett M, Sasai N, Nishide K, Becker S, Papadaki V, Limb GA, et al. Genetic background and light-dependent progression of photoreceptor cell degeneration in Prominin-1 knockout mice. Invest Ophthalmol Vis Sci. 2014;56(1):164-76.
69. Zhang Q, Zulfiqar F, Xiao X, Riazuddin SA, Ahmad Z, Caruso R, et al. Severe retinitis pigmentosa mapped to 4p15 and associated with a novel mutation in the PROM1 gene. Hum Genet. 2007;122(3-4):293-9.
70. Trigt ACv. Dissertatio ophthalmologica inauguralis de speculo oculi. PW van de Weijer; 1853.
71. Purkinje Jv. Beytr/ige zur Kenntniss des Sehens in subjectiver Hinsicht. Prag: Calve. 1819.
72. Gerloff O. Uber die photographie des augenhintergrundes. Klin Monatsblätter Augenheilkunde. 1891;29:397-403.
73. Gullstrand A. Neue methoden der reflexlosen ophthalmoskopie. Berichte Deutsche Ophthalmologische Gesellschaft. 1910;36(8):326.
74. Novotny HR, Alvis DL. A method of photographing fluorescence in circulating blood in the human retina. Circulation. 1961;24:82-6.
75. Abràmoff MD, Garvin MK, Sonka M. Retinal imaging and image analysis. IEEE Rev Biomed Eng. 2010;3:169-208.
76. Allen L. OCULAR FUNDUS PHOTOGRAPHY: SUGGESTIONS FOR ACHIEVING CONSISTENTLY GOOD PICTURES AND INSTRUCTIONS FOR STEREOSCOPIC PHOTOGRAPHY. Am J Ophthalmol. 1964;57:13-28.
77. Webb RH, Hughes GW. Scanning laser ophthalmoscope. IEEE Trans Biomed Eng. 1981;28(7):488-92.

78. van Velthoven ME, Faber DJ, Verbraak FD, van Leeuwen TG, de Smet MD. Recent developments in optical coherence tomography for imaging the retina. Prog Retin Eye Res. 2007;26(1):57-77.
79. Panwar N, Huang P, Lee J, Keane PA, Chuan TS, Richhariya A, et al. Fundus Photography in the 21st Century--A Review of Recent Technological Advances and Their Implications for Worldwide Healthcare. Telemed J E Health. 2016;22(3):198-208.
80. Huang D, Swanson EA, Lin CP, Schuman JS, Stinson WG, Chang W, et al. Optical coherence tomography. Science. 1991;254(5035):1178-81.
81. Drexler W, Fujimoto JG. State-of-the-art retinal optical coherence tomography. Prog Retin Eye Res. 2008;27(1):45-88.
82. Choma M, Sarunic M, Yang C, Izatt J. Sensitivity advantage of swept source and Fourier domain optical coherence tomography. Opt Express. 2003;11(18):2183-9.
83. Photocoagulation for diabetic macular edema. Early Treatment Diabetic Retinopathy Study report number 1. Early Treatment Diabetic Retinopathy Study research group. Arch Ophthalmol. 1985;103(12):1796-806.
84. Kong X, Ho A, Munoz B, West S, Strauss RW, Jha A, et al. Reproducibility of Measurements of Retinal Structural Parameters Using Optical Coherence Tomography in Stargardt Disease. Transl Vis Sci Technol. 2019;8(3):46.
85. Bhende M, Shetty S, Parthasarathy MK, Ramya S. Optical coherence tomography: A guide to interpretation of common macular diseases. Indian J Ophthalmol. 2018;66(1):20-35.
86. Kafieh R, Rabbani H, Kermani S. A review of algorithms for segmentation of optical coherence tomography from retina. J Med Signals Sens. 2013;3(1):45-60.
87. Cifuentes-Canorea P, Ruiz-Medrano J, Gutierrez-Bonet R, Peña-Garcia P, Saenz-Frances F, Garcia-Feijoo J, et al. Analysis of inner and outer retinal layers using spectral domain optical coherence tomography automated segmentation software in ocular hypertensive and glaucoma patients. PLoS One. 2018;13(4):e0196112.
88. Chen B, Chen H, Zheng C, Zhang M. Performance of Topcon 3D optical coherence tomography-2000 in re-analyzing OCT-1000 raw data. Exp Ther Med. 2019;17(6):4395-402.
89. Gheorghe A, Mahdi L, Musat O. AGE-RELATED MACULAR DEGENERATION. Rom J Ophthalmol. 2015;59(2):74-7.
90. Lang GE. Optical coherence tomography findings in diabetic retinopathy. Dev Ophthalmol. 2007;39:31-47.
91. Lindtjørn B, Krohn J, Forsaa VA. Optical coherence tomography features and risk of macular hole formation in the fellow eye. BMC Ophthalmol. 2021;21(1):351.
92. Schmidt-Erfurth U, Garcia-Arumi J, Gerendas BS, Midena E, Sivaprasad S, Tadayoni R, et al. Guidelines for the Management of Retinal Vein Occlusion by the European Society of Retina Specialists (EURETINA). Ophthalmologica. 2019;242(3):123-62.
93. Geevarghese A, Wollstein G, Ishikawa H, Schuman JS. Optical Coherence Tomography and Glaucoma. Annu Rev Vis Sci. 2021;7:693-726.
94. Delori FC, Dorey CK, Staurenghi G, Arend O, Goger DG, Weiter JJ. In vivo fluorescence of the ocular fundus exhibits retinal pigment epithelium lipofuscin characteristics. Invest Ophthalmol Vis Sci. 1995;36(3):718-29.
95. Lois N, Halfyard AS, Bird AC, Fitzke FW. Quantitative evaluation of fundus autofluorescence imaged "in vivo" in eyes with retinal disease. Br J Ophthalmol. 2000;84(7):741-5.
96. Lois N, Forrester JV. Fundus autofluorescence: Lippincott Williams & Wilkins; 2009.
97. Delori FC, Goger DG, Dorey CK. Age-related accumulation and spatial distribution of lipofuscin in RPE of normal subjects. Invest Ophthalmol Vis Sci. 2001;42(8):1855-66.
98. Sparrow JR, Nakanishi K, Parish CA. The lipofuscin fluorophore A2E mediates blue light-induced damage to retinal pigmented epithelial cells. Invest Ophthalmol Vis Sci. 2000;41(7):1981-9.

99. Feng J, Chen X, Sun X, Wang F, Sun X. Expression of endoplasmic reticulum stress markers GRP78 and CHOP induced by oxidative stress in blue light-mediated damage of A2E-containing retinal pigment epithelium cells. Ophthalmic Res. 2014;52(4):224-33.
100. Ben-Shabat S, Itagaki Y, Jockusch S, Sparrow J, Turro N, Nakanishi K. ZUSCHRIFTEN-Formation of a Nonaoxirane from A2E, a Lipofuscin Fluorophore related to Macular Degeneration, and Evidence of Singlet Oxygen Involvement. Angewandte Chemie-German Edition. 2002;114(5):842-4.
101. Sparrow JR, Vollmer-Snarr HR, Zhou J, Jang YP, Jockusch S, Itagaki Y, et al. A2E-epoxides damage DNA in retinal pigment epithelial cells. Vitamin E and other antioxidants inhibit A2E-epoxide formation. J Biol Chem. 2003;278(20):18207-13.
102. Wu Y, Yanase E, Feng X, Siegel MM, Sparrow JR. Structural characterization of bisretinoid A2E photocleavage products and implications for age-related macular degeneration. Proc Natl Acad Sci U S A. 2010;107(16):7275-80.
103. Roberts JE, Kukielczak BM, Hu DN, Miller DS, Bilski P, Sik RH, et al. The role of A2E in prevention or enhancement of light damage in human retinal pigment epithelial cells. Photochem Photobiol. 2002;75(2):184-90.
104. Maeda A, Golczak M, Chen Y, Okano K, Kohno H, Shiose S, et al. Primary amines protect against retinal degeneration in mouse models of retinopathies. Nat Chem Biol. 2011;8(2):170-8.
105. Ablonczy Z, Higbee D, Anderson DM, Dahrouj M, Grey AC, Gutierrez D, et al. Lack of correlation between the spatial distribution of A2E and lipofuscin fluorescence in the human retinal pigment epithelium. Invest Ophthalmol Vis Sci. 2013;54(8):5535-42.
106. Crouch RK, Koutalos Y, Kono M, Schey K, Ablonczy Z. A2E and Lipofuscin. Prog Mol Biol Transl Sci. 2015;134:449-63.
107. Beatty S, Murray IJ, Henson DB, Carden D, Koh H, Boulton ME. Macular pigment and risk for age-related macular degeneration in subjects from a Northern European population. Invest Ophthalmol Vis Sci. 2001;42(2):439-46.
108. Snodderly DM, Brown PK, Delori FC, Auran JD. The macular pigment. I. Absorbance spectra, localization, and discrimination from other yellow pigments in primate retinas. Invest Ophthalmol Vis Sci. 1984;25(6):660-73.
109. Elsner AE, Burns SA, Weiter JJ, Delori FC. Infrared imaging of sub-retinal structures in the human ocular fundus. Vision Res. 1996;36(1):191-205.
110. Dysli C, Wolf S, Zinkernagel MS. Autofluorescence Lifetimes in Geographic Atrophy in Patients With Age-Related Macular Degeneration. Invest Ophthalmol Vis Sci. 2016;57(6):2479-87.
111. Schmitz-Valckenberg S, Holz FG, Bird AC, Spaide RF. Fundus autofluorescence imaging: review and perspectives. Retina. 2008;28(3):385-409.
112. Delori F, Greenberg JP, Woods RL, Fischer J, Duncker T, Sparrow J, et al. Quantitative measurements of autofluorescence with the scanning laser ophthalmoscope. Invest Ophthalmol Vis Sci. 2011;52(13):9379-90.
113. Armenti ST, Greenberg JP, Smith RT. Quantitative Fundus Autofluorescence for the Evaluation of Retinal Diseases. J Vis Exp. 2016(109).
114. Eandi CM, Nassisi M, Lavia C, Alovisi C, de Sanctis U. Macular Pigment Density and Quantitative Fundus Autofluorescence in Young Healthy Subjects. Invest Ophthalmol Vis Sci. 2017;58(4):2284-90.
115. Greenberg JP, Duncker T, Woods RL, Smith RT, Sparrow JR, Delori FC. Quantitative fundus autofluorescence in healthy eyes. Invest Ophthalmol Vis Sci. 2013;54(8):5684-93.
116. Gliem M, Müller PL, Finger RP, McGuinness MB, Holz FG, Charbel Issa P. Quantitative Fundus Autofluorescence in Early and Intermediate Age-Related Macular Degeneration. JAMA Ophthalmol. 2016;134(7):817-24.
117. Duncker T, Tsang SH, Woods RL, Lee W, Zernant J, Allikmets R, et al. Quantitative Fundus Autofluorescence and Optical Coherence Tomography in PRPH2/RDS- and ABCA4-

Associated Disease Exhibiting Phenotypic Overlap. Invest Ophthalmol Vis Sci. 2015;56(5):3159-70.
118. Boudreault KA, Schuerch K, Zhao J, Lee W, Cabral T, Yannuzzi LA, et al. Quantitative Autofluorescence Intensities in Acute Zonal Occult Outer Retinopathy vs Healthy Eyes. JAMA Ophthalmol. 2017;135(12):1330-8.
119. Liang J, Williams DR, Miller DT. Supernormal vision and high-resolution retinal imaging through adaptive optics. J Opt Soc Am A Opt Image Sci Vis. 1997;14(11):2884-92.
120. Liang J, Grimm B, Goelz S, Bille JF. Objective measurement of wave aberrations of the human eye with the use of a Hartmann-Shack wave-front sensor. J Opt Soc Am A Opt Image Sci Vis. 1994;11(7):1949-57.
121. Liang J, Williams DR. Aberrations and retinal image quality of the normal human eye. J Opt Soc Am A Opt Image Sci Vis. 1997;14(11):2873-83.
122. Roorda A. Adaptive optics for studying visual function: a comprehensive review. J Vis. 2011;11(7).
123. Porter J, Queener H, Lin J, Thorn K, Awwal A. Adaptive optics for vision science. 2006.
124. Miller A, Roorda A. Handbook of optics. Vol I: Fundamentals, Techniques, and Design. 1994:9.1-9.33.
125. Webb RH, Hughes GW, Pomerantzeff O. Flying spot TV ophthalmoscope. Appl Opt. 1980;19(17):2991-7.
126. Gill JS, Moosajee M, Dubis AM. Cellular imaging of inherited retinal diseases using adaptive optics. Eye (Lond). 2019;33(11):1683-98.
127. Roorda A, Duncan JL. Adaptive optics ophthalmoscopy. Annu Rev Vis Sci. 2015;1:19-50.
128. Dubra A, Sulai Y, Norris JL, Cooper RF, Dubis AM, Williams DR, et al. Noninvasive imaging of the human rod photoreceptor mosaic using a confocal adaptive optics scanning ophthalmoscope. Biomed Opt Express. 2011;2(7):1864-76.
129. Georgiou M, Singh N, Kane T, Robson AG, Kalitzeos A, Hirji N, et al. Photoreceptor Structure in GNAT2-Associated Achromatopsia. Invest Ophthalmol Vis Sci. 2020;61(3):40.
130. Georgiou M, Kalitzeos A, Patterson EJ, Dubra A, Carroll J, Michaelides M. Adaptive optics imaging of inherited retinal diseases. Br J Ophthalmol. 2018;102(8):1028-35.
131. Scoles D, Sulai YN, Langlo CS, Fishman GA, Curcio CA, Carroll J, et al. In vivo imaging of human cone photoreceptor inner segments. Invest Ophthalmol Vis Sci. 2014;55(7):4244-51.
132. Beck RW, Maguire MG, Bressler NM, Glassman AR, Lindblad AS, Ferris FL. Visual acuity as an outcome measure in clinical trials of retinal diseases. Ophthalmology. 2007;114(10):1804-9.
133. Zang J, Gesemann M, Keim J, Samardzija M, Grimm C, Neuhauss SC. Circadian regulation of vertebrate cone photoreceptor function. Elife. 2021;10.
134. Scholl HP, Strauss RW, Singh MS, Dalkara D, Roska B, Picaud S, et al. Emerging therapies for inherited retinal degeneration. Sci Transl Med. 2016;8(368):368rv6.
135. World Medical Association Declaration of Helsinki. Ethical principles for medical research involving human subjects. Bull World Health Organ. 2001;79(4):373-4.
136. Strauss RW, Munoz B, Jha A, Ho A, Cideciyan AV, Kasilian ML, et al. Comparison of Short-Wavelength Reduced-Illuminance and Conventional Autofluorescence Imaging in Stargardt Macular Dystrophy. Am J Ophthalmol. 2016;168:269-78.
137. Strauss RW, Ho A, Munoz B, Cideciyan AV, Sahel JA, Sunness JS, et al. The Natural History of the Progression of Atrophy Secondary to Stargardt Disease (ProgStar) Studies: Design and Baseline Characteristics: ProgStar Report No. 1. Ophthalmology. 2016;123(4):817-28.

138. Strauss RW, Kong X, Ho A, Jha A, West S, Ip M, et al. Progression of Stargardt Disease as Determined by Fundus Autofluorescence Over a 12-Month Period: ProgStar Report No. 11. JAMA Ophthalmol. 2019;137(10):1134-45.
139. Velaga SB, Nittala MG, Jenkins D, Melendez J, Ho A, Strauss RW, et al. Impact of segmentation density on spectral domain optical coherence tomography assessment in Stargardt disease. Graefes Arch Clin Exp Ophthalmol. 2019;257(3):549-56.
140. GraphPad Software 2023 [Available from: https://www.graphpad.com/quickcalcs/ttest1.cfm.
141. Salmon AE, Cooper RF, Langlo CS, Baghaie A, Dubra A, Carroll J. An Automated Reference Frame Selection (ARFS) Algorithm for Cone Imaging with Adaptive Optics Scanning Light Ophthalmoscopy. Transl Vis Sci Technol. 2017;6(2):9.
142. Davidson B, Kalitzeos A, Carroll J, Dubra A, Ourselin S, Michaelides M, et al. Fast adaptive optics scanning light ophthalmoscope retinal montaging. Biomed Opt Express. 2018;9(9):4317-28.
143. Georgiou M, Robson AG, Singh N, Pontikos N, Kane T, Hirji N, et al. Deep Phenotyping of PDE6C-Associated Achromatopsia. Invest Ophthalmol Vis Sci. 2019;60(15):5112-23.
144. Georgiou M, Litts KM, Kalitzeos A, Langlo CS, Kane T, Singh N, et al. Adaptive Optics Retinal Imaging in CNGA3-Associated Achromatopsia: Retinal Characterization, Interocular Symmetry, and Intrafamilial Variability. Invest Ophthalmol Vis Sci. 2019;60(1):383-96.
145. Jackson K, Vergilio GK, Cooper RF, Ying GS, Morgan JIW. A 2-Year Longitudinal Study of Normal Cone Photoreceptor Density. Invest Ophthalmol Vis Sci. 2019;60(5):1420-30.
146. den Dunnen JT. Describing Sequence Variants Using HGVS Nomenclature. Methods Mol Biol. 2017;1492:243-51.
147. Richards S, Aziz N, Bale S, Bick D, Das S, Gastier-Foster J, et al. Standards and guidelines for the interpretation of sequence variants: a joint consensus recommendation of the American College of Medical Genetics and Genomics and the Association for Molecular Pathology. Genet Med. 2015;17(5):405-24.
148. Csaky K, Ferris F, 3rd, Chew EY, Nair P, Cheetham JK, Duncan JL. Report From the NEI/FDA Endpoints Workshop on Age-Related Macular Degeneration and Inherited Retinal Diseases. Invest Ophthalmol Vis Sci. 2017;58(9):3456-63.
149. Holz FG, Sadda SR, Staurenghi G, Lindner M, Bird AC, Blodi BA, et al. Imaging Protocols in Clinical Studies in Advanced Age-Related Macular Degeneration: Recommendations from Classification of Atrophy Consensus Meetings. Ophthalmology. 2017;124(4):464-78.
150. Gliem M, Muller PL, Birtel J, Herrmann P, McGuinness MB, Holz FG, et al. Quantitative Fundus Autofluorescence and Genetic Associations in Macular, Cone, and Cone-Rod Dystrophies. Ophthalmol Retina. 2020;4(7):737-49.
151. Paavo M, Lee W, Parmann R, Lima de Carvalho JR, Jr., Zernant J, Tsang SH, et al. Insights Into PROM1-Macular Disease Using Multimodal Imaging. Invest Ophthalmol Vis Sci. 2023;64(4):27.
152. Duncker T, Tsang SH, Lee W, Zernant J, Allikmets R, Delori FC, et al. Quantitative fundus autofluorescence distinguishes ABCA4-associated and non-ABCA4-associated bull's-eye maculopathy. Ophthalmology. 2015;122(2):345-55.
153. Mitani AA, Haneuse S. Small Data Challenges of Studying Rare Diseases. JAMA Network Open. 2020;3(3):e201965-e.
154. Sheck LHN, Esposti SD, Mahroo OA, Arno G, Pontikos N, Wright G, et al. Panel-based genetic testing for inherited retinal disease screening 176 genes. Mol Genet Genomic Med. 2021;9(12):e1663.
155. Langlo CS, Patterson EJ, Higgins BP, Summerfelt P, Razeen MM, Erker LR, et al. Residual Foveal Cone Structure in CNGB3-Associated Achromatopsia. Invest Ophthalmol Vis Sci. 2016;57(10):3984-95.

156. Sheehy CK, Tiruveedhula P, Sabesan R, Roorda A. Active eye-tracking for an adaptive optics scanning laser ophthalmoscope. Biomed Opt Express. 2015;6(7):2412-23.
157. Tam J, Roorda A. Speed quantification and tracking of moving objects in adaptive optics scanning laser ophthalmoscopy. J Biomed Opt. 2011;16(3):036002.
158. Privitera CM, Sabesan R, Winter S, Tiruveedhula P, Roorda A. Eye-tracking technology for real-time monitoring of transverse chromatic aberration. Opt Lett. 2016;41(8):1728-31.
159. Martinez-Marquez D, Pingali S, Panuwatwanich K, Stewart RA, Mohamed S. Application of Eye Tracking Technology in Aviation, Maritime, and Construction Industries: A Systematic Review. Sensors. 2021;21(13):4289.
160. Park SP, Chung JK, Greenstein V, Tsang SH, Chang S. A study of factors affecting the human cone photoreceptor density measured by adaptive optics scanning laser ophthalmoscope. Exp Eye Res. 2013;108:1-9.
161. Tumahai P, Moureaux C, Meillat M, Debellemanière G, Flores M, Delbosc B, et al. High-resolution imaging of photoreceptors in healthy human eyes using an adaptive optics retinal camera. Eye (Lond). 2018;32(11):1723-30.
162. Bergeles C, Dubis AM, Davidson B, Kasilian M, Kalitzeos A, Carroll J, et al. Unsupervised identification of cone photoreceptors in non-confocal adaptive optics scanning light ophthalmoscope images. Biomed Opt Express. 2017;8(6):3081-94.
163. Roorda A, Williams DR. The arrangement of the three cone classes in the living human eye. Nature. 1999;397(6719):520-2.
164. Duncan JL, Roorda A. Dysflective Cones. Adv Exp Med Biol. 2019;1185:133-7.
165. Alpern M, Ching CC, Kitahara K. The directional sensitivity of retinal rods. J Physiol. 1983;343:577-92.
166. Morgan JI, Dubra A, Wolfe R, Merigan WH, Williams DR. In vivo autofluorescence imaging of the human and macaque retinal pigment epithelial cell mosaic. Invest Ophthalmol Vis Sci. 2009;50(3):1350-9.
167. Roorda A, Zhang Y, Duncan JL. High-resolution in vivo imaging of the RPE mosaic in eyes with retinal disease. Invest Ophthalmol Vis Sci. 2007;48(5):2297-303.
168. Rossi EA, Granger CE, Sharma R, Yang Q, Saito K, Schwarz C, et al. Imaging individual neurons in the retinal ganglion cell layer of the living eye. Proc Natl Acad Sci U S A. 2017;114(3):586-91.
169. Liu Z, Kurokawa K, Zhang F, Lee JJ, Miller DT. Imaging and quantifying ganglion cells and other transparent neurons in the living human retina. Proc Natl Acad Sci U S A. 2017;114(48):12803-8.
170. Ivers KM, Li C, Patel N, Sredar N, Luo X, Queener H, et al. Reproducibility of measuring lamina cribrosa pore geometry in human and nonhuman primates with in vivo adaptive optics imaging. Invest Ophthalmol Vis Sci. 2011;52(8):5473-80.
171. Burns SA, Elsner AE, Chui TY, Vannasdale DA, Jr., Clark CA, Gast TJ, et al. In vivo adaptive optics microvascular imaging in diabetic patients without clinically severe diabetic retinopathy. Biomed Opt Express. 2014;5(3):961-74.
172. Roorda A, Romero-Borja F, Donnelly Iii W, Queener H, Hebert T, Campbell M. Adaptive optics scanning laser ophthalmoscopy. Opt Express. 2002;10(9):405-12.
173. Wilk MA, McAllister JT, Cooper RF, Dubis AM, Patitucci TN, Summerfelt P, et al. Relationship between foveal cone specialization and pit morphology in albinism. Invest Ophthalmol Vis Sci. 2014;55(7):4186-98.
174. Gocho K, Sarda V, Falah S, Sahel J-A, Sennlaub F, Benchaboune M, et al. Adaptive Optics Imaging of Geographic Atrophy. Investigative Ophthalmology & Visual Science. 2013;54(5):3673-80.
175. Querques G, Kamami-Levy C, Georges A, Pedinielli A, Capuano V, Blanco-Garavito R, et al. ADAPTIVE OPTICS IMAGING OF FOVEAL SPARING IN GEOGRAPHIC ATROPHY SECONDARY TO AGE-RELATED MACULAR DEGENERATION. Retina. 2016;36(2):247-54.

176. Davoudi S, Ebrahimiadib N, Yasa C, Sevgi DD, Roohipoor R, Papavasilieou E, et al. Outcomes in Autoimmune Retinopathy Patients Treated With Rituximab. Am J Ophthalmol. 2017;180:124-32.
177. Marcos S, Werner JS, Burns SA, Merigan WH, Artal P, Atchison DA, et al. Vision science and adaptive optics, the state of the field. Vision Res. 2017;132:3-33.
178. Wang Q, Tuten WS, Lujan BJ, Holland J, Bernstein PS, Schwartz SD, et al. Adaptive optics microperimetry and OCT images show preserved function and recovery of cone visibility in macular telangiectasia type 2 retinal lesions. Invest Ophthalmol Vis Sci. 2015;56(2):778-86.
179. Bruce KS, Harmening WM, Langston BR, Tuten WS, Roorda A, Sincich LC. Normal Perceptual Sensitivity Arising From Weakly Reflective Cone Photoreceptors. Invest Ophthalmol Vis Sci. 2015;56(8):4431-8.
180. Tuten WS, Tiruveedhula P, Roorda A. Adaptive optics scanning laser ophthalmoscope-based microperimetry. Optom Vis Sci. 2012;89(5):563-74.
181. Wynne N, Heitkotter H, Woertz EN, Cooper RF, Carroll J. Comparison of Cone Mosaic Metrics From Images Acquired With the SPECTRALIS High Magnification Module and Adaptive Optics Scanning Light Ophthalmoscopy. Transl Vis Sci Technol. 2022;11(5):19.
182. Konstantinou EK, Mendonça LSM, Braun P, Monahan KM, Mehta N, Gendelman I, et al. Retinal Imaging Using a Confocal Scanning Laser Ophthalmoscope-Based High-Magnification Module. Ophthalmol Retina. 2021;5(5):438-49.
183. Mendonça LSM, Braun PX, Martin SM, Hüther A, Mehta N, Zhao Y, et al. Repeatability and Reproducibility of Photoreceptor Density Measurement in the Macula Using the Spectralis High Magnification Module. Ophthalmol Retina. 2020;4(11):1083-92.
184. Cideciyan AV, Swider M, Aleman TS, Roman MI, Sumaroka A, Schwartz SB, et al. Reduced-illuminance autofluorescence imaging in ABCA4-associated retinal degenerations. J Opt Soc Am A Opt Image Sci Vis. 2007;24(5):1457-67.
185. Reiter GS, Told R, Baumann L, Sacu S, Schmidt-Erfurth U, Pollreisz A. INVESTIGATING A GROWTH PREDICTION MODEL IN ADVANCED AGE-RELATED MACULAR DEGENERATION WITH SOLITARY GEOGRAPHIC ATROPHY USING QUANTITATIVE AUTOFLUORESCENCE. Retina. 2020;40(9):1657-64.
186. Kleefeldt N, Bermond K, Tarau IS, Hillenkamp J, Berlin A, Sloan KR, et al. Quantitative Fundus Autofluorescence: Advanced Analysis Tools. Transl Vis Sci Technol. 2020;9(8):2.
187. Miere A, Le Meur T, Bitton K, Pallone C, Semoun O, Capuano V, et al. Deep Learning-Based Classification of Inherited Retinal Diseases Using Fundus Autofluorescence. J Clin Med. 2020;9(10).
188. Schmitz-Valckenberg S, Pfau M, Fleckenstein M, Staurenghi G, Sparrow JR, Bindewald-Wittich A, et al. Fundus autofluorescence imaging. Prog Retin Eye Res. 2021;81:100893.
189. Dysli C, Wolf S, Berezin MY, Sauer L, Hammer M, Zinkernagel MS. Fluorescence lifetime imaging ophthalmoscopy. Prog Retin Eye Res. 2017;60:120-43.
190. Dysli C, Quellec G, Abegg M, Menke MN, Wolf-Schnurrbusch U, Kowal J, et al. Quantitative analysis of fluorescence lifetime measurements of the macula using the fluorescence lifetime imaging ophthalmoscope in healthy subjects. Invest Ophthalmol Vis Sci. 2014;55(4):2106-13.
191. Sauer L, Andersen KM, Li B, Gensure RH, Hammer M, Bernstein PS. Fluorescence Lifetime Imaging Ophthalmoscopy (FLIO) of Macular Pigment. Invest Ophthalmol Vis Sci. 2018;59(7):3094-103.
192. Sauer L, Gensure RH, Andersen KM, Kreilkamp L, Hageman GS, Hammer M, et al. Patterns of Fundus Autofluorescence Lifetimes In Eyes of Individuals With Nonexudative Age-Related Macular Degeneration. Invest Ophthalmol Vis Sci. 2018;59(4):Amd65-amd77.

193. Sauer L, Gensure RH, Hammer M, Bernstein PS. Fluorescence Lifetime Imaging Ophthalmoscopy: A Novel Way to Assess Macular Telangiectasia Type 2. Ophthalmol Retina. 2018;2(6):587-98.
194. Dysli C, Wolf S, Hatz K, Zinkernagel MS. Fluorescence Lifetime Imaging in Stargardt Disease: Potential Marker for Disease Progression. Invest Ophthalmol Vis Sci. 2016;57(3):832-41.
195. Sauer L, Calvo CM, Vitale AS, Henrie N, Milliken CM, Bernstein PS. Imaging of Hydroxychloroquine Toxicity with Fluorescence Lifetime Imaging Ophthalmoscopy. Ophthalmol Retina. 2019;3(10):814-25.
196. Dysli C, Wolf S, Tran HV, Zinkernagel MS. Autofluorescence Lifetimes in Patients With Choroideremia Identify Photoreceptors in Areas With Retinal Pigment Epithelium Atrophy. Invest Ophthalmol Vis Sci. 2016;57(15):6714-21.
197. Pole C, Ameri H. Fundus Autofluorescence and Clinical Applications. J Ophthalmic Vis Res. 2021;16(3):432-61.
198. Mishra Z, Wang Z, Sadda SR, Hu Z. Automatic Segmentation in Multiple OCT Layers For Stargardt Disease Characterization Via Deep Learning. Transl Vis Sci Technol. 2021;10(4):24.
199. Fang L, Cunefare D, Wang C, Guymer RH, Li S, Farsiu S. Automatic segmentation of nine retinal layer boundaries in OCT images of non-exudative AMD patients using deep learning and graph search. Biomed Opt Express. 2017;8(5):2732-44.
200. Roy AG, Conjeti S, Karri SPK, Sheet D, Katouzian A, Wachinger C, et al. ReLayNet: retinal layer and fluid segmentation of macular optical coherence tomography using fully convolutional networks. Biomed Opt Express. 2017;8(8):3627-42.
201. Apostolopoulos S, Zanet SD, Ciller C, Wolf S, Sznitman R. Pathological OCT Retinal Layer Segmentation Using Branch Residual U-Shape Networks. ArXiv. 2017;abs/1707.04931.
202. Pekala M, Joshi N, Liu TYA, Bressler NM, DeBuc DC, Burlina P. Deep learning based retinal OCT segmentation. Comput Biol Med. 2019;114:103445.
203. He Y, Carass A, Jedynak BM, Solomon SD, Saidha S, Calabresi PA, et al. Topology guaranteed segmentation of the human retina from OCT using convolutional neural networks. arXiv preprint arXiv:180305120. 2018.
204. Sharrock MF, Mould WA, Hildreth M, Ryu EP, Walborn N, Awad IA, et al. Bayesian deep learning outperforms clinical trial estimators of intracerebral and intraventricular hemorrhage volume. J Neuroimaging. 2022;32(5):968-76.
205. Shah A, Zhou L, Abrámoff MD, Wu X. Multiple surface segmentation using convolution neural nets: application to retinal layer segmentation in OCT images. Biomed Opt Express. 2018;9(9):4509-26.
206. Guo Y, Camino A, Zhang M, Wang J, Huang D, Hwang T, et al. Automated segmentation of retinal layer boundaries and capillary plexuses in wide-field optical coherence tomographic angiography. Biomed Opt Express. 2018;9(9):4429-42.
207. Hamwood J, Alonso-Caneiro D, Read SA, Vincent SJ, Collins MJ. Effect of patch size and network architecture on a convolutional neural network approach for automatic segmentation of OCT retinal layers. Biomed Opt Express. 2018;9(7):3049-66.
208. Chen LC, Zhu Y, Papandreou G, Schroff F. European Conference on Computer Vision (ECCV). 2018.
209. Li Q, Li S, He Z, Guan H, Chen R, Xu Y, et al. DeepRetina: Layer Segmentation of Retina in OCT Images Using Deep Learning. Transl Vis Sci Technol. 2020;9(2):61.
210. Schönbach EM, Strauss RW, Ibrahim MA, Janes JL, Birch DG, Cideciyan AV, et al. Faster Sensitivity Loss around Dense Scotomas than for Overall Macular Sensitivity in Stargardt Disease: ProgStar Report No. 14. Am J Ophthalmol. 2020;216:219-25.
211. Schönbach EM, Strauss RW, Muñoz B, Wolfson Y, Ibrahim MA, Birch DG, et al. Longitudinal Microperimetric Changes of Macular Sensitivity in Stargardt Disease After 12 Months: ProgStar Report No. 13. JAMA Ophthalmol. 2020;138(7):772-9.

212. Schönbach EM, Wolfson Y, Strauss RW, Ibrahim MA, Kong X, Muñoz B, et al. Macular Sensitivity Measured With Microperimetry in Stargardt Disease in the Progression of Atrophy Secondary to Stargardt Disease (ProgStar) Study: Report No. 7. JAMA Ophthalmol. 2017;135(7):696-703.
213. Schönbach EM, Ibrahim MA, Kong X, Strauss RW, Muñoz B, Birch DG, et al. Metrics and Acquisition Modes for Fixation Stability as a Visual Function Biomarker. Invest Ophthalmol Vis Sci. 2017;58(6):Bio268-bio76.
214. Schonbach E, editor Month 24 results from the scotopic microperimetric assessment of rod function in Stargardt diseasedisease (SMART) study. American Academy of Ophthalmology Annual Meeting; 2019.
215. Salvatore S, Fishman GA, McAnany JJ, Genead MA. Association of dark-adapted visual function with retinal structural changes in patients with Stargardt disease. Retina. 2014;34(5):989-95.
216. Nuzbrokh Y, Ragi SD, Tsang SH. Gene therapy for inherited retinal diseases. Ann Transl Med. 2021;9(15):1278.
217. Curtis HJ, Seow Y, Wood MJA, Varela MA. Knockdown and replacement therapy mediated by artificial mirtrons in spinocerebellar ataxia 7. Nucleic Acids Res. 2017;45(13):7870-85.
218. Cehajic-Kapetanovic J, Eleftheriou C, Allen AE, Milosavljevic N, Pienaar A, Bedford R, et al. Restoration of Vision with Ectopic Expression of Human Rod Opsin. Curr Biol. 2015;25(16):2111-22.
219. Radu RA, Han Y, Bui TV, Nusinowitz S, Bok D, Lichter J, et al. Reductions in serum vitamin A arrest accumulation of toxic retinal fluorophores: a potential therapy for treatment of lipofuscin-based retinal diseases. Invest Ophthalmol Vis Sci. 2005;46(12):4393-401.
220. Amengual J, Golczak M, Palczewski K, von Lintig J. Lecithin:retinol acyltransferase is critical for cellular uptake of vitamin A from serum retinol-binding protein. J Biol Chem. 2012;287(29):24216-27.
221. Golczak M, Maeda A, Bereta G, Maeda T, Kiser PD, Hunzelmann S, et al. Metabolic basis of visual cycle inhibition by retinoid and nonretinoid compounds in the vertebrate retina. J Biol Chem. 2008;283(15):9543-54.
222. Kaiser-Kupfer MI, Peck GL, Caruso RC, Jaffe MJ, DiGiovanna JJ, Gross EG. Abnormal Retinal Function Associated With Fenretinide, a Synthetic Retinoid. Archives of Ophthalmology. 1986;104(1):69-70.
223. Decensi A, Fontana V, Fioretto M, Rondanina G, Torrisi R, Orengo MA, et al. Long-term effects of fenretinide on retinal function. Eur J Cancer. 1997;33(1):80-4.
224. Mata N, Lichter J, Vogel R, Han Y, Bui T, Singerman L. Investigation of oral fenretinide for treatment of geographic atrophy in age-related macular degeneration. Retina (Philadelphia, Pa). 2012;33.
225. Mata NL, Lichter JB, Vogel R, Han Y, Bui TV, Singerman LJ. Investigation of oral fenretinide for treatment of geographic atrophy in age-related macular degeneration. Retina. 2013;33(3):498-507.
226. Petrukhin K. Pharmacological inhibition of lipofuscin accumulation in the retina as a therapeutic strategy for dry AMD treatment. Drug Discov Today Ther Strateg. 2013;10(1):e11-e20.
227. Palczewski K. Retinoids for treatment of retinal diseases. Trends Pharmacol Sci. 2010;31(6):284-95.
228. Marmor MF, Jain A, Moshfeghi D. Total rod ERG suppression with high dose compassionate Fenretinide usage. Doc Ophthalmol. 2008;117(3):257-61.